THE EFFECT OF HALLOYSITE NANOTUBES ON THE PROCESSING, THERMAL, MECHANICAL, AND ELECTRICAL PROPERTIES OF POLYMERIC COMPOSITE MATERIALS

by

BAIDAA SHARANI

Submitted to the Graduate School of Engineering and Natural Sciences

in partial fulfillment of the requirements for the degree of

Doctor of Philosophy

Sabanci University

Spring 2023

THE EFFECT OF HALLOYSITE NANOTUBES ON THE PROCESSING, THERMAL, MECHANICAL, AND ELECTRICAL PROPERTIES OF POLYMERIC COMPOSITE MATERIALS

APPROVED BY:

Prof. Dr. Mehmet Yildiz .....
(Thesis Supervisor)

Assoc. Prof. Dr. Fevzi Cakmak Cebeci .....

Asst. Prof. Dr. Bertan Beylergil .....

Asst. Prof. Dr. Hatice Sinem Sas Caycı .....

Prof. Dr. Afzal Suleman .....

DATE OF APPROVAL: 12/07/2023

The Effect of Halloysite Nanotubes on the Processing, Thermal, Mechanical, and Electrical Properties of Polymeric Composite Materials

Baidaa SHARANI

Material Science and Nano Engineering, Ph.D. Dissertation, 2023

Thesis Supervisor: Prof. Dr. Mehmet Yildiz

Keywords: Curing Kinetics, Halloysite Nanotubes, Resin Transfer Molding, Structural Health Monitoring

ABSTRACT

This thesis focuses on achieving a broad understanding of one polymeric system, which is epoxy reinforced with Halloysite nanotubes (HNTs) (epoxy/HNT). The curing kinetics of this system is analyzed, and some of its properties are scanned, whether they are mechanical, thermal, or electrical ones. Comprehensive characterization of epoxy/HNT is conducted to facilitate its practical implementation as a matrix component for Carbon Fiber Reinforced Polymer (CFRP) composites to produce CFRP composites reinforced with HNTs (CFRP/HNT) for aerospace, and automobile applications. The first part of this thesis seeks to detect the most beneficial epoxy/HNT nanocomposites. A series of epoxy/HNT nanocomposites were prepared with various concentrations of HNTs and then tested under flexural stress. To understand the effect of HNTs concentration on the curing process, the curing kinetics of the epoxy and epoxy/HNT nanocomposites were explored by Differential Scanning Calorimetry (DSC) and rheological studies. Model-free (i.e., Friedman method) and model-based kinetic analysis (i.e., Kamel and Sourour (KS) model-based analysis) were used to analyze the DSC experimental data. Each concentration of HNTs produced a combination of both acceleration and inhibition mechanisms during The polymerization process, which led to different local topologies in the polymeric network. The effect of different polymeric networks, in these epoxy/HNT systems with different concentrations of HNTs, on the thermal, mechanical, and thermomechanical performances of nanocomposites was evaluated in detail. Additionally, the feasibility of epoxy/HNT, for usage as materials for structural capacitor applications, was examined by manufacturing epoxy/HNT composites with ionic liquid and lithium perchlorate as additives. The electrical properties of modified epoxy/HNT nanocomposite were tested by Electrochemical Impedance Spectroscopy (EIS), and the analysis of conductivity spectra showed that 5 wt.% and 10 wt.% of HNTs provide ionic conductivity with values close to what was provided by incorporating 1 wt.% on ionic liquid and lithium perchlorate. The results of EIS prove that epoxy/HNT are viable systems for further tuning of ionic conductivity.

The second part of this thesis investigates the effect of HNTs on the properties of CFRP composites, which were prepared by Resin Transfer Molding (RTM) method. The manufactured CFRP and CFRP/HNT plates were subject to flexural and in-plane shear load

tests. It was found that HNTs highly affect the deformation mechanisms of CFRP. This result was further corroborated by health monitoring techniques (i.e., Acoustic Emission (AE), Digital Image Correlation (DIC), and thermal imaging system (IRT)), which were simultaneously employed during the mentioned tests. HNTs improved the flexural- and in-plane shear moduli by ∼18% and ∼ 27%, respectively. Deformation mechanisms were identified, then the experimental data were further supported by non-local meshless numerical analysis, Peridynamics. Furthermore, the RTM mold's design creates a certain flow path for the resin during the wetting process. Therefore, the effect of the flow path on the infiltration of HNTs and the properties of CFRP/HNT composite plates was analyzed by using two different RTM molds. The design of the RTM, and the placement of the inlet and outlet port creates a characteristic front flow path for each type of preform-resin system. The inlet port in the first RTM (RTM(I)) is in the middle of one side of the rectangular mold, and the outlet ports are on the opposite side. The design of RTM(I) creates a linear front flow path. In the second RTM (RTM(II)), the inlet port is in the middle of one side of the mold, and the outlet port is in the center of the plate. This placement in RTM(II) creates a curved front flow path for the resin. In both RTMs, 10 wt.% of HNTs were added to the resin, ∼4.5 wt.% of HNTs were impregnated within the fibers and ∼5.5 wt.% of HNTs were washed away. In RTM(I) the precipitation of HNTs increased gradually from the inlet toward the outlet, however, in RTM(II), the filtration of the nanotubes occurred with variant levels throughout the composite plate and CFRP/HNT plates were inhomogeneous in *Vv* and HNT wt.% , therefore the average flexural and in-plane shear modulus were negatively affected.

Halloysit Nanotüplerin Polimerik Kompozit Malzemelerin İşleme, Termal, Mekanik ve Elektriksel Özellikleri Üzerine Etkisi

Baidaa SHARANI

Malzeme Bilimi ve Nano Mühendisliği, Doktora Tezi, 2023

Tez Danışmanı: Prof. Dr. Mehmet Yildiz

Anahtar kelimeler: Halloysite Nanotüpler, Kürleşme Kinetiği, Reçine Enjeksiyon Kalıplama, Yapısal Sağlık Görüntüleme

ÖZET

Bu tez, Halosit nanotüpler (HNT'ler) ile güçlendirilmiş epoksi bir polimerik sistemin (epoksi/HNT) geniş bir şekilde anlaşılmasına odaklanmıştır. Bu sistemin kürleşme kinetiği ve mekanik, termal ve elektriksel özellikler gibi bazı özellikleri araştırılmıştır. Epoksi/HNT'nin kapsamlı karakterizasyonu, havacılık, uzay ve otomobil uygulamalarında Karbon Elyaf Takviyeli Polimer CFRP kompozitlerinin matris bileşeni olarak pratikte kullanılmasını kolaylaştırmak üzere yürütülmüştür. Bu tezin ilk bölümü, en kullanışlı epoksi/HNT nanokompozitlerini saptamayı amaçlamaktadır. Çeşitli HNT konsantrasyonları ile bir dizi epoksi/HNT nanokompoziti hazırlanmış ve bükülme mukavemetleri test edilmiştir. HNT konsantrasyonunun kürleşme süreci üzerindeki etkisini anlamak için, epoksi ve epoksi/HNT nanokompozitlerinin sertleşme kinetikleri, diferansiyel taramalı kalorimetri (DSC) ve reolojik çalışmalarla araştırılmıştır. DSC deneysel verilerini analiz etmek için modelden bağımsız (Friedman yöntemi) ve modele dayalı kinetik analiz (KS modeline dayalı analiz) kullanılmıştır. HNT'lerin her bir konsantrasyonu, polimerizasyon işlemi sırasında hem hızlanma hem de inhibisyon mekanizmalarının bir kombinasyonunu üretmiş, bu da polimerik ağda farklı lokal topolojilere yol açmıştır. Farklı HNT konsantrasyonlarına sahip bu epoksi/HNT sistemlerindeki farklı polimerik ağların nanokompozitlerin termal, mekanik ve termomekanik performansları üzerindeki etkisi ayrıntılı olarak değerlendirilmiştir. Ek olarak, katkı maddesi olarak iyonik sıvı ve lityum perklorat kullanılarak epoksi/HNT kompozitleri üretilmiş ve epoksi/HNT'nin yapısal kapasitör uygulamaları için malzeme olarak kullanıma yönelik uygulanabilirliği incelenmiştir. Modifiye edilmiş epoksi/HNT nanokompozitin elektriksel özellikleri Elektrokimyasal Empedans Spektroskopisi (EIS) ile test edilmiş ve iletkenlik spektrumlarının analizi, HNT'lerin ağırlıkça %5 ve ağırlıkça %10'unun ilave edilmesinin, ağırlıkça %1 iyonik sıvı ve lityum perklorat ilave edilmesiyle sağlanan değerlere yakın iyonik iletkenlik sağladığını göstermiştir. EIS sonuçları, epoksi/HNT'nin iyonik iletkenliğin iyileştirilmesi için uygun sistemler olduğunu kanıtlamıştır.

Bu tezin ikinci bölümü, HNT'lerin Reçine Enjeksiyon Kalıplama (RTM) yöntemiyle hazırlanan CFRP kompozitlerin özellikleri üzerindeki etkisini araştırmıştır. Üretilen CFRP ve CFRP/HNT plakalar, eğilme ve düzlem içi kayma testlerine tabi tutulmuştur. HNT'lerin

CFRP'nin deformasyon mekanizmalarını oldukça etkilediği saptanmıştır. Bu sonuç, söz konusu testler sırasında eş zamanlı olarak kullanılan sağlık izleme teknikleri (akustik emisyon (AE), dijital görüntü korelasyonu (DIC) ve termal görüntüleme sistemi (IRT)) ile desteklenmiştir. HNT'ler bükülme ve düzlem içi kayma modüllerini sırasıyla ~%18 ve ~%27 oranlarında iyileştirmiştir. Deformasyon mekanizmaları belirlenmiş, ardından deneysel veriler sayısal lokal olmayan ağsız Peridinamik yöntemler ile desteklenmiştir.

Ayrıca, RTM kalıbının tasarımı, ıslatma işlemi sırasında reçine için belirli bir akış yolu oluşturmaktadır. Bu nedenle, akış yolunun HNT'lerin süzülmesi ve CFRP/HNT kompozit plakaların özellikleri üzerindeki etkisi iki farklı RTM kalıbı kullanılarak analiz edilmiştir. RTM'nin tasarımı ve giriş ve çıkış portunun yerleşimi, her tip preform reçine sistemi için karakteristik bir ön akış yolu oluşturmaktadır. RTM(I)'deki giriş ağzı dikdörtgen kalıbın bir tarafının ortasındadır ve çıkış ağızları karşı taraftadır. RTM(I) tasarımı, doğrusal bir ön akış yolu oluşturur. RTM(II)'de giriş ağzı kalıbın bir tarafının ortasındadır ve çıkış ağzı plakanın merkezindedir. RTM(II)'deki bu yerleşim, reçine için kavisli bir ön akış yolu oluşturur. Her iki RTM'de, reçineye ağırlıkça %10 HNT ilave edilmiş, ağırlıkça ~%4.5 HNT'ler lifler içinde emprenye edilmiş ve ağırlıkça ~%5.5 HNT yıkanarak uzaklaştırılmıştır. RTM(I)'de HNT'lerin nüfuzu girişten çıkışa doğru kademeli olarak artmıştır, ancak RTM(II)'de nanotüplerin nüfuzu kompozit plaka ve CFRP/HNT plakaları boyunca hacimce (V_v) ve ağırlıkça (HNT wt.%) değişken seviyelerde, homojen olmayan bir şekilde gerçekleşmiştir. Bu nedenle ortalama eğilme ve düzlem içi kayma modülü olumsuz etkilenmiştir.

ACKNOWLEDGEMENTS

I would like to express my gratitude to my advisor Prof. Dr. Mehmet Yildiz for his continuous support and guidance throughout my studies. I am also so grateful for Dr. Jamal Seyyed Monfared Zanjani for his guidance and discussion in the first year of my Ph.D. I am really grateful to the technical staff in SU-IMC for all their help and efforts. Additionally, I would like to thank my friends and colleagues who made this journey valuable and bearable. Finally, I am endlessly grateful to my family for their love and support.

TABLE OF CONTENTS

LIST OF FIGURES

LIST OF TABLES

LIST OF SYMBOLS AND ABBREVIATIONS

HNTs	Halloysite nanotubes
CNTs	Carbon nanotubes
epoxy/HNT	epoxy reinforced with Halloysite nanotubes
FRP	Fiber reinforced polymer
CF	Carbon fibers
CFRP	Carbon fiber reinforced polymer
CFRP/HNT	CFRP composites reinforced with HNTs
RTM	Resin Transfer Molding
RTM(I)	the first RTM
RTM(II)	the second RTM
N(I)	CFRP plates that are produced via RTM(I)
NT(I)	CFRP/HNT plates that are produced via RTM(I)
N(II)	CFRP plates that are produced via RTM(II)
NT(II)	CFRP/HNT plates that are produced via RTM(II)
KFM	kinetic free method
KS	Kamal and Sourour model
WLF	Williams-Landel-Ferry
OFW	Ozawa-Flynn-Wall
KAS	Kissinger-Akahira-Sunose
PD	Peridynamcs
DGEBA	Diglycidyl ether of bisphenol A
DSC	Differential Scanning Calorimetry
EIS	Electrochemical Impedance Spectroscopy
DMA	Dynamic Mechanical Analysis test
SEM	Scanning Electron Microscopy
AE	Acoustic Emission
DIC	Digital Image Correlation
IRT	Thermal imaging system
FTIR	Fourier Transform Infrared
TGA	Thermal Gravimetric Analyzer
DTA	Differential Thermal Analysis
WE	working electrode
RE	reference electrode
H0	epoxy/HNT(0 wt.%) nanocomposites
H0.5	epoxy/HNT(0.5 wt.%) nanocomposites
H1	epoxy/HNT(1 wt.%) nanocomposites
H2	epoxy/HNT(2 wt.%) nanocomposites
H5	epoxy/HNT(5 wt.%) nanocomposites
H10	epoxy/HNT(10 wt.%) nanocomposites
mHNTs	alkaline modified HNTs
mH0	epoxy/mHNT(0 wt.%) nanocomposites
mH0.5	epoxy/mHNT(0.5 wt.%) nanocomposites
mH1	epoxy/mHNT(1 wt.%) nanocomposites
mH2	epoxy/mHNT(2 wt.%) nanocomposites

mH5	epoxy/mHNT(5 wt.%) nanocomposites
mH10	epoxy/mHNT(10 wt.%) nanocomposites
ΔH_t	heat of reaction after certain time
$\Delta H_{tot.}$	total heat of reaction
T	temperature
T_{onset}	temperature at the beginning of the exothermic peak
T_p	T_{peak} of the exothermic peak in DSC curves
T_{endset}	temperature at the end of the exothermic peak
ΔT	estimated as temperature range at the base of the exothermic peak
$\overline{\Delta H_{tot.}}$	average of the total exothermic heat of reaction
Ea	activation energy
Ea_1	activation energies for the noncatalytic reactions
Log (A_1)	rate constants for the noncatalytic reactions
K_1	the first rate-constant for the noncatalytic reactions
n	exponent describes the n-th order noncatalytic reaction
Ea_2	activation energies for the autocatalytic reactions
Log (A_2)	rate constants for the autocatalytic reactions
K_2	the second rate-constant for the autocatalytic reactions
m	exponent describes the autocatalytic contribution of the reaction
α	conversion
Log($K_{diff.}$)	the diffusion-controlled reaction rate constant
C_1	general constant
C_2	general constant
d_{98}	the point in the size distribution, up to and including 98% of the total volume of material in the sample is contained
d_{90}	the point in the size distribution, up to and including 90% of the total volume of material in the sample is contained
d_{50}	the point in the size distribution, up to and including 50% of the total volume of material in the sample is contained
μ'	dynamic storage modulus
μ''	dynamic loss modulus
G'	storage modulus
G''	loss modulus
$\bar{S}$	average values of flexural strength
$\bar{\varepsilon}$	average values of strain at the maximum load
$\bar{E}$	average values of flexural modulus
T_g	glass transition temperature
$\overline{T_g}$	average T_g
$\|\mu^*\|$	complex viscosity
$\|\mu^*\|_{gel.}$	complex viscosity at the gelation point
$t_{gel.}$	critical gelation point
tan δ	tangent delta
$(\tan\delta)_p$	the peak point of the tan δ graph
$T_{Inflec.}$	T at the inflection point in DTA curve
ω	oscillatory shear strain

Res. wt.	residual weight
wt.%	weight per cent
σ_{dc}	dc-conductivity
Z'	the real part in Nyquist curve
Z''	the imaginary part in Nyquist curve
R0	Ohmic resistance
f	frequency
-OH	hydroxyl groups
$-NH_2$	amine group
N_2	Nitrogen gas
IL	ionic liquid
$LiClO_4$	Lithium perchlorate
SG	strain gauge
WPF	weighted peak frequency
PP2	partial power 2
ROI	regions of interest
cluster-cr	AE hit-cluster associated with matrix crack failure
cluster-d	AE hit-cluster associated with delamination failure
cluster-fr	AE hit-cluster associated with fabric fracture
0º CFs	CFs parallel to the examined plane within the fracture surface
90º CFs	CFs normal to the examined plane within the fracture surface
ε_{xx}	axial strain
ε_{yy}	transverse strain
ρ	density
$\bar{\rho}$	average density
V_v	void volume fraction
$\overline{V_v}$ (%)	average void volume fraction
δ	a finite distance referred to as horizon
dx	the particle spacing
U*i*	displacement of the material points *i*, caused by a deformation of the continuum
U*j*	displacements of the material points *j*, caused by a deformation of the continuum
$\mathbf{Y}_i$	the deformed positions of material point *i*
$\mathbf{Y}_j$	the deformed positions of material point *j*
$\mathbf{X}_i$	initial position of material point *I*
ρ_i	the density of the continuum at point *i*
$\ddot{\mathbf{U}}_i$	vector of the acceleration acting on material point *i*
B*i*	vector of body force density acting on material point *i*
$\mathbf{t}_{ij}$ and $\mathbf{t}_{ji}$	the pairwise force densities between material points *i* and *j*
C*i* and C*j*	auxiliary parameter established through interrelating force density vectors and the strain energy in the continuum
θ_i	PD dilatation of point *i*
θ_j	PD dilatation of point *j*
V_i	the volume of particle *i*
V_j	the volume of particle *j*

λ_{ij}	irreversible control parameter for the breakage of the related PD bond
G_c	the critical energy release rate
φ_i	extra damage parameter
ppm	parts per million
N	newton
kN	kilonewton
J/g	joules per gram
µs	micro second
min.	minute
mm^3	cubic millimeter
µm	micro meter
γ_A	gamma amplitude
mm	millimeter
℃	degree Celsius
µL	microliter
Hz	hertz
mHz	millihertz
MHz	megahertz
MPa	megapascal
GPa	gigapascal
Pa.s	Pascal second
gsm	grams per square meter
dB	decibel
S/cm	Siemens per centimeter

CHAPTER 1. STATE-OF-THE-ART

Halloysite nanotubes (HNTs) are multilayers silicate aluminate, clay-based nanomaterials, which have captivated the academic research as a promising component for applications such as drug delivery and membrane engineering. Nevertheless, research exploring HNTs in structural composites is relatively limited. This thesis seeks to contribute to this gap by focusing on scanning various properties of carbon fiber reinforced polymer (CFRP) system with additional emphasis on the effect of HNTs on system developments, characteristics, and performance under stress loads, whether tested under out-of-plane (perpendicular) loads (as in three-point bending test) or under in-plane shear loads (as in in-plane shear test using the Iosipescu shear test fixture).

In the first part of the thesis, curing kinetics of epoxy/HNT polymeric nanocomposites are studied. Based on analyzing the curing kinetics of epoxy/HNT system with various HNTs concentrations, a curing kinetic model is constructed. This model provides a source from which multiple quantitative relationships are derived. Those structural relationships change the morphology of the polymeric network locally, and this results in a non-linear relationship between the increase of HNTs amount and the response to stress. In addition, the effect of the HNTs concentration on the polymeric chain length, and thus on the conductivity of such systems, is examined by Electrical Impedance Scanning Spectroscopy (EIS).

The second part of this thesis examines the direct effect of HNTs on the interfacial interaction between the matrix and plain woven carbon fibers. The study is composed of destructive analysis techniques such as three-point bending and in-plane shear tests, accompanied with non-destructive techniques such as Acoustic Emission (AE), Digital Image Correlation (DIC), and thermal imaging (IRT). Moreover, the experimental results are supported with computational Peridynamic Analysis. CFRP composite plates were manufactured using Resin Transfer Molding (RTM) technique. It was found that HNTs improved the overall performance of CFRP composites with this simple manufacturing technique, without additional modifications to the HNTs prior to the composite manufacturing process. Pristine HNTs were used after drying overnight at 100 ^{o}C and

resulted in higher resistance to flexural and in-plane shear stresses. During the manufacturing process it became more demanding to explore how the location of the injection outlets in the mold affects the propagation of the flow front. The presence of HNTs with high concentrations in the injected resin perpetuates phenomena such as agglomeration, filtration, and pores formation within the composite system. To answer these inquires, two RTM molds were used to manufacture CFRP composites with and without HNTs. The first RTM mold had linear injection flow, while injection ports in the second RTM mold were located to produce a curved flow path. The produced plates were analyzed under flexural and in-plane shear test. It is found that there was little range of void volume fraction where the composites performance improved under three-point bending and in-plane shear tests. The formation and distribution of these voids is directly related to the injection flow layout within the mold, and the location of the injection ports. The linear flow in the first RTM mold produced CFRP with better resistance to flexural and in-plane shear tests compared to CFRP produced by the second RTM. Similar results were obtained for CFRP/HNTs composites.

Material from this dissertation has been published in the following journals and two additional papers are under preparation or submission processes:

B. AlKhateab, I.E. Tabrizi, J.S.M. Zanjani, M.N. Rahimi, L.H. Poudeh, A. Kefal, M. Yildiz. *Damage mechanisms in CFRP/HNT laminates under flexural and in-plane shear loadings using experimental and numerical methods.* **Composites Part A: Applied Science and Manufacturing**, 2020. 136. 105962.

B. AlKhateab, L.H. Poudeh, S. Elmas, H.S. Sas, M. Yildiz, *Aspects of Halloysite Nanotubes Integration in Epoxy Nanocomposites; Curing kinetics and Deformation Mechanism.* **Polymer Composites**, 2023. 44 (1), 574-591.

CHAPTER 2. ASPECTS OF HALLOYSITE NANOTUBES INTEGRATION IN EPOXY NANOCOMPOSITES; CURING KINETICS AND DEFORMATION MECHANISM

The curing kinetics of Diglycidyl ether of bisphenol A (DGEBA) epoxy resin using amine-based hardener in the presence of HNTs are investigated by performing isothermal and dynamic Dynamic Scanning Calorimetry (DSC) measurements, followed by a detailed analysis of the experimental data via the kinetic free method (KFM) and three common model-based analysis. Kamal and Sourour (KS) model gave the best fit for the experimental data and thus, was further modified by Williams-Landel-Ferry (WLF) diffusion control equations to calculate the diffusion constants near the glass transition temperature (T_g). The optimized model is used to find the curing kinetics parameters of epoxy/HNT nanocomposites, and these finding are further validated and explained by performing rheometric measurements. Noncatalytic and autocatalytic curing reactions and diffusion constants are all functions of the amount of HNTs. HNTs shift the curing reaction slightly toward higher temperatures and promote etherification reactions, leading to an increase in the curing enthalpy, as extra bonds will be formed between HNTs and epoxy resin during the polymerization. The combination of acceleration and inhibition mechanisms dictates the complex kinetics of the reactions at high concentrations of HNTs, while the produced local topology of the polymeric network depends highly on HNTs weight ratio. Furthermore, to investigate the mechanical performance of the prepared nanocomposites under flexural loads, three-point bending tests were performed in both modes, dynamic and static, followed by a fractography analysis of the fractured surfaces. The mechanical properties have improved due to the addition of pristine HNTs without compromising the T_g of the polymer. This study provides a set of observational relationships between various chemical interactions during polymerization and the final topology and performance of the polymer, which in turn aims to bridge the gap in the literature between the curing kinetics of epoxy/HNT nanocomposites and the performance of these nanocomposites under various thermal and mechanical stresses.

2.1. Introduction

Polymeric composites with superior mechanical and physical properties are of great interest in many applications such as aerospace, automotive, and energy industries [1]. Epoxy and its derivatives are widely used in structural composites due to their favorable chemical and thermal resistances. However, relatively low toughness and, in turn, the brittle nature of the epoxy resin lead to poor resistance to crack initiation and failure growth in manufactured parts. Several attempts have been made to address this problem and improve the matrix-dominant properties by incorporating organic [2-4] and inorganic nanomaterials [5-8] in polymeric matrices. Layered silicate materials, known as nano-clays, are considered one of the most attractive inorganic fillers due to their low cost and environmentally friendly nature. However, the performance of epoxy composites depends on the curing quality, and the presence of nanomaterials within the uncured epoxy system adds more complexities to the kinetics of the curing reactions. Hence, exploring the curing reaction kinetics of the resin and understanding the rheological characteristics of the system [9-12] are highly important steps to unraveling the key factors of the process and establishing optimized curing cycles for the epoxy composites. The epoxy polymerization reaction can be described by mainly two phases, chemically controlled and diffusion controlled [13]. Initially, the reaction is fast (i.e., chemically controlled). In this stage, an autocatalytic model by an n^{th} order expression is sufficient to describe the reaction [14, 15]. After a certain degree of cross linking, the viscosity increases, and the curing rate slows significantly. Thus, the curing reaction becomes dominated by diffusion mechanisms (i.e., diffusion controlled), and the curing kinetic model should be modified using diffusion control function [16].

The performance of the nanomaterials used in producing epoxy nanocomposite is closely linked to their size, shape, and surface functionalities. Kamran-Pirzaman et al. [17] reported that integrating unmodified nano silica increases the activation energy (*Ea*), whereby modified silica nanoparticles can reduce *Ea* compared to the epoxy and epoxy/unmodified nano silicate counterparts. Similarly, Tcherbi-Narteh et al. [18] studied the effect of montmorillonite nano clay on DGEBA epoxy composites and found that the presence of 1 wt.% montmorillonite resulted in the formation of longer molecular chains and lower resistance to segmental mobility compared to 2 and 3 wt.% montmorillonite systems.

Consequently, relatively higher energy was required at higher concentrations to fuse montmorillonite /epoxy molecules during vitrification and increase the crosslinking density.

Tubular double-layered clays known as HNTs have also been used as an effective clay type to improve the mechanical properties of polymeric composites [19, 20]. The crystal structure of HNTs that is similar to carbon nanotubes (CNTs) with regard to the aspect ratio, provides an extensive usage area for epoxy/HNT composites [21, 22]. Furthermore, HNTs are cheap, abundant, and have a high resistance to mechanical and thermal stresses [23]. Although the morphology of HNTs is similar to that of CNTs [24], they do not suffer from entanglement problems as CNTs do, making HNTs more easy-to-handle materials that can be integrated into the composite with high weight ratios when needed. In the case of epoxy nanocomposites, the integration of HNTs into the matrix significantly reduces the shrinkage after polymer curing, strengthens the polymeric matrix, and improves the fiber-matrix interface, all of which enhance the matrix's ability to respond to stress in out-of-plane (i.e., flexural) direction [25]. In one of the recent works, Akbari et al. [26] have compared the effect of neat, alkaline treated, and silane functionalized HNTs on the curing process and stated that these nanotubes showed a catalytic influence on the curing reaction due to the presence of hydroxyl groups (-OH) on the surface of HNTs. Jouyandeh et al. [27] analyzed the effect HNTs concentration on the curing behavior of the epoxy/anhydride hardener system and indicated that the addition of 0.5 and 1 wt.% of HNTs has prompted the crosslinking while 2 wt.% HNTs hindered the reaction due to the deactivation of the curing agent fueled by diffusion into the lumen of HNTs. Although several studies have focused on adding nanofillers to epoxy composites, to the best of our knowledge, no work investigates the effect of HNTs concentration on curing kinetics and deformation mechanism of epoxy/amine-based hardener systems. Despite the promising results regarding the integration of pristine HNT as a cheap yet effective toughener, there is still a shortage of preliminary investigations concerning network formation in epoxy/HNT nanocomposites.

To tune epoxy/HNT nanocomposite properties for better mechanical performance, one should control mainly three factors: (i) HNTs dispersion, (ii) HNTs concentration, and (iii) the interfacial interaction in the composite system. Firstly, concerning the dispersion, the multilayer structure and the absence of entanglement of HNTs facilitate their dispersion in viscous polymers [28]. However, the processing of nanocomposites should be optimized

since HNTs tend to agglomerate due to Van der Waals forces. Ye et al. [24] investigated the morphology of epoxy/HNT nanocomposites through advanced electron microscopy techniques and reported the presence of two different regions, namely, an epoxy-rich region (i.e., continuous phase) and HNT-rich regions (i.e., a discontinuous phase). Secondly, by examining the existing literature regarding the effect of HNTs concentration on epoxy nanocomposites properties [29-36], the maximum weight percentage of used HNTs is in the range of 2-3%, where there is a threshold after which the mechanical properties start to degrade. However, there is a lack of data encompassing a wider range of concentrations after reaching the threshold. In this study, a wide range of HNTs concentration is studied (i.e., epoxy/HNT(0, 0.5, 1, 2, 5, and 10 wt.%) nanocomposites). Finally, concerning the polymer/HNT interfacial interactions, studies showed that integrating HNTs at low weight ratios provides crack front pinning [34], and bridging effects [24] on the matrix deformation. Currently, there are no available explanations of how the HNTs affect the mechanical properties of the polymeric nanocomposites on the molecular level. Eventually, it is necessary to explore how HNTs promote other toughening mechanisms at higher HNT concentrations, i.e., plastic void growth and the formation of matrix shear bands [35, 37]. Additionally, the addition of nanomaterial to the resin might compromise the mechanical properties if it causes a decrease in the glass transition temperature (T_g) of nanocomposites. Such a decrease is due to the presence of the nanomaterial within the polymer cross-linking net, which will hinder the movement of the polymeric chains under dynamic load. Generally, the effect of silica-based nanoparticles on the T_g is a debated issue since some systems showed a decrease in the T_g. In contrast, other polymeric systems' T_g has improved after incorporating silica-based nanoparticles. Such inconsistency in the reported results is attributed to the competition between morphology, size, and concentration of the used nanomaterial.

This research aims to bridge the gap in the existing literature between the curing kinetics and the morphology of the nanocomposites at various concentrations of pristine tubular nanomaterials that have the capacity to contribute to the curing of epoxy resin alongside an amine-based curing agent. Moreover, it explores how the change in weight fraction of HNTs affects the local topology of the polymeric network and, consequently, alters the mechanical performance of epoxy/HNT nanocomposites under static and dynamic

loads. In the present study, curing kinetics of epoxy/HNT(0, 0.5, 1, 2, 5, and 10 wt.%) nanocomposites are explored by performing dynamic and isothermal DSC measurements and fitting the experimental data using KFM and model-based analysis. The complex viscosity profiles are obtained from rheological measurements and used to explain the kinetics properties that the model produced. The static and dynamic three-point bending tests are performed, and the surface of the fractured specimens under statistical flexural load is examined by Scanning Electron Microscopy (SEM).

2.2. Experimental

2.2.1. Materials

HNTs with the size of d_{98} = 9.95 µm, d_{90} = 5.01 µm, and d_{50} = 0.53 µm (where d_{98}, d_{90}, and d_{50} signify the point in the size distribution, up to and including 98%, 90%, or 50% of the total volume of material in the sample is contained, respectively), and a specific surface area of 128 m^2/g were supplied by ESAN, Turkey. Two components, DGEBA epoxy (ARALDITE® LY 1564 SP resin and XB 3403 hardener), were purchased from HUNTSMAN.

2.2.2. Preparation of epoxy/HNT Nanocomposites

Due to its high hygroscopic nature, HNT was dried at 100 ℃ for 24 hours and then immediately transferred to a sealed tube before its use for nanocomposite manufacturing and characterization steps. Epoxy resin was mixed with the hardener in a 100:36 mass ratio to prepare the neat epoxy system. To investigate the effect of HNTs weight content on the properties of nanocomposites, a set of epoxy/HNT samples with various HNT concentrations (0, 0.5, 1, 2, 5, and 10 wt.% to the total composite weight) was manufactured. The following samples (epoxy, epoxy/HNT(1 wt.%), epoxy/HNT(2 wt.%), epoxy/HNT(5 wt.%), and epoxy/HNT(10 wt.%) will be referred to as (H0, H1, H2, H5, and H10) interchangeably throughout the text. To produce epoxy/HNT nanocomposites, a given amount of pristine HNTs was mixed with epoxy resin through subsequent ultrasonication for 30 minutes to enhance the interfacial interactions between the constituents. The amine-based curing agent was added to the epoxy/HNT mixture, followed by manual stirring for 5 minutes at room temperature. Knowing that ultrasonication with a probe sonicator causes a significant increase in the temperature of the mixture, each mixture was kept in an ice bath for 2 minutes

after every five minutes of sonication to prevent its premature curing. At the final step, samples were degassed for 15 minutes and then casted onto Teflon molds with dimensions of 4 mm x 14 mm x 100 mm to produce three-point bending test and Dynamic Mechanical Analysis (DMA) test specimens. The curing process was conducted in an oven at 80 ℃ for 48 hours. The cured specimens were carefully demolded and then post-cured for 12 hours at 80 ℃ (Figure 2.1).

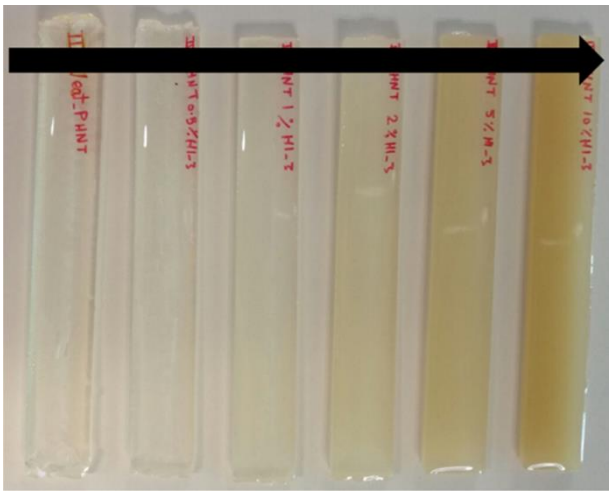

Figure 2.1 Image of produced epoxy and epoxy/HNT nanocomposites where specimens are ordered with increasing content of HNTs from left to right starting from epoxy towards epoxy/HNT(0.5, 1, 2, 5, and 10 wt.%).

2.2.3. Characterization

The curing reaction of uncured epoxy and epoxy/HNT mixtures was studied using the dynamic DSC method under an N_2 atmosphere with heating rates of 2.5, 5, 7.5, and 10 ℃/min. in a temperature range of 25 ℃ to 300 ℃ to cover the entire curing process. Next, the sample was cooled down to room temperature, and reheated to 150 ℃ to obtain T_g of the polymer/nanocomposite. Isothermal DSC measurements were conducted at 80 ℃, 100 ℃, and 120 ℃ for 5 hours for the neat epoxy and the epoxy/HNT (10 wt.%) nanocomposites. The Kinetic Neo Netzsch software is used for data analysis by conducting KFM analysis with different heating rates in which the reaction rate equation, conversion rate, and activation energies are obtained for each sample accordingly. To find the complex viscosity ($|\mu^*|$) profile of nanocomposites, dynamic rheometric measurements of oscillatory shear strain are performed by MCR 302 rheometer under static air at 0.01 % γ_A, 1Hz frequency, and 0 N normal force by ASTM D1525 standard. The first interval of the test is to raise the

temperature of a specimen from 20 ℃ to 80 ℃ at 2.5 ℃/min heating rate, followed by a stage where temperature is held constant at 80 ℃ for an additional 20 minutes. $|\mu^*|$ is calculated from equation 2.1,

$$|\mu^*| = \sqrt{\mu'^2 + \mu''^2} \quad (2.1)$$

Where ω is the oscillatory shear strain, $\mu' = G'/\omega$ (i.e., G' is dynamic storage modulus), and $\mu'' = G''/\omega$ (i.e., G'' is dynamic loss modulus.

The basic composition of cured nanocomposites and pristine HNTs is analyzed using Fourier Transform Infrared (FTIR) spectroscopy (Thermo Fisher Scientific Nicolet iS10). Additionally, resin, hardener, and resin + hardener cured for 0, 1, 2, and 18 hours are examined to check the progress of the cure during the polymerization of epoxy resin. The thermal stability of HNTs and cured epoxy/HNT nanocomposites is studied by a thermal gravimetric analyzer (TGA) (Mettler Toledo (TGA) / DSC 3+ Star system) employing 70 µL alumina sample holders. For each concentration of epoxy/HNT nanocomposites, three specimens are tested. The samples are heated up to 1000 ℃ at a rate of 20 ℃/min. under N_2 gas. The elastic and viscoelastic properties of the specimens are studied by the DMA using Melter Toledo (DMA)/SDTA861 instrument. To assess the effect of HNTs on T_g, at least, two specimens are tested under three-point bending mode at 1 Hz frequency within a temperature range of 30 ℃ to 150 ℃ and with a heating rate of 3 ℃/min. Specimens are mechanically tested under bending load using Instron Universal Testing Machine (5982) equipped with a static load cell of ±100 kN by ASTM D790-03 standard, where each batch is composed of five specimens. The morphology of dried HNTs and surface morphology of fractured flexural epoxy/HNT nanocomposite specimens are analyzed by Leo Supra35VP Field Emission SEM.

2.3. Results and Discussion

2.3.1. Characteristic properties of HNTs

The physical and morphological properties of HNTs play an important role in their interfacial interactions with polymeric chains. In this regard, the thermal stability (i.e., the resistance to degradation under elevated temperatures) of HNTs is analyzed by TGA, and the results are given in Figure 2.2. The total residual weight of hydrated (undried) and dried

HNTs is measured as 84 wt.% and 79 wt.%, respectively, indicating the samples' good thermal stability. The dried HNTs lose 3 wt.% of their weight below 100 ℃ due to the loss of remaining absorbed water. As the temperature is increased up to 400 ℃, there is a gradual decrease of about 2 wt. % in the residual weight (Res. wt.). On the other hand, at around 400 ℃, a relatively sharp drop is observed in the weight of the sample from 95 wt.% down to 85 wt.%, which is attributed to the dihydroxylation of the residual structural aluminium hydroxide groups [36, 38], and water molecules [39]. Undried HNTs show similar degradation behavior compared to dried ones, except that there is a 7 wt.% loss between 100 ℃ and 400 ℃. This difference can be explained by the desorption of water molecules that are physically adsorbed in the inner and outer surface of the HNTs [40].

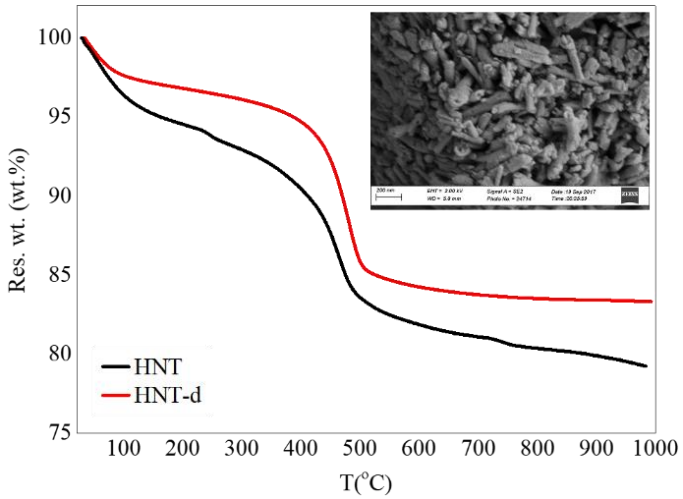

Figure 2.2 TGA curves of dried (HNT-d) and undried HNTs (HNT) tested under N_2 gas, inset: SEM micrograph of pristine dried HNTs.

The inset SEM micrograph in Figure 2.2 shows HNTs having tubular morphology with a diameter ranging from 200 to 550 ± 20 nm and with an average length of 626 nm. The main structure of HNTs consists of a double layer of aluminates and silicates. The difference in the size of the tetrahedral silicate molecule and the octahedral aluminate molecule causes a distortion in the crystal structure; hence, the planer double layer of HNT bends to relieve the stress, thereby forming a tubular morphology [41]. HNTs may be formed in different morphologies depending on the number of water molecules located within the silicate and aluminate layers. Nevertheless, the linear morphological features of HNTs (which are dominant) prevent entanglement and facilitate their dispersion in various polymeric mediums.

2.3.2. Curing kinetics

The development of a reaction kinetic model for epoxy/HNT nanocomposites is important to establish a reliable curing cycle that is needed in composite manufacturing by RTM or injection molding processes. In the current study, epoxy/HNT nanocomposites are used as a matrix material in CFRP composites manufactured via RTM method. The optimization of the curing kinetic model is performed on epoxy/HNT(10 wt.%) since this is the highest and most challenging concentration that can be handled in the RTM process (i.e., the injection process will get more difficult due to the increase in the viscosity of epoxy/HNT mixture). First, the isothermal DSC measurements are done at three different temperatures in order to get the T_g as a function of the applied temperature, afterward; the DiBenedetto function, which uses the T_g as a function of the degree of cure or conversion (α), is used to optimize the curing constants in the model. α is calculated using equation 2.2,

$$\alpha = \frac{\Delta H_t}{\Delta H_{tot.}} \tag{2.2}$$

Where ΔH_t is the heat of reaction after certain time, and $\Delta H_{tot.}$ is the total heat of reaction. Finally, the optimized model is used to find the mentioned constants as a function of specific concentrations of HNTs [42].

2.3.2.1. DSC measurements

Figure 2.3a and 2.3b show the variation of heat flow with temperature and time, respectively. In general, all DSC curves possess a typical form with one exothermic peak, meaning there are no side reactions during the curing. The curing reaction of epoxy with amine-based curing agent proceeded with addition-polymerization without side reaction [26, 27].

The curing process proceeds in three steps that can be observed from the DSC graphs below in Figure 2.3, namely, (i) the deviation in the linearity of the heat flow, (ii) the formation of an exothermic peak corresponding to the curing and crosslinking of the epoxy, and finally (iii) a quasi-linear heat flow region. As the heating rate increases, the exothermic heat flow rises and T_{peak} (T_p) shifts towards higher temperatures while the duration of the curing process (i.e., estimated as temperature range at the base of the exothermic peak (ΔT)) decreases.

The progress of the curing process and the formation of thermosetting system network can be monitored by epoxy ring-opening reaction with a slow to intermediate reactive curing agent. $\Delta H_{tot.}$ increases with higher heating rates (Table 2.1) because the higher the heating rate is, the more local reaction sites are available; hence, the system can reach its gelation point much quicker. Generally, HNTs play a catalytic role in the polymerization where it increases the reaction probability and reaction heat, (i.e., the average of the total heat of the reaction ($\overline{\Delta H_{tot.}}$) increases by 39% upon the addition of 10 wt.% HNTs) because the presence of HNTs among the unreacted monomers lowers the free volume and provides additional reaction sites (i.e., heterogeneous nucleation points to initiate polymerization) in the reaction medium.

Table 2.1 lists temperatures at the start (T_{onset}) and at the end (T_{endset}) of the exothermic peak, ΔT, T_p, T_g, and average T_g ($\overline{T_g}$) (average value is calculated based on T_g for four different heating rates) of both epoxy and epoxy/HNT(10 wt.%) nanocomposite at four different heating rates.

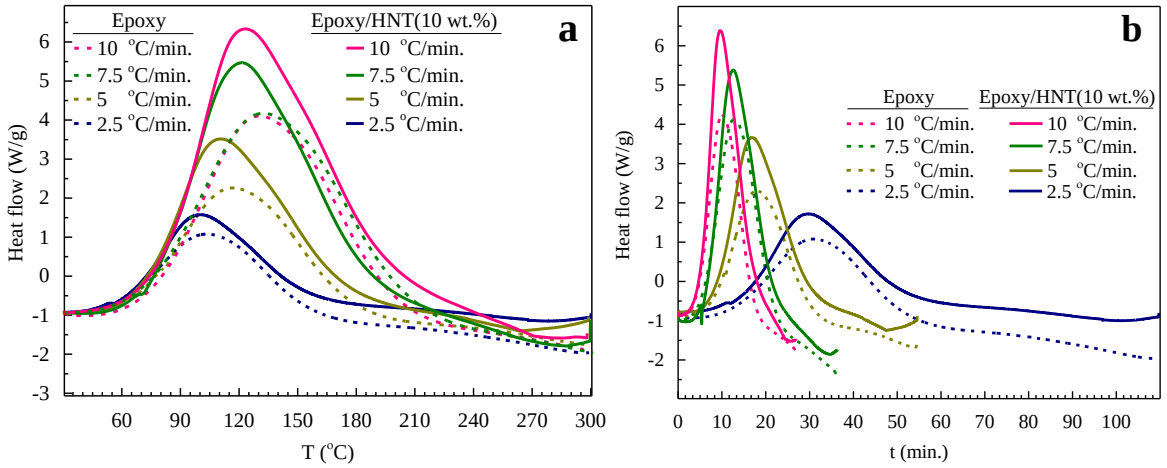

Figure 2.3 Dynamic DSC graphs during the curing cycles of epoxy and epoxy/HNT(10 wt.%) nanocomposite at 2.5, 5,7.5, and 10 °C/min. as a function of (a) temperature, and (b) time.

In the epoxy polymerization reaction, a three-dimensional cross-linking network is formed. At the early stages of curing reaction, the polymerization is chemically controlled. HNTs restrict bond formation at lower temperatures thereby increasing T_{onset} of epoxy/HNT(10 wt.%) with respect to pristine epoxy, which can be observed from Table 2.1. As the network is growing, the viscosity increases gradually until a *"critical conversion"* state is reached. After this point, the reaction becomes diffusion controlled and the speed of

the reaction decreases significantly even though there are still unreacted epoxides and amine groups in the system. In the case of epoxy/HNT system, HNTs promote the critical conversion at lower temperature because T_p, where the reaction rate is maximum, slightly decreases when compared to its counterparts for the neat epoxy at each heating rate.

HNTs prolong the diffusion-controlled reaction and ΔT of cure (T_{endset} - T_{onset}) of the exothermic peak increases in comparison to the neat resin's. Moreover, higher heating rates result in lower T_g values due to fast curing process, yet $\overline{T_g}$ of epoxy/HNT negligibly changes compared to $\overline{T_g}$ of epoxy. Therefore, it is readily apparent that HNTs played a catalytic role in the curing process without compromising the properties of epoxy resin.

Table 2.1 ΔH_{tot}, $\overline{\Delta H_{tot.}}$, T_{onset}, T_{endset}, ΔT, T_p, T_g and $\overline{T_g}$ of epoxy vs. epoxy/HNT(10 wt.%) during dynamic DSC measurements as a function to four different heating rates (2.5, 5, 7.5, and 10 °C/min.).

	Epoxy				**Epoxy/HNT(10 wt. %)**			
Heating rate (°C/min.)	2.5	5	7.5	10	2.5	5	7.5	10
$\Delta H_{tot.}$ (J/g)	270	295	307	314	436	410	422	378.5
$\overline{\Delta H_{tot.}}$ (J/g)	296.5				411.6			
T_{onset} (°C)	42	38	39	44	62	70	65	78
T_{endset} (°C)	180	185	200	210	275	270	280	282
ΔT (°C)	138	147	161	166	213	200	215	204
Tp (°C)	103	117	131	130	100	111	121	124
T_g (°C)	66.4	64.9	63.4	62.5	69	68	66	66
$\overline{T_g}$ (°C)	64.3				66.3			

Through using $\Delta H_{tot.}$ data from dynamic DSC, the experimental α curves of epoxy and epoxy/HNT(10 wt.%) at four different heating rates (2.5, 5, 7.5, and 10 °C/min.) are plotted and shown in Figure 2.4. For detailed fitted curves please refer to Figures S2.2-S2.4 in supporting information in Appendix I. The conversion curves of H0 and H10 show a sigmoidal shape indicating an autocatalytic nature of the curing process. It is clearly seen that the conversion of the neat resin and the nanocomposites shift toward higher temperatures when the heating rate increases. Additionally, polymerization of epoxy seems to almost stop after 270 °C due to the increase in gelation, therefore, whatever is left of unreacted functional group would be trapped within the highly dense 3D network that has been formed. With HNTs addition, the rate of conversion is slower and α of epoxy/HNT at $\alpha \geq 0.3$ requires

higher temperatures for each rate compared to the neat epoxy. Although HNTs hinder the polymerization of epoxy at lower temperatures, they contribute to the resin curing mainly through the presence of -OH groups on their surface, especially at T > 180 °C, and the added HNTs prolong the reaction since the conversion curve levels off at higher temperature value. To evaluate the kinetic parameters of H0 and H10 nanocomposites, KFM analysis with different heating rates is performed in order to find the activation energy (*Ea*) without being limited to a specific reaction type. KFM assumes that *Ea* does not remain constant during a reaction and is considered independent of the temperature program at a particular conversion (using the "iso-conversion principle"). Moreover, the curing process of epoxy resin is assumed as one or multiple-step reaction without parallel reaction steps.

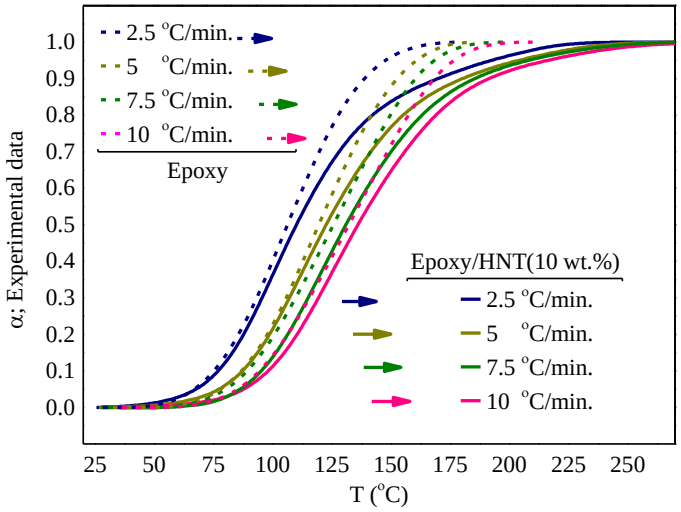

Figure 2.4 Experimental conversion curves at various heating rates for neat epoxy, and epoxy/HNT (10 wt.%) nanocomposites.

Considering this information, conversion-dependent KFM methods such as Friedmann, Ozawa-Flynn-Wall (OFW), and Kissinger-Akahira-Sunose (KAS) are utilized, and Friedman model gives the best fit to the experimental data set (Table 2.3S).

The Friedman master plots along with the iso-conversion lines for H0 and H10 nanocomposites are represented in Figure 2.5. The iso-conversion lines in the epoxy analysis curve are almost parallel to each other and there is a slight deviation from parallelism at α = 0.4, which indicates a change in the kinetic parameters and correlates with the gelation starting point. At high heating rates (e.g., 10 °C/min.), the system reached a 0.4 conversion value (in the chemically controlled reactions) faster than low rates. Another change in the

slope of iso-conversion lines is noticed at the 0.9 conversion value, where the available reaction sites are about to be consumed, and the curing reaction is about to cease. On the other hand, in the case of epoxy/HNT (10 wt.%), the change in the slope of iso-conversion lines took place at α = 0.7. This accords alongside the previous findings and emphasizes the role of HNTs in enhancing the curing at an advanced stage of the diffusion-controlled reaction.

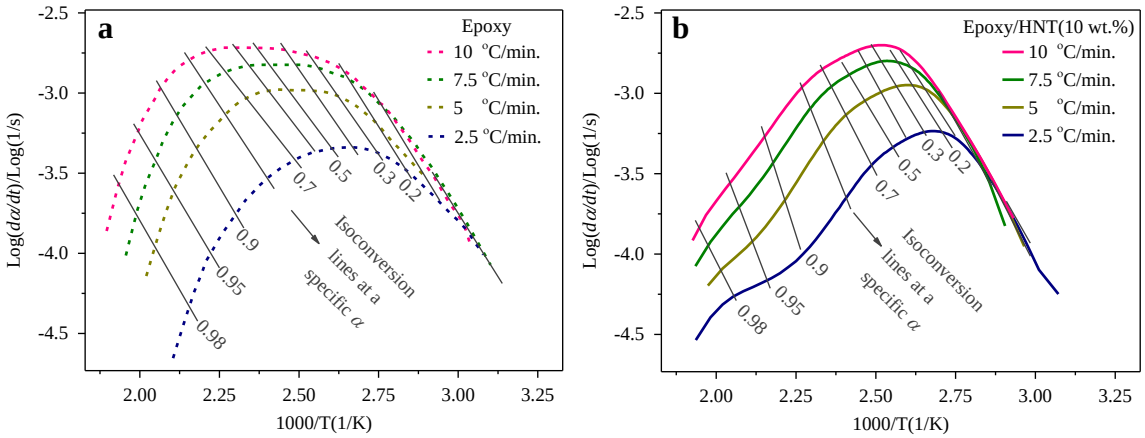

Figure 2.5 Friedman master plots and iso-conversion lines at the different heating rates (2.5, 5, 7.5, and 10 ℃/min.); $0.1 \leq \alpha \leq 0.99$ for (a) epoxy, and (b) epoxy/HNT(10 wt.%).

Ea variations as a function of conversion for epoxy and epoxy nanocomposites are presented in Figure 2.6. In regions with $\alpha \leq 0.3$, the *Ea* of H0 is slightly higher than that of H10 since the presence of HNTs lowers the free volume and provides additional reaction sites. At $0.3 < \alpha < 0.6$, *Ea* remains nearly constant for both H0 and H10, then it increases gradually until the end of the reaction. Besides, *Ea* of the nanocomposite has a cross-over with *Ea* of epoxy above α = 0.3 because as the network grows while still being in the temperature range below 200 ℃, HNTs can hinder the movement of the reacting moieties [27]. Besides, the presence of -OH-containing molecules makes the catalyzing role of amines in the ring-opening reaction weaker [43]. At temperatures higher than 200 ℃, the unreacted amine groups and epoxide rings (trapped within the polymeric network [26]) react with -OH groups of HNTs, thus forming amidic and etheric bonds. However, since HNTs distribution and HNTs clusters' sizes are not homogenous, the extent to which these lateral reactions occur varies, therefore, the standard deviation values are high at $\alpha \geq 0.8$ for H10.

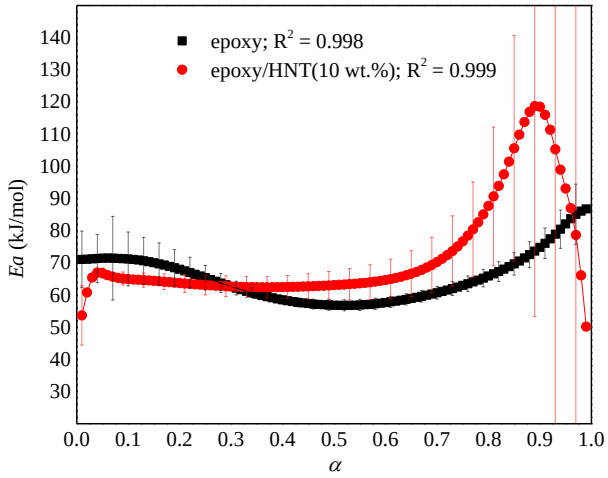

Figure 2.6 Activation energy (*Ea*) variations as a function of conversion (α) for epoxy and epoxy/HNT(10 wt.%) with dynamic measurements at 2.5, 5, 7.5, and 10 °C/min.

HNTs tend to agglomerate with time even after the gelation point, affecting the size and distributions of clustered HNTs in the cured nanocomposite. Hence, by studying the cure behavior at various concentrations of HNTs, a preliminary understanding related to the effect of HNTs cluster size on the diffusion constant for curing reaction can be achieved. $\Delta H_{tot.}$ between 20 °C and 270 °C, T_{onset}, T_{endset}, ΔT, and T_g of epoxy/HNT (0, 1, 2, 5, and 10 wt.%) are given in Table 2.2. The absence of an increasing linear trend in $\Delta H_{tot.}$ might be attributed to the following factors: (i) the diffusion of epoxy segments into the HNTs structure during the early stages of crosslinking; (ii) the bonding between the -OH groups on the surface of HNTs and the epoxy resin; and (iii) the closer packing of functional groups during polymerization. At low amounts of HNTs, the inner lumen space is expected to be more accessible (i.e., 1 and 2 wt.%), hence facilitating the diffusion of oligomers into the HNTs. At higher weight ratios, the agglomeration of HNTs causes a poor capillary effect, which corresponds to a less accessible lumen space. Nevertheless, the combined effect of -OH groups at the outer surface of HNTs and the increase in the packing of growing polymeric chains may lead to higher values of ΔH_{tot} as in the case of 5 and 10 wt.%.

In order to find the curing reaction parameters, Kamal and Sourour (KS) model given in Equation 2.3 is used for analyzing the effect of the HNTs concentration on the curing reaction of the epoxy resin,

$$\frac{d\alpha}{dt} = (K_1 + K_2\alpha^m)(1-\alpha)^n \tag{2.3}$$

where the first rate-constant (K_1) and the exponent (n) describe the n-th order noncatalytic reaction and the second rate-constant (K_2) and the exponent (m) describe the autocatalytic contribution of the reaction. K_1 and K_2 can be described by the Arrhenius type equation (2.4) as;

$$K_{1,2} = A_{1,2} \exp\left(-\frac{E\alpha_{1,2}}{RT}\right) \tag{2.4}$$

where Ea_1, Log (A_1), Ea_2, and Log (A_2) are activation energies and rate constants for the noncatalytic and autocatalytic reactions, respectively.

To calculate the diffusion coefficient near T_g, Equation 2.3 is modified through using diffusion control equation (WLF, Williams-Landel-Ferry) [42] so that it has additional constants of Log($K_{diff.}$), C_1, and C_2 with K_{diff} being the diffusion-controlled reaction rate constant, C_1, and C_2 being general constants. These properties (Ea_1, Log (A_1), Ea_2, Log (A_2), m and n) show a similar trend prior to or after applying diffusion control equation (Table 2.4S).

Table 2.2 $\Delta H_{tot.}$, T_{onset}, T_{endset}, ΔT, T_p and T_g of epoxy/HNT (0, 1, 2, 5, and 10 wt.%).

HNT wt/%	**$\Delta H_{tot.}$ (J/g)**	**T_{onset} (℃)**	**T_{endset} (℃)**	**ΔT (℃)**	**T_p (℃)**	**T_g (℃)**
0	216.4	54	232	178	128	66
1	335.3	58	218	160	129	66
2	310.9	54	210	156	126	65
5	343.2	56	213	157	127	66
10	321.3	70	235	165	124	66

The polymeric network evolves in a fairly regular manner, and the presence of HNTs and HNT clusters changes the topology of the polymeric structure by creating inhomogeneous crosslinking in the polymeric network. The more the HNTs amount is, the more lumen space and the less free volume between the chains are available for the polymerization reactions. Table 2.3 provides a comparison of some of the polymerization reaction constants. The pattern of variation in Ea_1 and Log(A_1) values as a function of HNTs weight percentage are similar.

We will initially discuss the effect of HNTs on the chemically controlled reactions for the temperature range below 40 ℃. In general, for epoxy/HNT(0, 1, 2, 5, and 10 wt.%)

nanocomposites, the values of Ea_1 are descending in the order of 1 wt.%, 0 wt.%, 5 wt.%, 10 wt.%, and 2 wt.%. In the H0 case, after the start of the crosslinking and with the progress of the reaction, the entanglement of the polymeric chains occurs, and the probability of entrapment of the reactive sites (within the polymeric network) increases with time. For the H1 specimen, the presence of HNTs lowers the free volume and slows down the chemically controlled reaction due to the hindrance of the reactive sites, and thus, Ea_1 increases.

As for H2, the free volume becomes even less compared to H0 and H1, and the chemical functional groups are pushed closer toward each other which relatively facilitates the reaction. Polymeric chains are longer and prone to entanglement further. Also, HNTs bring additional reactive sites (-OH groups) to the system. All these factors drop-down Ea_1 drastically (one order of magnitude) and speed up the reaction. In H5 case, the hindrance and entrapment of reactive site is more prominent and HNTs aggregate into bigger clusters compared to the previous samples with lower concentrations. These two effects might create sub-zones within the reaction system in which the polymeric chains grow in all directions surrounded by what is left from the unreacted liquid monomers. The ratio of $-NH_2$: -OH is 100:105 and this affects the local topology of the polymer network by making it more cross linked compared to H2. Additionally, since the total available inner lumen space of HNTs is larger, the capillary effect prevails. The outcome from all these effects is a reaction speed that is close to that of H0 but with 5% lower Ea_1.

In H10, a combination of the mechanisms that are discussed above for H2 and H5 samples occurs simultaneously. Additionally, there are the big clusters (i.e., that mark subzone), the entrapment of the functional sites, and diffusion that is driven by the capillary effect. On the other hand, there is the effect of lowering the free volume within these subzones and bringing the functional groups closer to each other and increasing the -OH groups on HNTs surfaces.

Table 2.3 Activation energy (Ea_1), Log of the pre-exponential factor (Log(A_1)), and equivalent ratio of functional groups (-NH_2 : -OH) for epoxy/HNT(0, 1, 2, 5, and 10 wt.%).

Sample	**H0**	**H1**	**H2**	**H5**	**H10**
HNTs wt.%	0	1	2	5	10
-NH_2: -OH	100: 100	100: 101	100: 102	100: 105	100: 110
Log (A_1)	- 0.67	- 0.75	- 0.41	- 0.66	- 0.45
Ea_1	1886	1894	197	1788	1787
Log (A_2)	1.73	1.7	1.35	1.71	1.65
Ea_2	24.5	23.9	23.5	24.3	24.5
Log ($K_{diff.}$)	-2.75	-4.05	-7	2.66	-6.24

These combined mechanisms result in speeding up the reaction similar to H2 case (i.e., $\text{Log}(A_1)_{H10} = \text{Log}(A_1)_{H2}$) and lowering the Ea_1 similar to H5 case (i.e., $(Ea_1)_{H10} = (Ea_1)_{H5}$). To recapitulate, the hindrance of moieties movement due to the reduction in free volume reduces Ea_1 by 90% when the ratio of -NH_2: -OH is 100:102, and by 5% when the ratio of -NH_2: -OH is 100:105 and 100:110.

The first chemical reaction in Figure 2.7 shows how -OH groups are created as a result of the noncatalytic "ring-opening reaction" while the second one indicates how the created -OH participates in the new "ring-opening reaction", which is also referred to as the autocatalytic mechanism that can create side cross linking in the polymeric chain. Upon comparing Log (A_2) and Ea_2 values of all samples in Table 2.3 to understand the effect of HNTs weight ratio on the autocatalytic reactions at temperatures lower than 40 °C, it is found that all samples have similar Log (A_2) apart from the case of H2 sample. When 2 wt.% of HNTs are used, the speed of the autocatalytic reaction is the lowest even though it has the lowest activation barrier (the lowest Ea_2). This indicates that when the ratio of -NH_2: -OH: is 100:102, the reduction in the free volume causes the chain growth to proceed in favor of increasing the length of polymeric chains rather than forming more branched cross linking.

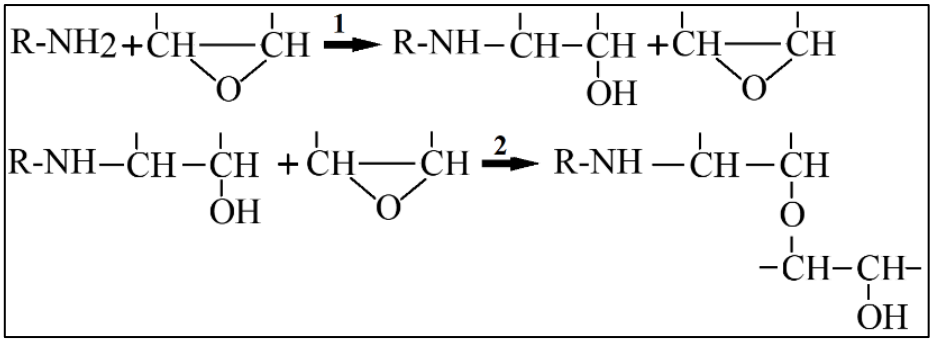

Figure 2.7 Ring opening reactions 1 and 2 during polymerization process.

Log ($K_{diff.}$) is correlated with the speed of the diffusion dominated reactions and gives insights regarding the effect of HNTs on the diffusion-controlled reactions at temperatures higher than 40 °C. In H1 case, Log ($K_{diff.}$) has a smaller value compared to H0, indicating that the diffusion of moieties is hindered by the presence of 1 wt.% of HNTs, and this effect is more noticeable in H2. At higher concentrations of HNTs as in the case of H5 sample, subzones are formed due to the big clusters of HNTs, which promotes diffusion-controlled reactions and leads to an increase in Log ($K_{diff.}$). In H10, the diffusion-controlled reactions slow down similar to H2 case since higher amount of HNTs within subzones obstructs diffusion paths.

2.3.2.2. Rheological measurements

The polymeric network contains elastically active chains between junction points, and the presence of HNTs during the network formation process alters the topology of the final network. For further understanding of the relations between the structure of the chains and the properties of the mixtures, rheological measurements in oscillatory mode have been performed. Figure 2.8 presents the variation of tan δ (computed as the ratio of dynamic loss modulus (G″) to dynamic elastic modulus (G′) as a function of time. At the beginning of the polymerization for all samples, G″ increases with a higher rate than G′. The peak point of the tan δ graph ($(\tan \delta)_p$) corresponds to the stage where the relative difference between G′ and G″ moduli are the largest. Afterwards, G′ increases at higher rate than G″, indicating the onset of vitrification where the chemically controlled reactions are still dominant. As the cross-linking progresses, the critical gelation point ($t_{gel.}$) is reached, where the diffusion mechanism becomes dominant. $t_{gel.}$ is found from the intersection of shear elastic modulus G′ and shear loss modulus G″ graphs in Figure 2.6S and corresponds to a point where the ratio of G″/ G′=1, indicating the time needed to reach the stage where the polymeric system is mostly

cross-linked solid phase surrounded by liquid polymeric phase. After $t_{gel.}$, the liquid regions start to diminish, and the completion of the network formation accelerates rapidly until the moduli approach their equilibrium values, as given in Figure 2.7S. In all samples, the tan δ graph does not exhibit a sharp peak because the distribution of moieties is not homogenous throughout the whole system for each sample and the system needs time to attain a certain degree of cross-linking. Figure 2.8 also includes the values of $\boldsymbol{I}$ **= t at (tan δ)$_p$ – t$_{gel.}$** interval and $t_{gel.}$ for all samples. The highest $(\tan \delta)_p$ belongs to H0. The addition of rigid high moduli material like HNTs increases the elastic character of the system so that $(\tan \delta)_p$ has a lower value, which corresponds to a lower damping effect.

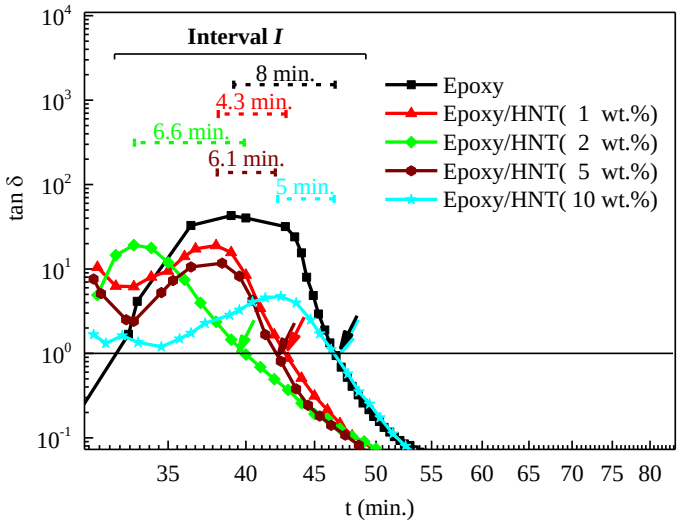

Figure 2.8 tan δ for epoxy/HNT(0, 1, 2, 5, and 10 wt.%) with $\boldsymbol{I}$ intervals indicated by horizontal dashed lines, and $t_{gel.}$ indicated by arrows at the intersection of each graph with the horizontal line at tan δ =1.

Table 2.4 presents the time at $(\tan \delta)_p$, ($\boldsymbol{I}$), and $t_{gel.}$ for H0, H1, H2, H5, and H10. The length of interval $\boldsymbol{I}$ can be correlated to the polymeric chains' length. In a liquid polymeric system, before $t_{gel.}$ (where the network contains chains that are growing with a solid-like phase surrounded by a liquid of unreacted substrates), the longer the polymeric chains, the more they tend to entangle, leading to the extension of $\boldsymbol{I}$.

The value of complex viscosity $|\mu^*|$ indicates the sol fraction of the system. Higher values of $|\mu^*|$ correspond to smaller sol fraction. Figure 2.9 shows the variation of $|\mu^*|$ as a function of time for different HNTs ratios where $t_{gel.}$ are also indicated on the corresponding

graphs using vertical arrows. At the beginning of the polymerization reaction, as the chain growth begins, $|\mu^*|$ raises slowly due to the increase in the molecular weight of the polymer.

Table 2.4 t at $(\tan\delta)_p$, interval $\boldsymbol{I}$,$t_{gel.}$ and complex viscosity at the gelation point $|\mu^*|_{gel.}$ for H0, H1, H2, H5, and H10.

Sample	**H0**	**H1**	**H2**	**H5**	**H10**
$\boldsymbol{(\tan\delta)_p}$ **(min.)**	38.6	38.5	33.4	35.9	41.5
$\boldsymbol{I = (\tan\delta)_p - (t_{gel.})}$ **(min.)**	8	4.3	6.6	6.1	5
$\boldsymbol{t_{gel.}}$ **(min.)**	46.6	42.8	40.0	42.0	46.5
$\boldsymbol{\|\mu^*\|_{gel.}}$ **(Pa.s)**	308	272	1133	198	271

Pristine epoxy has $|\mu^*|_{gel.}$ value around 300 Pa.s, and H1 sample has a lower $|\mu^*|_{gel.}$ compared to H0. This correlates with previous data of Log (A_1) and Ea_1 given in Table 2.3. Namely, 1 wt.% of HNTs decreases the free volume and leads to an earlier start of the diffusion-controlled reactions. H2 has the highest value of $|\mu^*|_{gel.}$. Previous findings showed how the free volume in H2 becomes even less compared to H0 and H1, and consequently, the chemical functional groups are pushed closer toward each other. Besides, the speed of the autocatalytic reaction is the lowest in H2 case, therefore, the formation of side cross-linking between polymeric chains is the slowest, in this case, resulting in producing longer polymeric chains compared to H1, H5, and H10. Longer chains lead to more entanglement of the polymeric chains, which leads to higher $|\mu^*|$.

The autocatalytic character of H5 is higher than H2 sample and close to H0. This difference in autocatalytic parameters between H2 and H5 affects the progress of the polymerization reaction under autocatalytic conditions, and in the diffusion-controlled reaction where the reaction products have become less mobile. At this stage, the products of the reaction form molecular clusters, and the reaction is localized in those sites.

The lower the molecular mobility and the stronger the autocatalytic factor, the larger the size of the growing clusters [43]. These phenomena create a kinetic inhibition meaning that the catalysis of the polymerization reaction involves only those molecules that are disposed of on the cluster surface, whereas those inside the cluster are essentially inaccessible. Those molecular cluster forms at concentrations above 2 wt.% and the larger the cluster size, the higher is the total autocatalysis efficiency, which explains the increase in

the autocatalytic character in H5 compared to H2. However, with these occurrences, the possibility of the formation of inhomogeneous structures (i.e., phase formations) becomes higher.

$|\mu^*|_{gel.}$ of H10 is slightly higher compared to H5 (it is almost equal to $|\mu^*|_{gel.}$ of H1) with shifted $t_{gel.}$ toward later time. In H10 system, sub-zones with higher HNT concentrations are formed. This adds additional inhibition mechanism to the system: At the initial stages of polymerization, the amines ($-NH_2$) have basic character and act as proton-donors. They contribute to the ring-opening reaction by attacking the epoxide ring (i.e., nucleophilic attacking mechanisms) (Figure 2.7). The basicity of the amines is low, and it becomes weaker in the presence of -OH containing molecules such as HNTs. Since the ratio of $-NH_2$ to -OH decreases at higher concentrations of HNTs, the concentration of proton-donor reduces leading to a decrease in reaction rate. Moreover, higher amount of HNTs brings more intramolecular reactions with the functional groups in the system, and this causes the occurrence of ineffective cycles of polymerization. Consequently, this combination of acceleration and inhibition mechanisms makes the $|\mu^*|$ profile of H10 similar to H0 and the $t_{gel.}$ shifts towards later times.

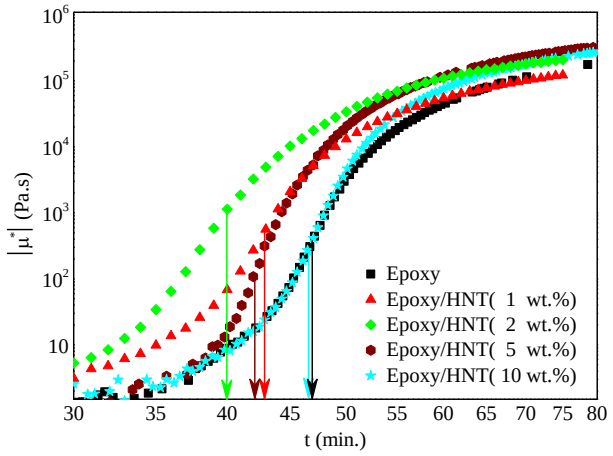

Figure 2.9 The evolution of $|\mu^*|$ with time, with arrows indicating $t_{gel.}$ for each sample.

2.3.3. Characteristics of epoxy/HNT nanocomposites

2.3.3.1. Effect of HNTs concentration on the network composition

The p-phenylene groups in the DGBEA resin do not participate in the ring opening reaction, and their corresponding FTIR peaks almost do not change or slightly decrease in intensity after polymerization (Figure 2.10a) and can be used as internal standards in the

system [44]. The peaks corresponding to epoxide rings in the resin and the primary and secondary amines in the hardener decrease in intensity and almost disappear due to participation in the ring-opening polymerization reaction (Figure 2.10b and 2.10c).

FTIR spectrums of pristine HNTs and cured epoxy/HNT (0, 1, 2, 5, and 10 wt.%) nanocomposites are presented in Figure S2.8 in Appendix I. The characteristic peaks for the epoxide ring at 970 cm^{-1} and for amines at 1590 cm^{-1} are chosen to estimate the consumption of epoxides and amines during polymerization. By dividing the intensity of each epoxide ring and amines by the intensity of the internal standard, it is possible to estimate the consumed amounts of these functional groups as presented in Figure 2.11.

These FTIR spectrums are presented as transmittance percentage (Transmittance %) value therefore, in this perspective, the lower the transmittance value, the higher the concentration and the less the consumption of the functional group during the polymerization. According to Figure 2.11, the consumption of epoxide and amine groups is the highest in epoxy/HNT(5 wt.%) system in the fully cured specimens. This agrees with the previous finding about the total autocatalytic efficiency being the best at 5 wt.% of HNTs. The stoichiometry of the functional groups in H5 leads to the growth of larger polymeric clusters, locally within the cross-linked network, compared to the rest of the studied systems. It is seen in Table 2.4 and Figure 2.9 that H5 has the second earliest $t_{gel.,}$ and the lowest $|\mu^*|_{gel}$. These factors decrease the miscibility between the HNTs-rich region and the epoxy-rich region in the final cured composite.

The inhomogeneity in the cured epoxy/HNT(5 wt.%) specimens is more prominent compared to the rest of the studied concentrations. To elaborate more on this point, the region from 3500 cm^{-1} to 3750 cm^{-1} is presented in Figure 2.10d. There are two characteristic peaks of HNTs at 3625, and 3694.4 cm^{-1}. epoxy/HNT(0, 1, and 2 wt.%) spectrums do not have the characteristic peaks of HNTs, and those peaks are only present in epoxy/HNT(5, and 10 wt.%) nanocomposites.

At lower concentrations of HNTs (i.e., 1 and 2 wt.%) the miscibility between polymer and the nanotubes increases and therefore, the mentioned two peaks of HNTs are absent. As the HNT content increases up to 5 wt.%, segregation between the polymer and HNTs occurs, hence, the peaks are most distinguished compared to other epoxy/HNT nanocomposites.

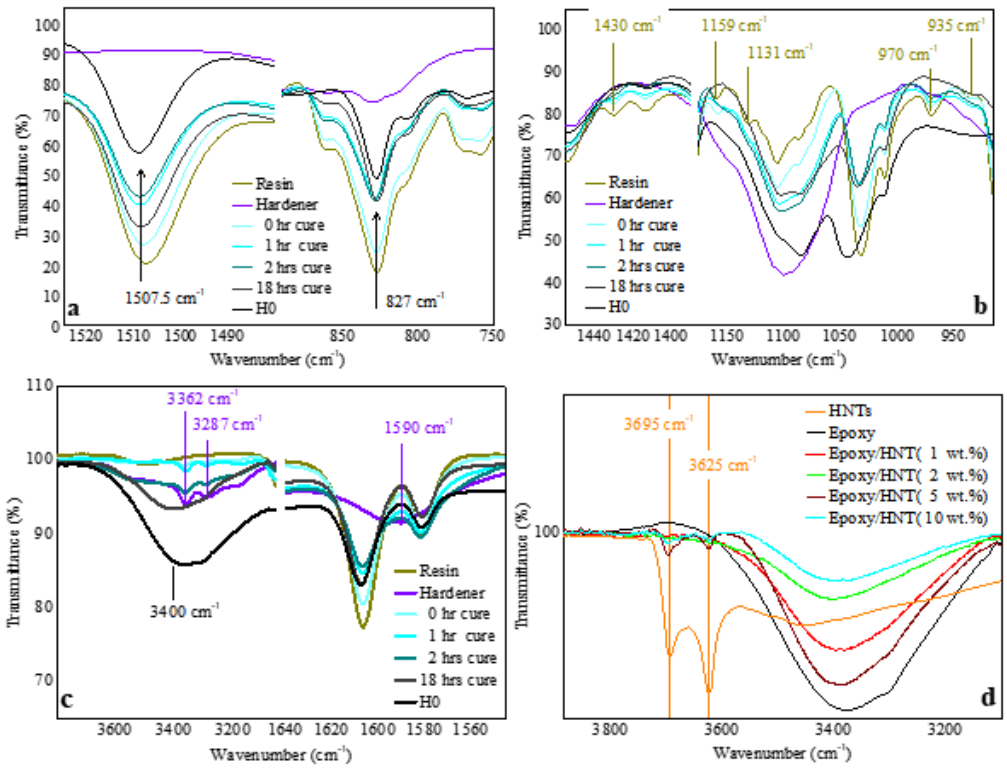

Figure 2.10 (a) Internal standard peaks related to p-phenylene groups transmittance, (b) consumption of epoxide rings, (c) consumption of amine groups for H0 sample; and resin, hardener, resin and hardener mixtures directly upon mixing (0 hr cure), after 1, 2, and 18 hours of cure in room temperature (1 hr cure, 2 hrs cure, and 18 hrs cure). (d) characteristic peaks of HNTs in FTIR spectrums of HNTs, and epoxy/HNT(0, 1, 2, 5, and 10 wt.%).

The intensity of characteristic peaks at 10 wt.% of HNT is smaller than that of H5, indicating that more interaction between HNTs and resin transpires, which can be explained by the etherification reaction between the -OH groups on the surface of HNTs and the epoxy resin polymeric chains.

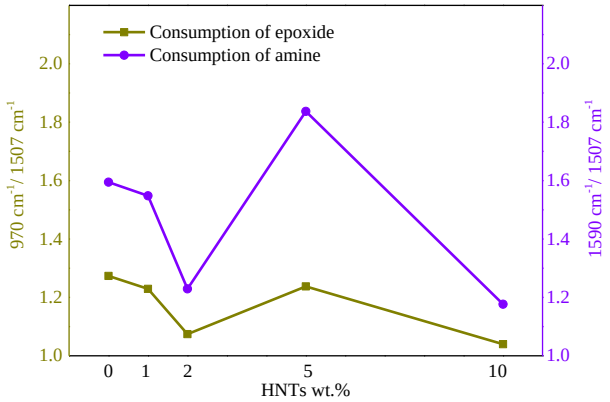

Figure 2.11 Consumption of epoxide and amine functional groups for epoxy/HNT(0, 1, 2, 5, and 10 wt.%) nanocomposites.

2.3.3.2. Thermal stability of epoxy/HNT nanocomposites

The thermal stability of polymeric materials and their resistance to thermal degradation are of great importance in most applications. Table 2.5 presents TGA results of epoxy/HNT nanocomposites at $T_{95\%}$, T at the inflection point ($T_{Inflec.}$), and the char yield at 800 °C. $T_{Inflec.}$ for neat and epoxy/HNT samples were obtained by the Differential Thermal Analysis (DTA) results for neat and epoxy/HNT samples (i.e., by taking the first derivative of the weight loss curve) (inset in Figure 2.12). The minimum temperature in the DTA curve is $T_{inflec.}$, and it indicates the point of the greatest rate of change on the weight loss curve.

The temperature corresponding to the 5 wt.% weight loss ($T_{95\%}$) for H0 is 352 °C. It increased for HNT concentrations from H0.5 to H2 with respect to $T_{95\%}$ of H0. This indicates an improvement in the thermal stability with the addition of a low amount of HNTs because silicon atoms in HNTs (in the form of silicon oxide or other oxides) serve as the protection or coating layer to prevent further thermal degradation or combustion of the matrix [45]. On the other hand, there is a drop in $T_{95\%}$ values for H5 and H10. Since the surface of HNTs contains certain amounts of impurities and solvents, increasing the concentration brings about higher impurity contents that tend to desorb at slightly lower temperatures, leading to lower $T_{95\%}$ values. Similarly, $T_{inflec.}$ for H0 is 382 °C, where it increase slightly for H1, and H2 (indicating better thermal stability), afterward it decrease for H5 and H10 compared to H0. The slightly lower $T_{inflec.}$ can be attributed to the variation to evaporation/decomposition of any solvents/impurities within HNT cavities as explained previously. The char yield of the nanocomposites increased with HNT concentrations. This correlates with previous results in

Figure 2.2, where HNT lost around 12 wt.% from the total weight after heating up to 1000 °C. 88 wt.% of the initial weight of HNTs were left in the sample toward the end of the TGA test (i.e., at 800 °C), thus the final char yield increase for epoxy/HNT nanocomposites from Ho toward H10.

Table 2.5 TGA results of epoxy/HNT nanocomposites at $T_{95\%}$, T at the inflection point ($T_{Inflec.}$), and the char yield at 800 °C.

	$T_{95\%}$ (°C)	$T_{Inflec.}$ (°C)	Char yield (wt.%) at 800 (°C)
HNT	462	462	88
Epoxy	352	382	6.18
Epoxy/HNT(0.5 wt%)	353	381	6.76
Epoxy/HNT(1 wt%)	354	383	7.01
Epoxy/HNT(2 wt%)	354	383	9.06
Epoxy/HNT(5 wt%)	351	382	9.53
Epoxy/HNT(10 wt%)	348	381	11.65

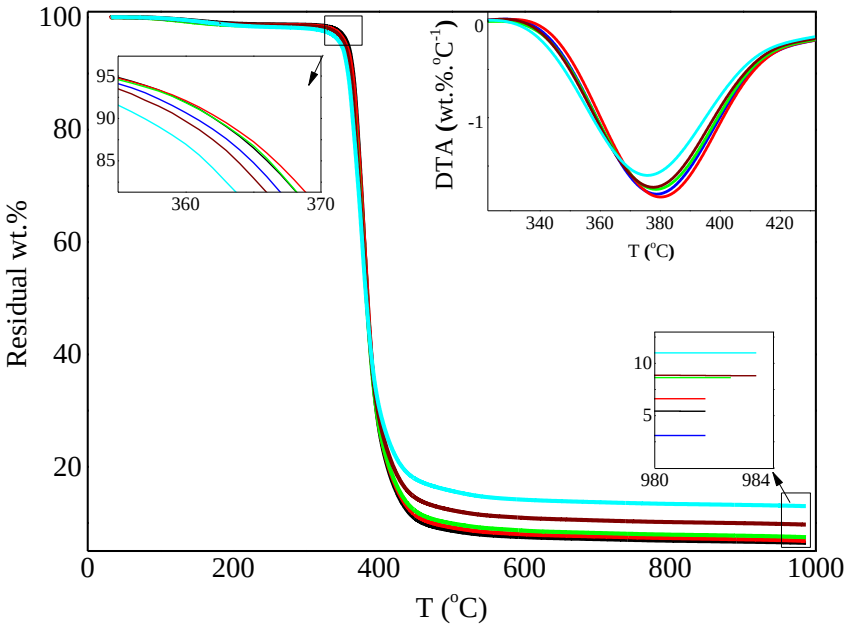

Figure 2.12 TGA and inset: DTA thermograms of epoxy/HNT (0 ,0.5, 1, 2, 5, and 10 wt.%) nanocomposites.

2.3.3.3. Mechanical properties of epoxy/HNT nanocomposites

Figure 2.13 represents the dynamic–mechanical properties like storage modulus (G′), loss modulus (G″), and tan δ for pristine and HNT-based nanocomposites. G″ is associated with the viscous properties of a polymeric material and represents energy dissipation during a cyclic load while the storage modulus is a measure of how much energy should be imposed

into the sample in order to deform it. Dynamic–mechanical properties of epoxy/HNT composites notably change depending on the amount of the fillers. G′ increases with the increase in the weight fraction of HNTs at low temperature, followed by a sharp drop, as the temperature increases, to very low values in the vicinity of the glass transition temperature (marked with a vertical dash-line on the graphs at 66 °C). To be more specific, the integration of 10 wt.% of HNTs into the epoxy resin significantly alters both elastic and the viscoelastic behaviors of pristine epoxy resin by, for example raising G′ from 2388 MPa up to 3540 MPa. It is important to point out that G″ of all specimens have relatively constant values at low temperatures and rise all together to a peak value, which corresponds to the maximum energy dissipation per unit cyclic loading. It is seen that both specimens with 5 and 10 wt.% HNTs are prominent in higher heat dissipation as a function of temperature at both elastic and rubbery regions. Two important factors which may affect the amount of heat dissipation corresponding to a higher value of loss modulus are (i) the filler weight fraction and (ii) the number and size of filler clusters. Such an increase in the presence of fillers enhances chain flow by modifying and facilitating the conformational pathway of chains to return to their equilibrium conformations, thereby increasing the energy dissipation under the influence of dynamic load. The increase in the cluster size of HNTs promotes polymer-filler and filler-filler slippages, thus leading to more heat dissipation and, in turn, higher G″. Essentially, the higher the peak value of G″, the more intermolecular bond is broken. To this end, it can be inferred that the specimen with 10 wt.% HNTs have the highest peak value of G″ due to their largest filler content. On the other hand, the specimen with 5 wt.% HNTs have the second highest loss modulus indicating that for this weight fraction the fillers are more clustered both in size and number. G″ curve for 10 wt.% HNTs specimen broadens towards the right more than the others, implying the internal friction between the resin and the filler. The presence of the HNTs did not significantly alter the peak temperature of tan δ which corresponds to T_g of the system (68 °C) except for 2 and 10 wt.% of HNTs, which are slightly decreased (63 °C) and increased (73 °C), respectively. Another important effect of HNTs on the epoxy resin can be discussed by referring to the maximum height of the tan δ peak. It can be seen that the presence and content of HNTs do not noticeably change the tan δ peak demonstrating that HNTs do not affect the damping response of epoxy resin. To conclude, despite including a high amount of "rigid and clustered" HNTs, the mechanical performance

of the nanocomposite under cyclic load still show improvement due to the strong interfacial interaction between polymer chains and HNTs which is formed during the curing (polymerization) stage.

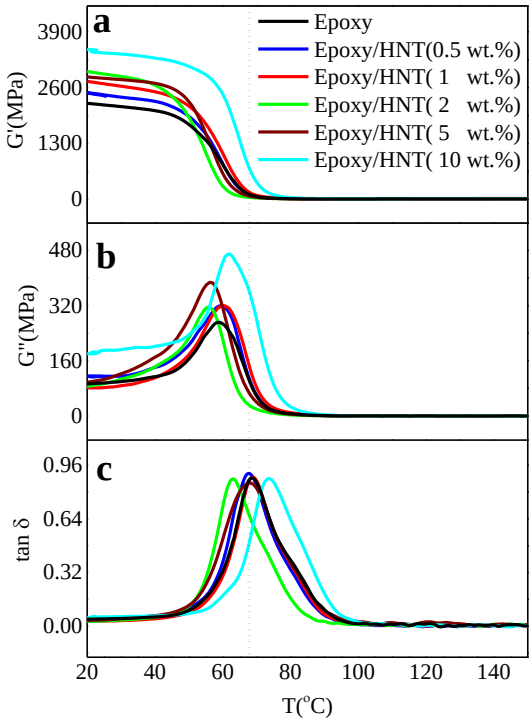

Figure 2.13 (a) Storage modulus (G′), (b) loss modulus (G′′), (c) tan δ graphs for epoxy/HNT (0, 0.5, 1, 2, 5, and 10 wt.%) nanocomposites.

Figure 2.14a shows representative stress-strain curves for neat epoxy and epoxy/HNT nanocomposites for three-point bending test. Additionally, Figure 2.14b compares the average values of flexural strength ($\bar{S}$), strain at the maximum load ($\bar{\varepsilon}$), and flexural modulus ($\bar{E}$) for epoxy/HNT nanocomposites with their counterparts for the neat epoxy system. Similar to dynamic-mechanical properties, the flexural modulus increases with the rise in the HNTs weight fraction except in the case with 2 wt.% HNTs. $\bar{\varepsilon}$ decreases almost linearly with the increase in HNTs amount. By the addition of 0.5, 1, and 2 wt.% HNTs, specimens showed slightly higher strain values compared to pristine cases. As the addition of small amount of HNTs in the resin matrix initiates a plasticization effect by softening the polymeric chains, consequently leading to a larger strain value. At 5 and 10 wt. % of HNTs values of $\bar{\varepsilon}$ decreases compared to $\bar{\varepsilon}$ of H0, because the stiffer the polymer gets with the incorporation of a nano-filler, the smaller the strain will be at the maximum load.

However, the trend followed by the $\bar{S}$ is rather different from that of the $\bar{\varepsilon}$ and $\bar{E}$ such that there is a V-shaped variation of the $\bar{S}$ as a function of HNTs weight fraction while the lowest strength value corresponds to 2 wt.%. This behavior can be explained by referring to the possible toughening mechanisms. Note that depending on the HNTs concentration in the resin system, there can be a micro- or a macro- toughening mechanism. At lower HNTs concentrations (i.e., 0.5 and 1 wt.%), there are a higher amount of well-dispersed nanotubes, which could contribute to the load-bearing capacity by micro-scale toughening mechanisms such as the pull-out and the breakage of nanotubes. By further increasing the weight fraction of the nanotubes up to 2 wt.%, the density of the isolated nanotubes in the nanocomposite decreases, and the number of HNTs clusters increases [46]. HNTs clusters form crack initiation points, and it is found from the curing study in previous sections that the polymeric network is less cross-linked in H2 compared to H1, H5, and H10. These two factor combined, lead to lowers $\bar{S}$ for H2 compared to H1, H5, and H10. At higher concentrations (i.e., 5 and 10 wt.%), the size of these clusters grows further, and the macro-scale toughening mechanism becomes more dominant, which results in notable improvement in flexural strength and modulus. Albeit a relatively large variation in the values of ($\bar{S}$) for both epoxy and epoxy/HNT (2 wt.%) samples (for each concentration, four different batches are tested, wherein each batch is composed of three specimens), these results still provide important insight about deformation under flexural load. For instance, the epoxy/HNT(2 wt.%) specimen with the highest maximum strength shows the lowest flexural modulus compared to 0.5 and 1 wt.% HNTs/epoxy nanocomposites, indicating that 2 wt.% of HNTs causes the highest plasticization effect compared to the rest of the HNTs ratios. The distinct behavior of 2 wt.% HNTs in terms of the abovementioned mechanical characteristics will be elaborated in the coming section by referring to the types of the formed bonds and the distribution of HNTs in the resin system.

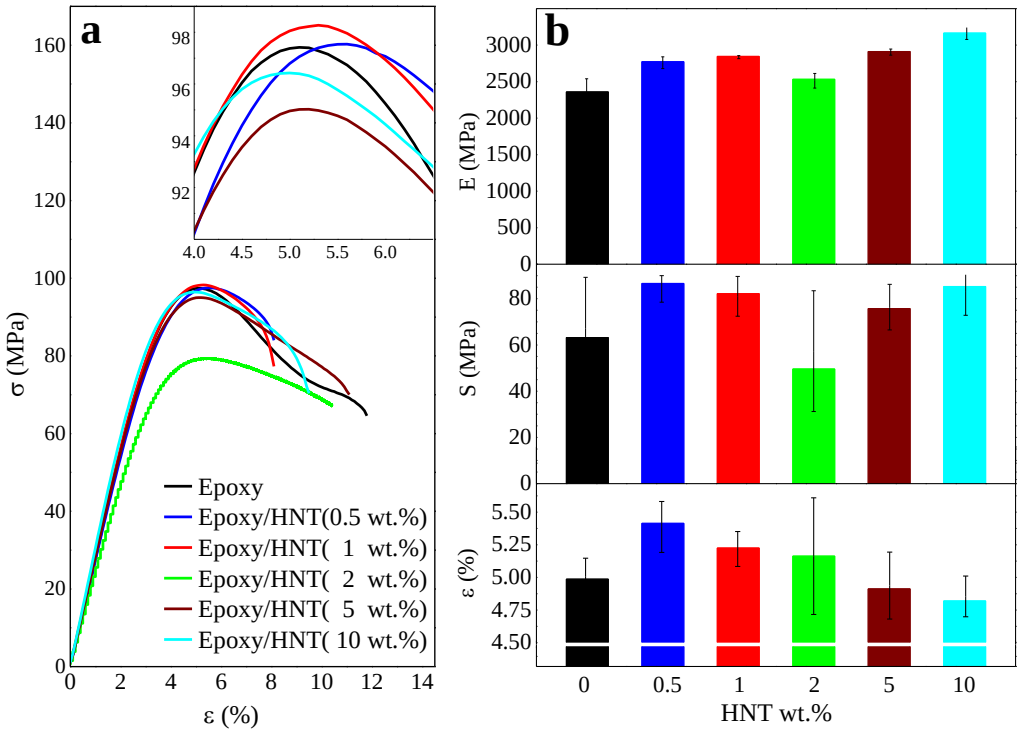

Figure 2.14 (a) stress-strain curves of epoxy/HNT nanocomposites during 3-point bending test, inset: magnified part around the ultimate flexural strength point, and (b) bar graphs of flexural strength ($\bar{S}$), strain at maximum load ($\bar{\varepsilon}$), and flexural modulus ($\bar{E}$) for epoxy/HNT nanocomposites.

2.3.3.4. Altering deformation mechanisms as a function of HNTs concentration

To further investigate the effect of HNTs amount and dispersion in the matrix on the morphology of the fracture surfaces, a detailed fractographic analysis of the surface of the fractured specimens is performed after three-point bending test, and the results are presented in Figure 2.15 and 2.16. The fracture surface of neat epoxy is seen in Figure 2.15a as smooth surfaces with multiple river lines and cusps, which are typical features of brittle fracture for epoxy resin specimens.

The integration of HNTs to the polymeric matrix interrupts the effective cross-linking of the polymer chains during polymerization and, in turn, promotes additional deformation mechanisms under stress such as crack pinning and deflection, and crack growth across and around the HNT clusters. The fracture surface of HNT-reinforced samples appears rougher than its counterpart in the pristine epoxy specimen. HNTs clusters in epoxy/HNT(0.5 wt.%) fracture surface can be seen as white dots in Figure 2.15b. Due to the strong localized adhesion between the agglomerated HNTs and the epoxy resin, HNTs pin the crack, stop its growth and leave a drop-like imprint at its location.

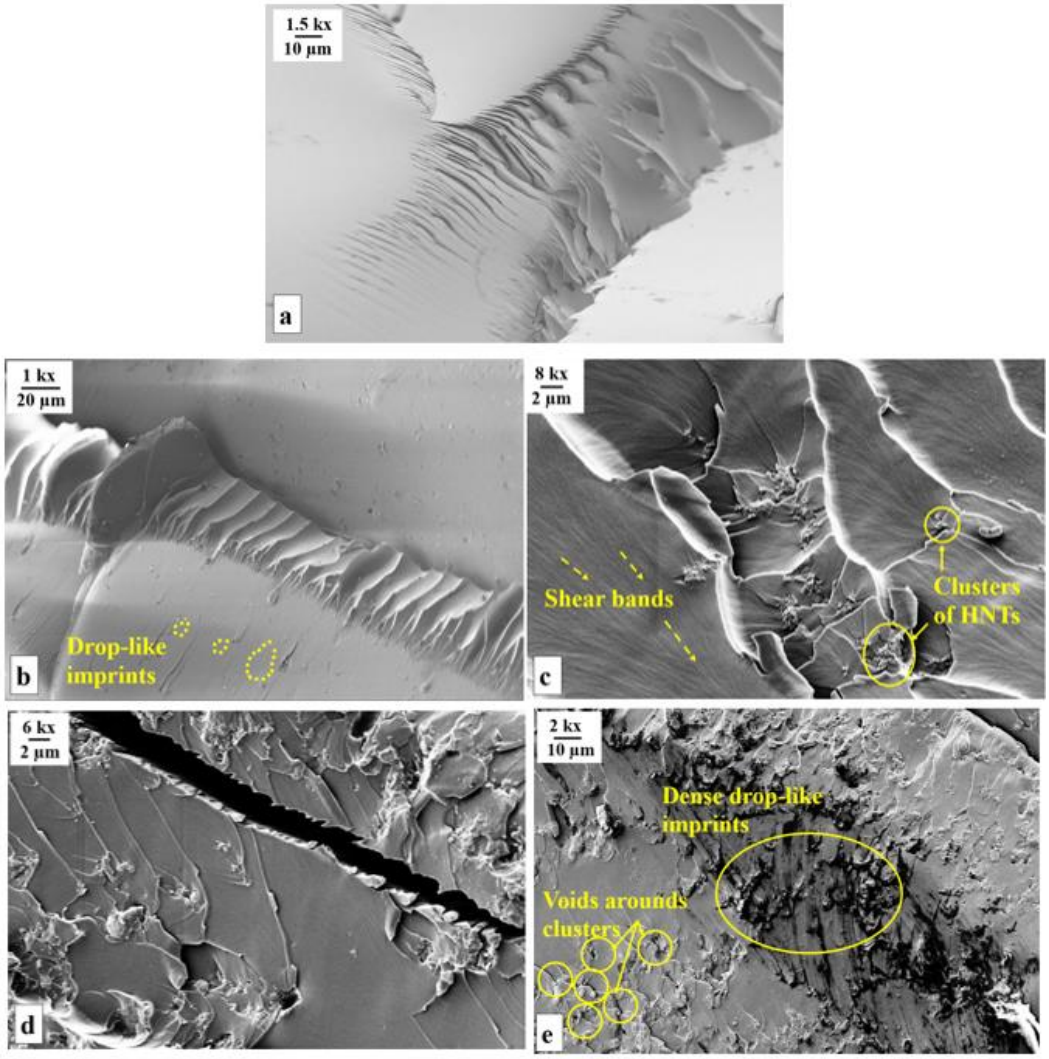

Figure 2.15 SEM micrographs of fracture surface of epoxy/HNT (a) 0 wt.%, (b) 0.5 wt.%, (c) 1 wt.%, (d, e) 2 wt.%.

For specimens with higher HNTs concentrations, fracture behaviour becomes much more complex with multiple fracture planes. As seen in Figure 2.15c, epoxy/HNT(1 wt.%) specimens have more textured fracture surfaces, and well-distributed HNTs with the size of 2-3 μm result in shear dominant deformation. Those clusters are large enough to stop the movement of polymeric chain segments without the formation of numerous micro-cracks (Figure 2.15d and 2.15e). Increasing the HNTs weight fraction up to 2 wt.% results in an increase in the size and the density of the clusters, and based on the earlier curing kinetic effects, it is found that this system contains longer segmental chains compared to the rest of the studied concentration. These factors slightly ameliorate the strain at maximum load (Figure 2.14) at the expense of promoting stress concentration points at higher stress levels,

which expectedly lowers the flexural strength of the nanocomposite compared to the neat epoxy. At higher weight ratios of HNTs, in epoxy/HNT(5 wt.%) nanocomposites (Figure 2.16a and 2.16b), the crack formation mechanism is altered due to the strong interaction between the bigger HNTs clusters (5-6 μm) and the resin (i.e., a high number of ether bonds). This results in detachment of HNTs clusters from the epoxy matrix with capes and bays features on the main crack edges. Lastly, for epoxy/HNT(10 wt.%) specimens (Figure 2.16c and 16d), HNTs clusters are seen as spheres (varying in diameters and can reach up to 10 μm) and surrounded by shear band formation during matrix deformation in various directions. With a more extensive cluster, the fracture plane can pass through some of the big clusters, and those sliced clusters can be seen clearly on the fracture surface and at the crack's tips.

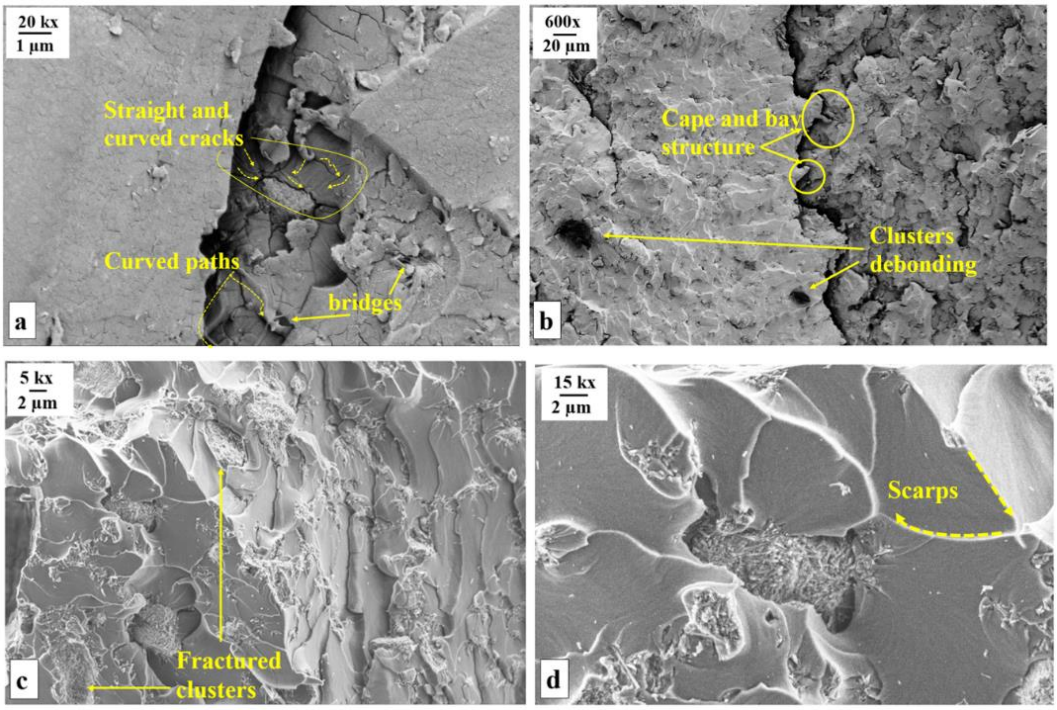

Figure 2.16 SEM micrographs of fracture surface of (a, and b) 5 wt.%, (c, and d) 10 wt.% after three-point bending test.

2.4. Conclusion

In the present work, a comprehensive study was conducted to understand the effect of HNTs on the curing kinetics using DSC experimental data and model-free and model-based kinetic analysis. Analyzing the DSC data showed that HNTs increased the autocatalytic

character of the resin curing reaction and led to an increase in the total heat, especially after the gelation point. By fitting the experimental data to various KFM methods, the Friedman method gave the best fit to the present curing reaction. KS model-based analysis was applied to explore the effect of HNTs concentration on the curing process. It is found that the diffusion constant has increased with the increase of HNTs content in the resin system and was the highest at 5 wt.% HNTs, which facilitates cross-linking reactions. Moreover, the deformation mechanism of epoxy nanocomposites under static and dynamic flexural loads was investigated. To this end, epoxy/HNT nanocomposites were manufactured with various concentrations of HNTs up to 10 wt.%. Thermal, mechanical, and thermomechanical performances of nanocomposites were evaluated in detail. Additionally, the surface of the fracture after three-point bending tests for each of the nanocomposites was examined by SEM. The integration of HNTs improved the mechanical performance of the nanocomposites with no effect on the T_g of the resin. At low concentrations, HNTs pinned the crack and stopped its growth, while the small amounts of HNTs in the resin have produced longer segmental chains, thus providing a plasticization effect on the matrix under flexural load. The deformation mechanism was altered at 5 and 10 wt.% of HNTs, where the deformation of HNT clusters dissipated an additional amount of energy and raised the toughness of the nanocomposites. The outcome of this study is further employed in our following research regarding the use of epoxy/HNT nanocomposites as a matrix for carbon fiber-reinforced polymeric composites.

CHAPTER 3. FEASIBILITY OF EPOXY/HNT NANOCOMPOSITES AS MATRIX FOR STRUCTURAL CAPACITORS

3.1. Introduction

Epoxy is used in printed circuit boards, semiconductor capsules, and structural composites. Epoxy polymer has a 3D cross linked structure that makes it highly resistant to temperature and corrosion, thus it is suitable for use in structural composites. Various types of hardeners can be used with epoxies, such as polyamines, polyamides, anhydrides, or mercaptans, many of which may cause irritation or damage to skin, eyes, and lungs [27]. The use of clay-based nanotubes can reduce the usage of amine-based hardeners. Researchers have reported successful synthesis of epoxy clay nanocomposites using both amine and anhydride curing agents with enhanced properties. HNTs are abundant, cheap, and bio-friendly nano materials. These nanotubes are composed of silicate and aluminate sheets that are arranged in a double layer structure to give tubular morphology with some hydroxyl groups (-OH) on the internal surface of the tube. These surface functional groups are able to break the epoxy ring and contribute to the polymer curing process [27].

To achieve a better dispersion of HNTs within the matrix, surface treatment is used in order to increase HNTs' solubility in organic solvents or in the epoxy based matrix. For example, HNTs can be treated with alkali solutions to enrich the hydroxyl groups of HNTs [47]. Another method was applied by S. Abbasi et al. [39] where they utilized amino silane-based compounds to modify the surface of HNTs.

In order to supply epoxy based polymeric composites with ionic conductivity for use in structural capacitors, researchers add ionic liquid (IL) and lithium salts to the polymeric matrix. To achieve ionic conductivity, it is necessary to control the microstructure at different length scales. One method to achieve that, is to add HNTs to the polymer. In our previous work [48] we explained how the local morphology of the epoxy polymeric network is changed with the change of weight fraction of HNTs. At 2 wt.% of HNTs the polymeric block chains were longer than in epoxy/HNT(% 0, 1, 5 and 10wt.%). At 5 wt.% of HNTs there were regions created by the rapid growth, locally, around a polymeric cluster within the polymeric network. With the addition of lithium salt to the system, Lithium ions will have

the ability to move towards the formed ionic pathways. The presence of HNTs should regulate this movement within epoxy/HNT nanocomposites. EIS is used to obtain the dc-conductivity (σ_{dc}) of the cured nanocomposite. EIS gives real and imaginary parts of the impedance over a wide range of frequencies. Using these data, one method to obtain σ_{dc} considers the following equation,

$$\sigma_{dc} = \frac{L.Z'}{S[(Z')^2+(Z'')^2]} \tag{3.1}$$

Where L is the thickness of the sample, S the effective area of the sample sandwiched between the two electrodes during the measurement, and Z' and Z'' are the real and imaginary part for impedance. A second method to obtain σ_{dc} involves fitting the experimental data to an equivalent electric circuits to obtain the resistance of the sample. Additionally, σ_{dc} and the Ohmic resistance ($R0$) can be obtained from Bode diagram (i.e., modulus of the complex conductivity is plotted versus the frequency (f).

For this research, three factors are investigated: the first factor is the effect of the dispersion method on the epoxy/HNT nanocomposites. Two batches of epoxy/HNT nanocomposites with various concentrations of HNTs (0, 0.5, 1, 2, 5, 10 wt.%) are manufactured using two mixing techniques (bath ultrasonication and probe-sonication). Cured specimens were tested under three-point bending to choose the method that produces specimens with higher flexural modulus. The second factor is the effects of alkaline treatment of HNTs with amino silane group on the resistance to flexural stress. One additional batch of the nanocomposites was manufactured using alkaline modified HNTs (mHNTs) to prepare epoxy/mHNT nanocomposites with (0, 0.5, 1, 2, 5, and 10 wt.%) of mHNTs. The prepared nanocomposites were tested under flexural load and the values of flexural strength and flexural modules are compared with their counterparts in epoxy/HNT. From above mentioned step the third factor which is the effect of weight ratio of HNTs on the flexural properties of epoxy/HNT can be concluded. After exploring the general factors that affect the nanocomposite manufacturing to achieve a better mechanical performance, further modification by adding conductive materials such as ionic liquid (IL) and Lithium perchlorate ($LiClO_4$) took place. EIS measurements were done on epoxy/HNT nanocomposites modified with IL/$LiClO_4$ and conductivity spectra were extracted. Effect of

HNTs on the ionic conductivity of epoxy polymer is compared to IL/$LiClO_4$ additives and explained by fitting the EIS results to Randle circuit.

3.2. Experimental

3.2.1. Materials

HNTs supplied by ESAN, Turkey, and were used without further modification. Two components, DGEBA epoxy (ARALDITE® LY 1564 SP resin and XB 3403 hardener) were purchased from HUNTSMAN. Alkaline modified HNTs (i.e., mHNTs modified by treating in alkali solution [39]) were supplied by YZ. Menceloglu' research group. 1-ethyl-3-methylimidazolium bis(trifluoromethylsulfonyl)imide and $LiClO_4$ (99.99%) were purchased from Sigma Aldrich).

3.2.2. Preparation of epoxy/HNT nanocomposite

The following nanocomposites (epoxy, epoxy/HNT(0.5 wt.%) epoxy/HNT(1 wt.%), epoxy/HNT(2 wt.%), epoxy/HNT(5 wt.%), and epoxy/HNT(10 wt.%) will be referred to as (H0, H0.5, H1, H2, H5, and H10). For epoxy/HNT nanocomposites which use alkaline modified HNTs (mHNT), the following nanocomposites will be prepared: epoxy, epoxy/mHNT(0.5 wt.%), epoxy/mHNT(1 wt.%), epoxy/mHNT(2 wt.%), epoxy/mHNT(5 wt.%), and epoxy/mHNT(10 wt.%), and the produced nanocomposites will be referred to as mH0, mH1, mH2, mH5, and mH10, respectively. All specimens are prepared as detailed in previous work [48]. Figure 3.1 shows two fully cured batches of epoxy/HNT and

epoxy/mHNT.

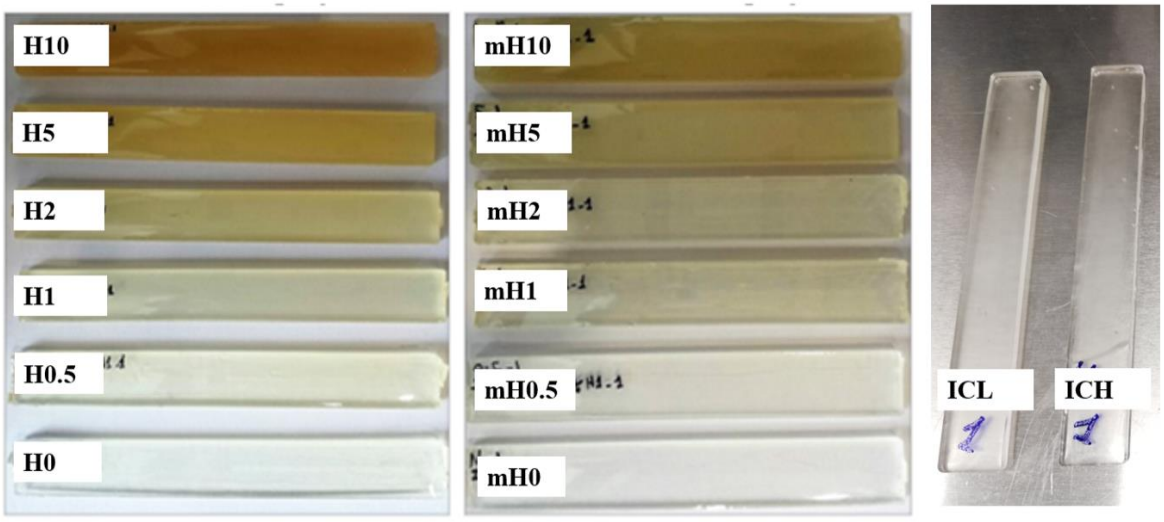

Figure 3.1 Images of produced epoxy, epoxy/HNT and epoxy/mHNT nanocomposites where specimens are ordered by increasing content of HNTs or mHNT upward starting from a) H0 towards H0.5, H1, H2, H5, and H10 and b) H0m toward mH0, mH1, mH2, mH5, and mH10, respectively, and c) ICL and ICH specimens.

Moreover, to prepare the following specimens: epoxy/IL(1%)/$LiClO_4$(1%) (ICL), and epoxy/IL(1%)/$LiClO_4$(1%)/HNT(1%) (ICH), a stock solution of IL/$LiClO_4$ is prepared with the stoichiometric ratios of active material and is added to the uncured epoxy mixture and stirred manually for 2 minutes prior to the degassing step. $LiClO_4$ was added to the IL and stirred by magnetic stirrer overnight in room temperature. Throughout the process all samples were kept under an argon filled glove box with < 0.2 ppm humidity to insure that $LiClO_4$ did not absorb moisture. Produced samples were stored in the glove box before being characterized. Table 3.1 lists the weight ratio of the additives for the prepared samples.

Table 3.1 Weight ratio of IL, $LiClO_4$, and HNTs for H0, H1, ICL, and ICH specimens.

	IL wt.%	**$LiClO_4$ wt.%**	**HNTs wt.%**
H0	-	-	-
H1	-	-	1
ICL	1	1	-
ICH	1	1	1

3.2.3. Characterization

Due to the high aspect ratio of HNTs, Van der Waals bonds are formed, and thus, HNTs may aggregate within the epoxy matrix. This state makes a well dispersion of HNTs an important

requirement for a high-performance composite. Two sonication methods (ultrasonic bath, and probe sonicator) are used to compare the effect of the mixing method on the nanocomposite performance. In order to find which sonication gives better nanocomposites, three-point bending test are conducted on two series of H0, H0.5, H1, H2, H5, and H10 nanocomposites that are prepared either by ultrasonic bath or by probe sonicator.

For the first series of epoxy/HNT nanocomposites, two were mixed using an ultrasonic bath, and another two batches were mixed by probe sonicator. Probe sonicator causes significant increase in the mixture temperature. In order to control the mixture temperature to prevent the early cure of the resin, each mixture was placed in an ice bath during sonication with an interval of 2 minutes every 5 minutes of sonication.

Specimens were mechanically tested under bending load using Instron Universal Testing Machine (5982) equipped with a static load cell of ±100 kN by ASTM D790-03 standard, where each batch was composed of five specimens. To follow the curing process all mixture were measured by Dynamic DSC method under an N_2 atmosphere with heating rate of 10 ℃/min. in a temperature range of 25 ℃ to 300 ℃ to cover the entire curing process. Next, the sample was cooled down to room temperature, then again, it was heated to 150 ℃ to obtain the T_g of the polymer/nanocomposite. To find the complex viscosity profile of nanocomposites, dynamic rheometric measurements of oscillatory shear strain were performed by MCR 302 rheometer under static air at 0.01 % γ_A, 1Hz frequency, and 0 N normal force by ASTM D1525 standard. The first interval of the test was to raise the temperature of a specimen from 20 ℃ to 80 ℃ at 2.5 ℃/min. heating rate, after the cell temperature reaches 80 ℃, it is kept in this condition for extra 20 minutes. The elastic and viscoelastic properties of the specimens are studied by the DMA using Melter Toledo (DMA)/SDTA861 instrument. Electrochemical measurements of H0, H1, H2, H3, H5, H10, ICL, and ICH were carried out by a Princeton Applied Research (PAR) Parstat 2263 potentiostat (Oak Ridge, USA). EIS measurements were scanned in the frequency range of 10 mHz to 1 MHz applying AC signal amplitude of 10mV by Power Sine. Specimens were prepared to exact same shape with dimensions of (20 mm x 10 mm x 3 mm), sandwiched

between two copper plates and put in Faraday cage throughout the whole measurement (Figure 3.2).

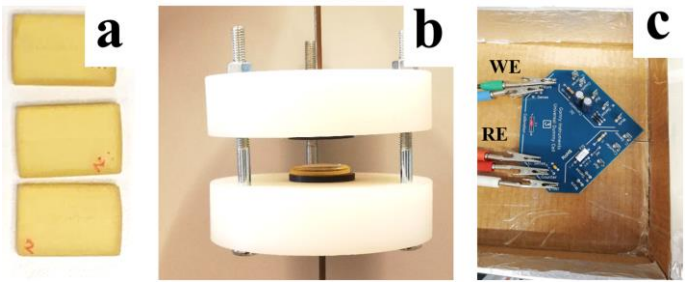

Figure 3.2 a) Nanocomposite sample cut to exact dimension, b) specimen sandwiched in the measurement cell, and c) working electrode (WE), and reference electrode (RE) connected to the calibration cell within Faraday cage.

3.3. Results and Discussion

3.3.1. Exploring various manufacturing techniques on epoxy/HNT

3.3.1.1. Effect of sonication method on the properties of epoxy/HNT nanocomposties

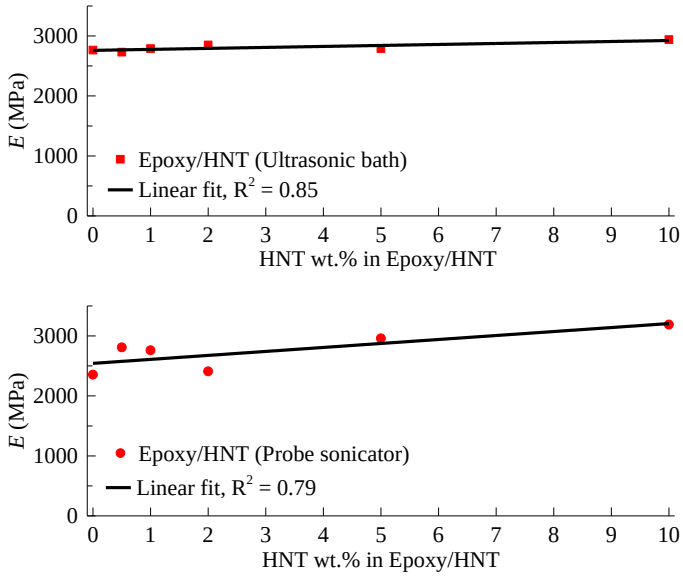

Figure 3.3 flexural muduls for three-point bending tests for H0, H0.5, H1, H2, H5, and H10 nanocomposites that are prepared either by (a) ultrasonic bath, and (b) by probe sonicator with the linear fit and R^2 value.

Figure 3.3 presents flexural muduls for three-point bending tests for H0, H0.5, H1, H2, H5, and H10 nanocomposites that are prepared by ultrasonic bath and by probe sonicator with

the linear fit and R^2 value. R^2 is higher for the specimens that are prepared by sonication bath however, according to Table 3.2, the improvement in $\bar{E}$ when using probe-sonication for all HNTs concentrations. The improvements in $\bar{E}$ for H1, H2, H5, and H10 are calculated based on $\bar{E}$ of H0 from the same batch of epoxy/HNT specimens.

Table 3.2 Improvements in $\bar{E}$ for H0, H1, H2, H5, and H10 prepared by ultrasonic bath vs. probe sonicator.

Sample ID	**$\bar{E}$ (MPa) Imp. (%)**	
	Ultrasonic bath	**Probe sonicator**
H0	0.00	0.00
H0.5	1.27	19.32
H1	0.90	17.20
H2	3.07	14.65
H5	0.90	25.69
H10	6.33	35.46

This mixing method causes more noticeable differences between the nanocomposites with different HNTs weight ratios. The probe sonication has dispersed HNTs more efficiently than the ultrasonic bath, especially at high concentrations of HNTs in the resin. The high difference in pressure that is generated locally by the probe vibration may break the agglomerated HNTs, allowing for more mixing and interaction with the polymer chains.

3.3.1.2. Effect of alkaline modification on the properties of epoxy/HNT nanocomposties

Figure 3.4 shows representative stress-strain curves of (a) epoxy/HNT and (b) epoxy/mHNT nanocomposites during three-point bending test. All specimens gave a stress-strain graph that is similar to the typical response of epoxy polymer in such a test. The first segment shows a linear behavior followed by a non-linear region until the maximum strength is reached, after which the graph shows a negative slope until the breaking point. The values in Table 3.2 shows the average modulus ($\bar{E}$) for five specimens for each concentration from epoxy/HNT and epoxy/mHNT specimens, alongside the standard deviation value. For epoxy/HNT specimens, $\bar{E}$ increase by the addition of HNTs for all weight ratio (wt. %) of HNTs, with H2 sample having the lowest improvements in $\bar{E}$ (compared to $\bar{E}$ of H0) among the rest of the samples manufactured by probe sonication method. The combined reason behind these phenomena is explained in details in our previous work [48], mainly that at 2 wt.% of HNTs, the stoichiometric ratio (i.e., the ratio between both stoichiometric

coefficients) of the hydroxyl groups (–OH) and amine groups ($–NH_2$) in the system. These groups are the main participants in the polymerization reaction of epoxy resin, and in the H2 system, the stoichiometric creates a curing kinetic conditions that produce a polymeric network with slightly longer segments of polymer chains, compared to their counterparts in the rest of the polymeric systems. This difference in the topology of the polymeric network leads to a slightly stronger plasticizing effect under stress but lower flexural strength at 2 wt.% in epoxy/HNT nanocomposites. For the second group of specimens in epoxy/mHNTs, similarly, $\bar{E}$ of epoxy samples increase after the incorporation of mHNTs, with the smallest improvement in $\bar{E}$ is achieved at 1 wt.% of mHNTs (i.e., in mH1 specimen) rather than at 2 wt.% as in H2. As the pristine HNTs undergo alkaline treatment, dispersion of HNTs improves, which exposes more -OH groups from the surfaces the nanotube. The uncured polymeric epoxy system needs only 1 wt.% of mHNTs to have a stoichiometric ratio which produces longer segmental chains, thus leading to more plasticizing during three-point bending test, and $\bar{E}$ is improved compared to $\bar{E}$ of mH0 but less than the improvement in mH2, mH5 and mH10. Table S3.2 contains more extensive comparison of mechanical properties for these two sets of nanocomposites.

Table 3.3 Values of average of flexural modulus ($\bar{E}$) for H0, H1, H2, H5, and H10 vs. mH0, mH1, mH2, mH5, and mH10 specimens.

	$\bar{E}$ **(MPa)**	
wt.%	**HNT**	**mHNT**
0	2740 ± 159	2798 ± 80
1	2900 ± 113	2832 ± 537
2	2830 ± 82	2983 ± 94
5	2950 ± 131	2977 ± 48
10	3030 ± 108	2960 ± 68

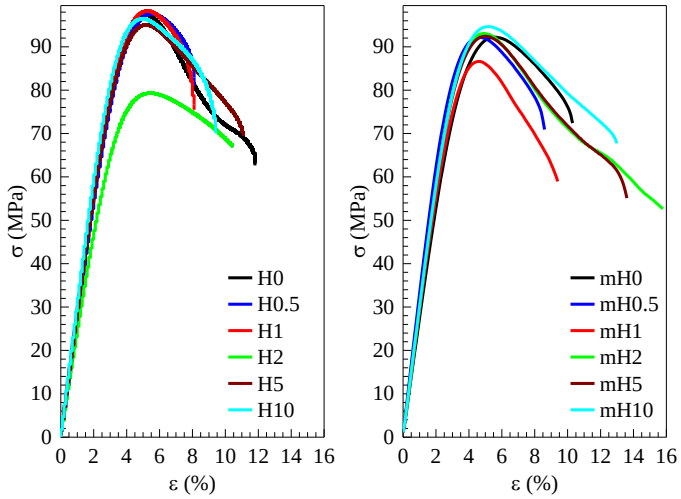

Figure 3.4 Stress-strain curves of (a) epoxy/HNT and (b) epoxy/mHNT nanocomposites during three-point bending test.

Table 3.3 shows that the improvement of $\bar{E}$ is moderate for mH1. Yet, modification of the HNTs by an alkaline solvent induces the risk of having some solvent remaining in the HNTs which might result in extra porosity. For that reason, mHNTs were not used in the EIS and conductivity experiments.

3.3.2. Exploring properties and performance of epoxy/HNT for structural capacitors properties

In the following section, the data is expressed exclusively for H0, ICL, ICH. All the results related to H1, H2, H5, and H10 can be found detailed in Chapter II.

3.3.2.1. DSC

Figure 3.5 shows the DSC graphs for H0, ICL, and ICH samples. The exothermic peak indicates the polymerization reaction for epoxy polymeric system and the formation of three-dimensional cross-linking network.

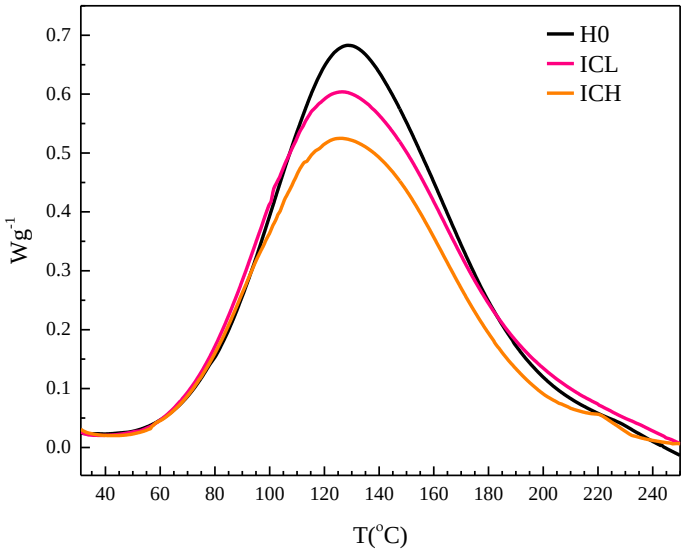

Figure 3.5 DSC graphs of H0, ICL, and ICH systems.

Table 3.4 lists T_{onset}, T_{endset}, ΔT, (T_p), and T_g for H0, ICL, and ICH. The epoxy ring-opening reaction can be monitored by $\Delta H_{tot.}$. For H0 $\Delta H_{tot.}$ = 314 J/g and it decreases by 17% in ICH to 259 J/g and decreases by 27% to 228 J/g in ICL system. The addition of IL/$LiClO_4$ to the uncured epoxy resin at room temperature jump start the polymerization reaction, thus the number of the reaction sites is smaller, which translates into smaller $\Delta H_{tot.}$ value obtained from the DSC test. For this same reason, $\Delta H_{tot.}$ for ICH is smaller than H0, however, adding HNT to the system provides additional reaction sites, therefore $\Delta H_{tot.}$ is higher than it is for ICL system. In ICL and ICH, the additives hinder the bond formation at lower temperature and T_{onset} increase by ~30 °C. On the other hand, T_{endset} for ICL and ICH is smaller than it is for H0 by ~10 °C, which lower ΔT by ~40 °C. This means that the presence of IL/$LiClO_4$ and HNTs in the system, plays a catalysis role and facilitate the polymerization process. Additionally, these additives lower T_p where the reaction rate is maximum by 2-4 °C. Finally, T_g of H0 increased by 2.5 °C in ICL and 3.5 °C in ICH showing the slight increase in the crosslinking in the polymeric net-work due to the presence of additives in the epoxy polymeric system.

Table 3.4 ΔH_{tot}, T_{onset}, T_{endset}, ΔT, T_p, and T_g of H0, ICL, and ICH during dynamic DSC measurements at Heating rate of 10 °C/min.

	H0	**ICL**	**ICH**
$\Delta H_{tot.}$ (J/g)	314	228	259
T_{onset} (°C)	44	72	73
T_{endset} (°C)	210	201	200
ΔT (°C)	166	129	127
T_p (°C)	130	128	126
T_g (°C)	62.5	64	65

3.3.2.2. Rheology

Figure 3.6 shows the evolution of complex viscosity $|\mu^*|$ with time for H0, ICL, and ICH systems. $|\mu^*|$ is related to the fraction of sol-gel in the reaction medium. Since the uncured epoxy mixture in H0 is liquid at room temperature, $|\mu^*|$ has a very low value. It shows that there are no chains formed yet. With the progress of the reaction and the gradual increase in temperature, $|\mu^*|$ increases very slowly therefore the plot almost looks like a plateau. Around 35 minutes, the polymerization process accelerates rapidly, indicating a significant increase in the molecular weight of the polymer and the progression of the cross-linking process. $|\mu^*|$ for ICL and ICH systems at the beginning of the test are 10 time bigger than $|\mu^*|$ of H0, as expected, since IL/$LiClO_4$ liquid and epoxy monomer solution will start interacting together once they are mixed (prior to the activation of the polymerization process by heating). Thus, the uncured systems of ICL, and ICH have higher $|\mu^*|$ compared to H0 at the beginning of the test in the low temperature region. The exponential increase in $|\mu^*|$ for ICL and ICH happens consequently after around 32 minutes.

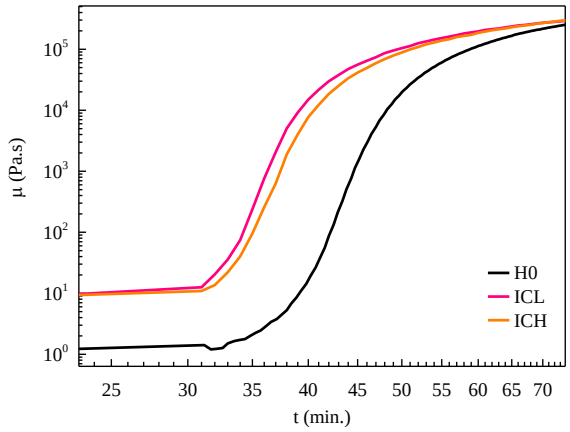

Figure 3.6 Graphs of complex viscosity $|\mu^*|$ vs. time for H0, ICL, and ICH systems.

3.3.2.3. DMA

Figure 3.7 represents the dynamic–mechanical properties like storage modulus (G′), loss modulus (G″), and tan δ for H0, ICL, and ICH. G′ increases with the addition of IL/$LiClO_4$ as the IL is incorporated in the epoxy cross-linked polymeric network. The additional bond with IL raises the polymer's resistance to deformation under stress. G′ of ICH is also higher than G′ of H0 but slightly lower than G′ o ICL. There are bonds formed between the epoxy and HNTs which raise G′ but not as much as IL/$LiClO_4$ system does. Because HNTs are a rigid clay-nanomaterial, they introduce second phase to the system and make it less homogeneous compared to ICL. On the other hand, by inspecting G″ curves, it is found that ICL sample has the highest G″. ICL has a higher cross-linking and can dissipate more energy during the DMA test. The peak of tan δ $(\tan \delta)_p$ correlates to the T_g of the system.T_g for H0 is 68 ℃ and it increases slightly to 73 ℃ and to 74 ℃ for ICL, and ICH, respectively. The maximum of $(\tan \delta)_p$ indicates the damping effect of the system, and it did not change for ICL compared to H0, however, it decreased in ICH. This means that the presence of HNTs improved the overall thermomechanical properties by improving G′ and lowering the damping effect of the system with a small increase in the T_g.

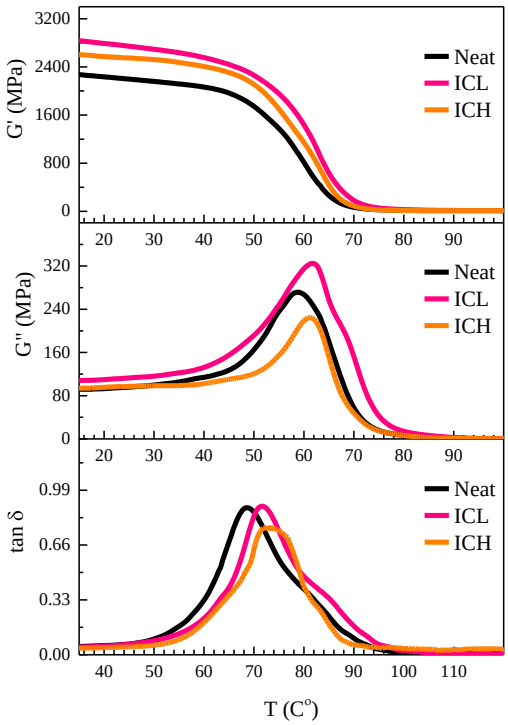

Figure 3.7 (a) Storage modulus (G′), (b) loss modulus (G″), (c) tan δ graphs for H0, ICL, and ICH.

3.3.3. EIS

Nyquist diagram of H0, H1, H2, H5, H10, ICL, and ICH that are obtained from the experimental data were corrected by dividing Z' and Z'' of each sample by its volume, and the corrected Nyquist plots are presented in Figure 3.8. All samples gave the typical semicircles shape, where the graph with x-axis at the high frequency region at $Z' = R_0$, and secondly in the lower frequency region at the end of the test. The phase angle and thus the impedance at $Z' = R_0 = 0$.

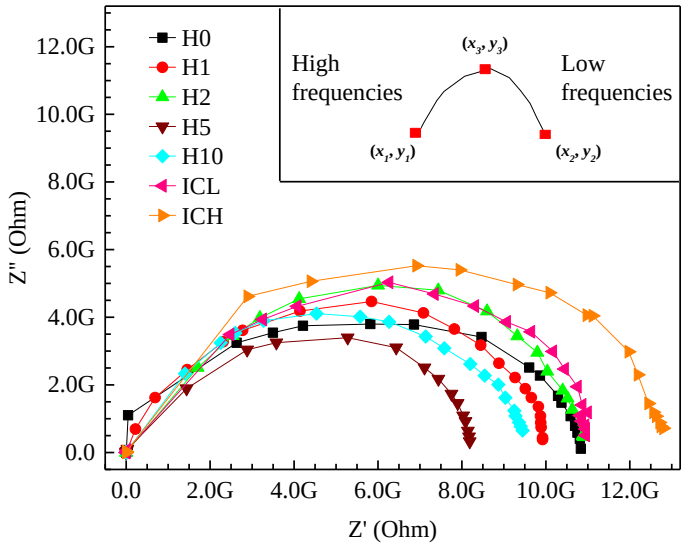

Figure 3.8 Nyquist plots the for H0, H1, H2, H5, H10 measured in frequency range of 1 MHz and 1 mHz, inset: scheme of the semicircle curve.

For each of the semi-circles there are two diameters, $r_1 = x_2 - x_1$, and $r_2 = y_3 - y_1$. A smaller r_1 is correlated with better conductivity. In Nyquist plots, at higher frequency ranges there is no difference among the tested samples, but at the low frequency level, it can be seen that the arc increase in length. So, at first glance to the Nyquist graph, the general trend of decrease in r_1 and thus the increase in conductivity is: ICH < ICL < H2 < H0 < H1 < H10 < H5.

For better representation of conductivity in the high frequency range, conductivities for each specimen were calculated at each frequency point using Equation 3.1, and conductivity spectra are presented as Log (σ) vs. Log (f) for H0, H1, H2, H5, H10, ICL, and ICH in Figure 3.9.

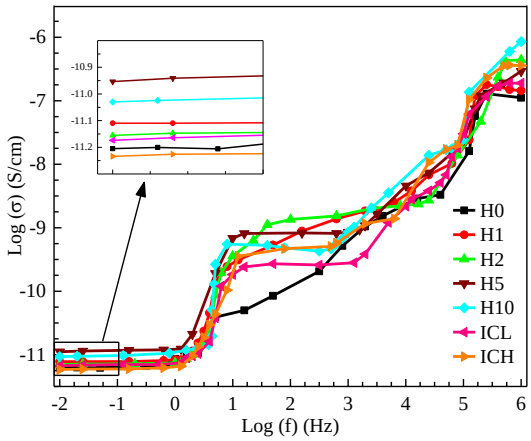

Figure 3.9 Conductivity spectra as Log (σ) vs. Log (f) for H0, H1, H2, H5, H10, ICL, and ICH nanocomposites.

At low frequencies, the conductivity is so small, that the average conductivity ($\bar{\sigma}$) = $10^{-11.1}$ S/cm at 10 mHz. $\bar{\sigma}$ increases to $10^{-6.5}$ S/cm at 1 MHz. At the higher frequency range (i.e., f $>10^4$ Hz) the conductivity corresponds to an electronic conducting component. At the beginning of the test, at f = 1 MHz, the conductivity increases from H0 to H10 as follows: H0 < H1 < ICL < H5 < ICH < H2 < H10. With decreasing frequencies, the conductivity deviates from electronic to ionic and the graph takes a more flat shape. The flattening is most clear in H5, H10, and ICL spectra. ICL does not contain HNTs and the ionic conductivity is caused mainly by IL and Lithium ions in the system. 5 wt.% and 10 wt.% of HNTs in the epoxy polymeric system provide better ionic conductivity.

Table 3.5 Log (σ) at 1 MHz, and at 10 mHz extracted from conductivity spectra in Figure 3.10 for H0, H1, H2, H5, H10, ICL, and ICH nanocomposites.

Sample	Log (σ) at 1 MHz	Log (σ) at 10 mHz
H0	-7.0	-11.25
H1	-6.9	-11.20
H2	-6.3	-11.25
H5	**-6.6**	**-10.90**
H10	**-6.0**	**-11.00**
ICL	-6.8	-11.10
ICH	-6.4	-11.30
Avg.	**-6.5**	**-11.1**

This indicates that the HNTs nanotubes provide some level of ionic conductivity without the presence of IL/Li^+ in the system. At lower frequencies the trend in the conductivity changes compared to higher conductivities. The conductivity is ascending as ICH < H0 < ICL < H2 < H1 < H10 < H5. According to Table 3.4, H10 has the highest

conductivity at 1MHz and the second highest conductivity at 10 mHz, therefore which makes it the sample with the best conductivity in a wide frequency range.

3.4. Conclusions

The manufacturing process of a wide range of concentration of epoxy/HNT nanocomposites was explored, to check the effect of mixing technique, and HNT type on the mechanical properties of the polymeric nanocomposite under flexural load. Probe-sonication is recommended for better distribution of HNT and other additives within the epoxy mixture. The alkaline modification of HNTs surface did not give a noticeable difference in the mechanical properties thus it can be excluded to make the synthesis process simpler. To introduce ionic additional ionic conductivity to epoxy/HNT nanocomposites, ionic liquid and Lithium perchlorate were used as additives, and the EIS spectra were obtained for all specimens. Conductivity spectra showed that high ratios of HNTs increase the ionic conductivity of epoxy similarly to the effect of 1 wt.% of IL/$LiClO_4$ does. When combining HNT and IL/$LiClO_4$ as additives to the system, a more complex change of the ionic conductivity is noticed. HNTs are efficient toughening materials that lower the overall cost of the resin, giving a greener composite. they creates channels within the epoxy polymers that provides paths for the ion movements which improves the ionic conductive of epoxy polymeric materials.

CHAPTER 4. DAMAGE MECHANISMS IN CFRP/HNT LAMINATES UNDER FLEXURAL AND IN-PLANE SHEAR LOADINGS USING EXPERIMENTAL AND NUMERICAL METHODS

This study is conducted to thoroughly scrutinize the role of nanotubes on the physics behind the deformation mechanisms and damage development in fiber reinforced polymer composites by using acoustic emission, digital image correlation, infrared thermography, fractography, and non-local meshless-numerical analysis, namely, Peridynamics. Carbon fiber laminates with and without HNTs are prepared and tested under flexural and in-plane shear loads. In depth analysis of the cumulative counts for acoustic emission data shows that the addition of HNTs mainly promotes the failure mechanisms associated with matrix cracking. Digital image correlation and infrared thermography analysis clearly prove that nanotubes prevent the coalescence of microcracks by blocking crack propagation or diverting its path. Fractography analysis shows that HNTs addition improves the interfacial strength despite promoting microcracks in the matrix. The hindrance of crack growth, crack tip splitting, and prevention of crack coalescence by HNTs clusters, are supported successfully by performing Peridynamic analysis.

4.1. Introduction

CFRP composites have been extensively used for both structural and non-structural applications in many different industries due to their high specific strength and improved fatigue life [49]. However, due to their layered structure, they possess relatively inferior through-thickness strength and low fracture toughness which readily leads to interlaminar failures such as delamination and debonding between the constituents [50]. One of the widely explored approaches for improving the interlaminar and also the intralaminar properties of the composite materials is to modify the matrix and/or the interface between the matrix and the fibers through the incorporation of nanomaterials [51-53]. The integration of nanomaterials helps to increase the interfacial affinity between carbon fibers and epoxy resin [54]. In literature, one can find a profound amount of effort on the incorporation of carbon based nanomaterials (i.e., carbon nanotubes, or graphene) into composite materials to improve their mechanical, thermal, thermomechanical and electrical properties, among

others [55]. On the other hand, there exist a lesser amount of research on the integration of other types of nanoparticles such as nano clay and silicon oxide into fiber reinforced polymeric (FRP) composites [31, 32, 56]. Bozkurt et al. [57] studied the nano clay incorporation into the glass fiber reinforced polymeric composite in order to form an adhesive layer on the fiber surfaces to increase the interfacial interaction. Their results showed that a 13% increase in the flexural strength can be achieved at 6 wt.% load of nano clay. Additionally, Tessema et al. [58] used silicon oxide nano powder in between prepreg layers during the stacking process and enhanced the in-plane shear modulus and shear strength of the pristine composite by 15% and 16%, respectively. Another clay-derivative nanoparticle such as HNTs was investigated as an alternative nano reinforcement candidate for FRP composites owing to its high aspect ratio. It was reported that the geometry of halloysite and the absence of entanglement compared to carbon nanotubes augments the surface interaction between the fibers and the matrix, and in turn transfer the load from the matrix to the fibers more efficiently, thus improving the numerous structural and non-structural properties of FRP composites [59, 60]. Moreover, Ye et al. [33] used HNTs to reinforce woven carbon fiber epoxy composites and ameliorated the flexural modulus by 5%. Besides, Han et al. [20] reported that they enhanced flexural modulus by 11% at the expense of a loss in ductility upon adding HNTs into composites. In literature, existing studies associated with HNTs reinforced composite materials have been mainly dedicated to improving certain mechanical properties of FRP composites, namely, fracture toughness [61-64], tensile [65], and interlaminar shear behavior [31, 33]. Nevertheless, there is no detailed study with combined experimental and numerical approaches to understand the physics behind how HNTs integration into composite materials improves mechanical properties.

To investigate the behavior of HNTs integrated FRP laminates or general composite materials, several structural health monitoring systems such as acoustic emission (AE), digital image correlation (DIC), and thermal imaging system (IRT) can be used. AE relies on the detection of elastic waves (i.e., bursts of energy) which are generated upon micro failure events and their propagation inside solid materials. AE technology employs ultrasonic transducers to collect real-time information on damage progression inside structures. Several studies utilized AE to characterize the failure behavior of composite materials under flexural and in-plane shear tests. For example, Tabrizi et al. [66] have recently investigated damage

accumulation in carbon/glass fiber hybrid polymer reinforced composite subjected to tensile and flexural load by using AE measurements. They successfully predicted the onset of major damages and classified the micro damage types. In an investigation by Cho et al. it has been found that the thermal conductivity of composite materials can be altered through the integration of nano materials [67]. Variation in thermal properties means that the IRT method which scans and detects the infrared radiation on the surface of materials can be used to identify damage initiation and propagations as well. Therefore, coupled AE- and IRT analysis can be helpful to monitor damage evolution within laminated composite structures. For instance, Yilmaz et al. [68] conducted in-plane shear tests via Iosipescu fixture on glass fiber reinforced composites without nano-integration and used AE with IRT to compare the effect of two types of glass fibers on micro-damage initiation under in-plane shear stresses.

Besides, it is almost inevitable not to have variations in the nanotube's distribution throughout the nanomaterial integrated laminated structure. As a result, any local or global inhomogeneity in nanotube distribution might lead to strain gradients inside the material [69]. Monitoring the full field strain map of the nanomaterial modified composites can be a logical approach to analyze the global effect of nanomaterials on a laminated structure. In fact, such a full field measurement would be more reliable as compared to monitoring local measurement systems such as strain gauge (SG). The DIC is a highly efficient full field monitoring technique, is used to characterize the strain evolution on various types of materials [70]. Principally, the DIC technique is based on the comparison of two images taken before and after deformation from the surface of the material which has a random speckle pattern applied on it [71]. The surface of the material should have a non-repetitive, high contrast pattern so that the displacement of a subset (i.e., one point and a set of points around it) can be readily tracked [72]. The subset displacement can be used to exactly determine the displacement of the material at one point on the surface. Cumulative examination of many subsets provides a full field displacement map of the surface which is readily transformed to strain values. Based on these strain maps, DIC can provide useful data such as the elastic modulus, poisons ratio, etc. [73].

Apart from the experimental investigations on composites materials for failure prediction, various theoretical approaches are also available based on classical continuum mechanics [74]. However, in general, these techniques suffer from the presence of structural

discontinuities such as crack occurrences/propagations when modelling the failure/damage in the composite material. A mesh-free non-local formulation of classical continuum mechanics, referred to as Peridynamics (PD) [75], circumvents these difficulties and in turn has become a powerful tool in solving complex engineering problems, especially the ones involving fracture mechanics, namely, modeling fracture behavior of various materials including isotropic [76] or orthotropic [77] materials, structural topology optimization [78, 79], and enhancement of fracture toughness [80], among others.

In this study, we have aimed to shed light on the failure behavior of HNTs integrated FRP laminate under flexural and in-plane shear loading conditions through experimental and numerical approaches, namely, AE, DIC, IRT, fractography, and PD. Given that each of these experimental methods provides a distinctive set of information from one another, e.g., being volumetric or surface related, the combined usage of them enables one to in-depth understanding of failure mechanisms in CFRP/HNT composites, which are not reliably and convincingly explainable by a single method. To our best knowledge, for the first time in literature, the effect of HNTs on the interface and the matrix failure mechanisms under shear forces are studied by utilizing a hybrid system of structural health monitoring techniques. Besides, we have theoretically investigated the effect of the nanomaterials on the shear response of composite materials through a novel computational model analyzed using the PD approach. Experimentally observed physical behavior during failure development by using the findings of AE, DIC, and IRT analyses is successfully cross-validated and explained by the computational PD model.

This study is structured as follows. In the methodology section which covers experimental and numerical approaches, firstly, the manufacturing process of CFRP and CFRP/HNT composites by RTM is described. Then, the mechanical tests i.e., flexural test coupled with AE, and in-plane shear test monitored with DIC, AE, and IRT are given in detail. To support the reasoning of the experimental results, PD analysis is conducted wherein the HNTs clusters are modeled as arbitrarily distributed multiple circular defects in the matrix system. The parameters used in the experimental procedures and in the numerical analysis are also provided in full detail. In the results section, the mechanisms involved in improvements of mechanical properties of CFRP composites due to the addition of HNTs are discussed thoroughly. Moreover, the results are supported by fractography analysis on the surface of

fractured flexural specimens. Finally, the numerical results of PD analysis are discussed and correlated to the finding of the experimental part, and the concluding marks are briefly provided.

4.2. Experimental

4.2.1. Materials

The following materials were used to prepare CFRP and CFRP/HNT composites: HNTs (ESAN, Turkey), LY 1564 SP resin, and XB 3403 Hardener (HUNTSMAN), and TORAY T300 3K plain-weave (2D) carbon fibers with 5 picks/cm and an aerial weight of 200 gsm ±3% purchased from Kordsa. In order to prepare the surface of RTM mold, three solvents are used: the XTEND-CX500 mold cleaner, XTEND-AMS semi-permanent mold sealer, and XTEND-838 as semi-permanent mold release (AXEL company).

4.2.2. Preparation of CFRP/HNT composites

The hardener was mixed with HNTs by a probe sonication for 40 minutes to have homogenously distributed nanoparticles and afterward, the hardener/HNT mixture was added into the epoxy resin. The overall mixture was stirred manually for five minutes, degassed for 20 minutes, and maintained under vacuum until the injection step. The mass amount of resin, hardener and HNTs in the final mixture was 67, 23, and 10 wt.%, respectively. Before manufacturing, the mold surface of the RTM system is processed with cleaning, sealing, and releasing agents in the given order to ensure that the manufactured part can be easily demolded. Twelve layers of precut woven carbon fibers (814 mm × 614 mm) were stacked in the mold cavity, and then vacuum was applied to the closed mold before the start of the resin injection. The prepared mixture which contained HNTs was infused into the mold cavity while monitoring impregnation of the dry fibers through glass top-lid of the RTM system. The injection process was terminated once the complete and bubble free impregnation was ensured. The impregnated fabrics were cured for 18 hours at 80 °C. Following the same procedure described, one pristine CFRP plate was also manufactured as a reference sample. Manufactured composite plates with and without HNTs were post cured at 80 °C in the oven for twelve hours and then cut into the geometry of the relevant test specimens for mechanical characterization.

4.2.3. Characterization

To obtain the weight fraction of different constituents of composite, TGA test was performed. Ten samples were collected from various locations of CFRP and CFRP/HNT plates. The samples were ramped from ambient temperature to 1000 °C by a rate of 20 °C/min. under N_2 gas in order to burn out the organic phase (i.e., the polymer matrix). Afterward, the temperature was maintained at 1000 °C and dry air was purged into the test chamber for 10 minutes, therefore, burning out the carbon fibers.

Mechanical tests were conducted using Instron 5982 equipped with a static load cell of ±100 kN. To find the flexural modulus of composite material, flexural tests were performed in accordance with the ASTM D790-03, with a constant speed of 2 mm/min., and a span-to-depth ratio of 16:1. The dimensions for flexural test samples of the CFRP laminate are 76 mm × 12.7 mm × 4 mm, while the dimensions of CFRP/HNT specimens are 76 mm × 12.7 mm × 3.5 mm. AE technique was also used to monitor the damage evolution during the test. Two wideband AE sensors were adhered by hot melt glue on the top surface of each specimen, with a 24 mm distance from the edges of the specimens (Figure 4.1a). MISTRAS Micro II Digital AE system was used to collect the data from the AE sensors with the sampling rate of 2 MHz. The sensor output was amplified by 20 dB using a preamplifier in single mode, and the sensitivity threshold level was set as 40 dB. The filtering of collected signals was performed between 20 kHz-1000 kHz using the Bessel band-pass filter. The calibration of the system was done using the pencil lead-breaking method, and the data were processed by Noesis 7 Software. K-means algorithm was used for clustering the data. Bray-Curtis dissimilarity function was employed as the distance function for clustering, and the chosen number of clusters was evaluated with Silhouette criteria [81].

In order to find the shear modulus, in-plane shear test was performed according to ASTM D5379 using Iosipescu shear test fixture, with a constant load speed of 2 mm/min. (Figure 4.1b). Biaxial rosette strain gauges from Micro-Measurements were used with an exposed solder tap area of 1.0 mm x 1.8 mm, a grid resistance of 350 ± 0.6% ohms, and a gauge factor of 4.728. In order to monitor the behavior of composite specimens under in-plane shear loading, three techniques were utilized simultaneously, AE, DIC, and IRT. The same set-up of AE as mentioned above was employed with only one piezoelectric sensor attached at the back of the specimen. To get the full field strain map of the gauge length, the DIC system

manufactured by GOM Company was used with 12M sensors. The calibration of DIC instrument was carried out in snapshot mode using coded calibration object provided by the manufacturer with a size of 55 × 45 mm^2. The results of calibration indicated a calibration deviation of 0.028 pixels and a scale deviation of 0 mm which are both under the limitations defined by the manufacturing company. The frame rate of image acquisition during the test was set to 5 Hz, and the post processing of the recorded images was done using subsets with the size of 25 × 25 pixels and a step size of 15 × 15 pixels at ARAMIS professional software.

Moreover, IRT is used to monitor thermal activity due to deformation under in-plane shear stress. FLIR X6580sc camera was used with temperature ranges from 20 °C to 3000 °C, 50 mm lens, an Indium antimonite photon detector, and reading accuracy of 1%. Thermal data was collected with a sampling rate of 10 Hz, and then processed with FLIR ResearchIR Max software. In order to position all the tests apparatuses properly with respect to the inspected specimens, both of DIC system sensors, and thermal camera were placed in front of the Iosipescu specimens at 450 mm, 500 mm, respectively. The strain gauge was fixed at the back of the specimen in order to prevent its induced temperature from interfering with the thermal camera, and the AE sensor was glued next to it as seen in the inset image of (Figure 4.1b).

The fracture surface of failed CFRP and CFRP/HNT specimens under flexural load was analyzed by using a Leo Supra35VP Field Emission SEM. The SEM images were produced using an electron power of 2 kV, with a 5.8 mm working distance. Prior to microscopic analysis, the examined surfaces of SEM samples were sputter coated with a thin layer of gold to allow for electric conductivity.

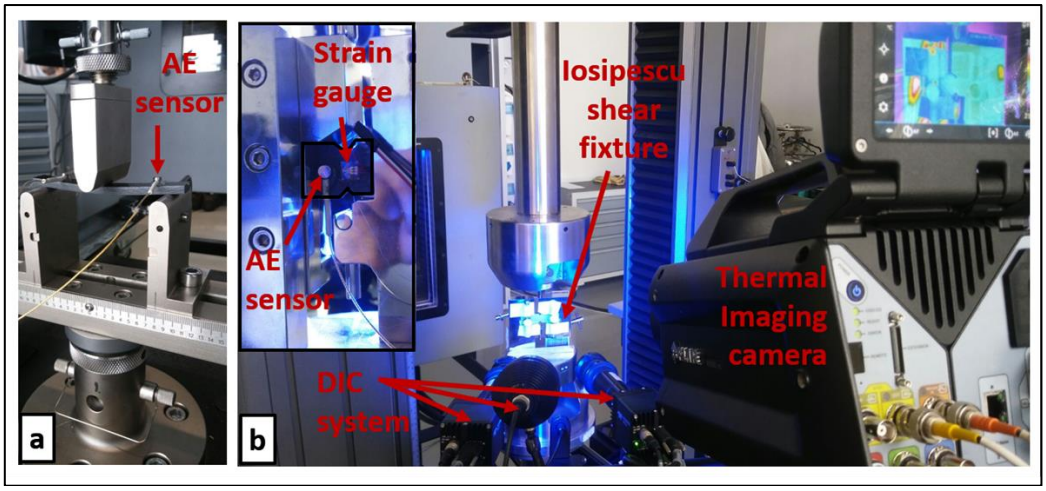

Figure 4.1 (a) Flexural test with AE sensors, (b) In-plane shear test with DIC system, and thermal camera at the front side of the specimen, and (Inset) (SG, and AE sensor) at the back side of the specimen.

4.3. Numerical Modeling (Ordinary-state-based peridynamic formulations)

For numerical modeling purpose, we have used an ordinary-state-based PD formulation, where the continuum is represented as the ensemble of infinitesimally small volumes (represented as material points or particles) interacting with each other in a non-local manner. According to PD theory, an arbitrary material point interacts with its neighbors within a finite distance referred to as horizon, δ, and these interactions are called the PD bonds. The horizon size is generally taken as $\delta = 3dx$ where dx represents the particle spacing (Figure 4.2).

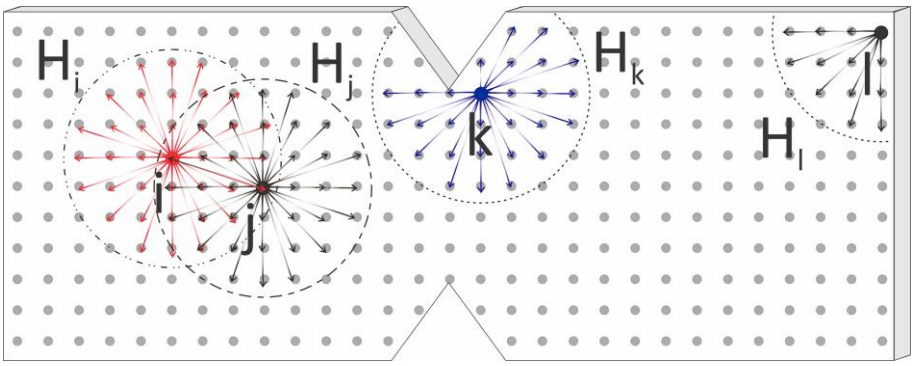

Figure 4.2 PD continuum in two dimensions.

In PD theory, unlike classical continuum mechanics, the divergence of stress in the equation of motion is replaced by integrals of PD bond force densities that are defined in terms of displacements and associated bond constants. To model the intra-family interactions

in the continuum, let us consider that the continuum undergoes a deformation causing displacements of $\mathbf{U}_i$ and $\mathbf{U}_j$ for the material points *i* and *j*, respectively, as shown in Figure 4. 3. Let the deformed positions of material points be $\mathbf{Y}_i$ and $\mathbf{Y}_j$, and their relative initial and final positions be $\boldsymbol{\xi}_{ij} = \mathbf{X}_j - \mathbf{X}_i$ and $\boldsymbol{\eta}_{ij} = \mathbf{Y}_j - \mathbf{Y}_i$, respectively. Hence, for any material point *i*, with an initial position of $\mathbf{X}_i$, the PD form of the equation (i.e., Equation 4.1) of motion can be written as:

$$\rho_i(\mathbf{X}_i)\ddot{\mathbf{U}}_i(\mathbf{X}_i,t) = \int_{H_i}\left[\mathbf{t}_{ij}(\mathbf{U}_j - \mathbf{U}_i, \boldsymbol{\xi}_{ij}) - \mathbf{t}_{ji}(\mathbf{U}_i - \mathbf{U}_j, \boldsymbol{\xi}_{ji})\right]dH_i + \mathbf{B}_i(\mathbf{X}_i,t) \tag{4.1}$$

where the parameter ρ_i is the density of the continuum at point *i*, and the vectors $\ddot{\mathbf{U}}_i$ and $\mathbf{B}_i$ are the acceleration and body force density acting on material point *i*, respectively.

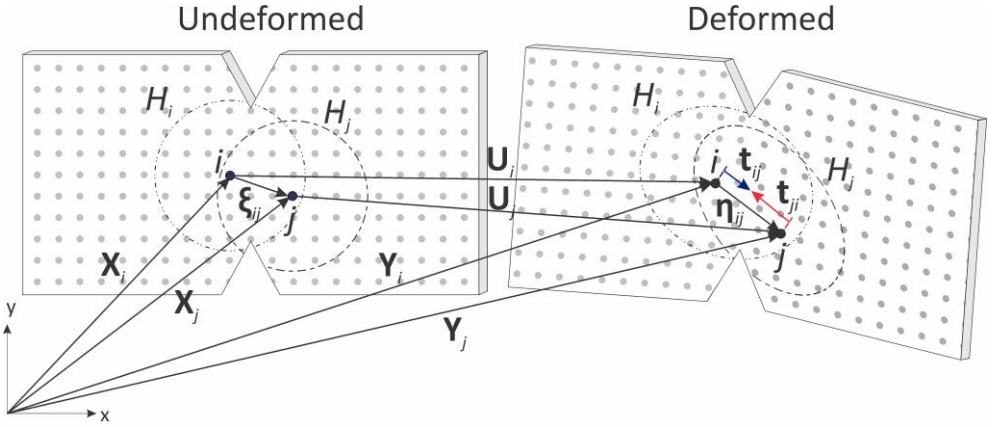

Figure 4. 3 Deformation state and force density vectors of PD continuum.

The discrete form of PD equation of motion can be written using the Gaussian quadrature method [82] by replacing the integral with the summation operator over the family of the point *i*. The terms $\mathbf{t}_{ij} \equiv \mathbf{t}_{ij}(\mathbf{U}_j - \mathbf{U}_i, \boldsymbol{\xi}_{ij}, t)$ and $\mathbf{t}_{ji} \equiv \mathbf{t}_{ji}(\mathbf{U}_i - \mathbf{U}_j, \boldsymbol{\xi}_{ji}, t)$ represent the pairwise force densities between material points *i* and *j* as shown in Figure 4. 3 Deformation state and force density vectors of PD continuum.. These force densities can be expressed as $\mathbf{t}_{ij} = 0.5C_i\boldsymbol{\eta}_{ij} / |\boldsymbol{\eta}_{ij}|$ and $\mathbf{t}_{ji} = -0.5C_j\boldsymbol{\eta}_{ij} / |\boldsymbol{\eta}_{ij}|$ where C_i and C_j constants are the auxiliary parameters established through interrelating force density vectors and the strain energy

density of the continuum [83]. These parameters can be explicitly written in Equations 4.2 and 4.3 as:

$$C_i = \left(\lambda_{ij}\right) 4 \frac{\delta}{\left|\boldsymbol{\xi}_{ij}\right|}\left[a d \theta_i \left(\frac{\boldsymbol{\eta}_{ij}}{\left|\boldsymbol{\eta}_{ij}\right|} \cdot \frac{\boldsymbol{\xi}_{ij}}{\left|\boldsymbol{\xi}_{ij}\right|} \right) + b S_{ij} \left|\boldsymbol{\xi}_{ij}\right| \right] \tag{4.2}$$

$$C_j = \left(\lambda_{ji}\right) 4 \frac{\delta}{\left|\boldsymbol{\xi}_{ji}\right|}\left[a d \theta_j \left(\frac{\boldsymbol{\eta}_{ji}}{\left|\boldsymbol{\eta}_{ji}\right|} \cdot \frac{\boldsymbol{\xi}_{ji}}{\left|\boldsymbol{\xi}_{ji}\right|} \right) + b S_{ji} \left|\boldsymbol{\xi}_{ji}\right| \right] \tag{4.3}$$

where $S_{ij} = \left(\left|\boldsymbol{\eta}_{ij}\right| - \left|\boldsymbol{\xi}_{ij}\right|\right) / \left|\boldsymbol{\xi}_{ij}\right|$ is the stretch of the bond between *i* and *j* material points. The terms θ_i and θ_j correspond to the PD dilatations of points *i* and *j*, respectively, and can be calculated by Equation 4.4 as:

$$\theta_i = d\delta \sum_{j=1}^{H_i} S_{ij} \left(\frac{\boldsymbol{\eta}_{ij}}{\left|\boldsymbol{\eta}_{ij}\right|} \cdot \frac{\boldsymbol{\xi}_{ij}}{\left|\boldsymbol{\xi}_{ij}\right|} \right) V_j \quad , \quad \theta_j = d\delta \sum_{i=1}^{H_j} S_{ji} \left(\frac{\boldsymbol{\eta}_{ji}}{\left|\boldsymbol{\eta}_{ji}\right|} \cdot \frac{\boldsymbol{\xi}_{ji}}{\left|\boldsymbol{\xi}_{ji}\right|} \right) V_i \tag{4.4}$$

with V_i and V_j denoting the volume of the particles, *i* and *j*. In Equations (4.2 – 4.4) the a, b, and d parameters are the PD bond constants dependent on material properties and horizon size. These parameters are defined by equating strain energies of PD theory and classical continuum mechanics and are given in [76]. The variable λ_{ij} is an irreversible control parameter for the breakage of the related bond. Thus, it is $\lambda_{ij} = 1$ if $S_{ij} < S_0$ (critical stretch) and $\lambda_{ij} = 0$ otherwise. Herein, the critical stretch is a function of material properties such as the critical energy release rate, G_c, and the horizon size [76]. One can think of the bond between two material points as an elastic spring where any change in the length of the bond causes a micro potential. The overall strain/potential energy of a point is then calculated by integrating these micro potentials over the family of the point. Accordingly, a critical strain energy is obtained when the stretch of the related bond reaches a critical/threshold value at which any small increase in energy results in the breakage of the bond and crack propagation. Hence, the amount of failure of the bonds is directly proportional to the amount of energy consumed.

Since the mathematical formulation of PD is written in the integral form, it is straightforward to introduce any discontinuity, i.e., crack, with static/dynamic interfaces. However, to calculate the amount of the local damage of a particle, an extra damage parameter should be introduced as $\varphi_i = 1 - \sum_{j=1}^{H_i} \lambda_{ij} V_j / \sum_{j=1}^{H_i} V_j$ where $\varphi_i = 1$ if all the bonds of the material point *i* are broken and $\varphi_i = 0$ in case of no broken bond [84]. Furthermore, when performing the explicit time-integration of the PD equation of motion, a stable incremental time-step size should be determined to achieve the convergence [85].

4.4. Results and Discussion

4.4.1. Composition of CFRP and CFRP/HNT composites

Based on the results of TGA analysis, the weight fraction of CFRP and CFRP/HNT constituents are calculated. The weight fraction of carbon fibers (CFs) in both composite systems is 48 wt.% while the weight fraction of the epoxy resin decreased from 52 wt.% in CFRP to 48 wt.% in CFRP/HNT laminates, corresponding to HNTs content of 4 ±1 wt.% in the composite. Thus, approximately 6 wt.% of the infused HNTs has been infiltrated through the woven fabric. Such infiltration can be attributed to possible entrapments of some agglomerated HNTs clusters during infusion at certain locations of the manufactured laminate. On the other hand, infiltration might also be promoted due to possible variations in the pressure across the mold cavity. These technical factors are mainly responsible for the variation in HNTs wt.% in the CFRP/HNT composite plate; therefore, precaution must be taken when the size of HNTs clusters are used to interpret the damage mechanisms in the resin matrix.

4.4.2. Flexural performance in CFRP/HNT

Flexural property is one of the key parameters for evaluating mechanical performance and failure characteristics of FRP composites. The flexural stress-strain curves obtained from flexural tests for CFRP and CFRP/HNT are shown in Figure 4.4. Moreover, in Table 4.1. are given the average values of flexural modulus and strength and strain at maximum load for three samples from each laminate. It is seen that the incorporation of HNTs into the composite structure has improved the flexural modulus from 41±0.5 GPa to 48±1 GPa. Furthermore, the flexural strength of CFRP and CFRP/HNT is measured to be 614±13 MPa

and 732±13 MPa, respectively, which indicates notable enhancement thereof, and strain at the maximum load is also slightly increased from 1.63±0.01% to 1.69±0.01% by addition of HNTs.

Table 4.1. Average of flexural modulus ($\bar{E}$), strain at maximum load ($\bar{\varepsilon}$), and flexural strength ($\bar{\sigma}$) of CFRP and CFRP/HNT specimens.

	$\bar{E}$ **(MPa)**	$\bar{\varepsilon}$ **(%)**	$\bar{\sigma}$ **(MPa)**
CFRP	41450 ± 1399	1.63 ± 0.01	614.7 ± 12.9
CFRP/HNT	48950 ± 0107	1.69 ± 0.01	732.0 ± 13.1
Improvements	18.10%	03.63%	19.10%

All the tested specimens gave similar responses as seen in Figure 4.4. At the end of the test, both composites present stress drops before the final fracture. Comparing this region between two sets of composite types (Figure 4.4; inset) reveals that the stress drops attain over a broader strain interval for the neat specimens, with wider stress-drop steps. HNTs reinforced specimens have a smaller region with a series of small stress drops until the end of the test. This agrees with previous findings in the literature where it has been shown the improvement of flexural strength upon nanotubes integration in FRP composites results in a narrower level-off region in the stress-strain curve towards the final stages of failure [86]. In other words, the final stage of the global failure is shifted towards the higher strain values. This improvement can be attributed to crack growth and delamination which are continuously hindered by the presence of nano reinforcements. The out of plane deformation and bending of CFRPs result in complex damage mechanisms, among which multiple delamination and interfacial fractures are dominant ones. Herein, to identify the effect of HNTs on damage initiation and growth in composite structures subjected to bending loads, the following section presents AE data collected during the flexural test.

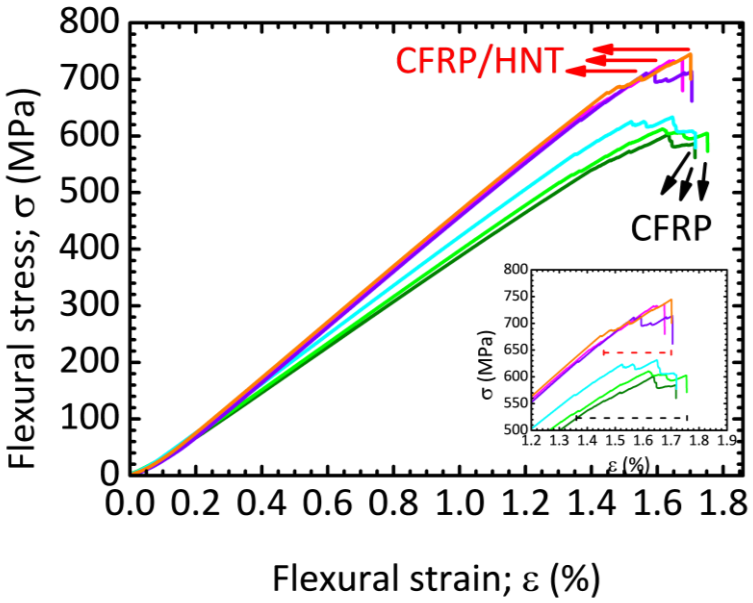

Figure 4.4 Stress-strain curves of CFRP and CFRP/HNT specimens under flexural test in 3-points bending configuration.

AE waves generated during the failure are collected using a couple of piezoelectric sensors. In this method, AE waves were clustered based on their weighted peak frequency (WPF), and partial power 2 (PP2) which are proven to be effective to identify different damage mechanisms such as matrix cracking, delamination, and fiber failure in CFRPs . Herein, WPF is the square root of the product of frequency centroid and peak frequency whereas the PP2 is calculated by dividing the power spectrum in the range of 300-600 kHz to the total power for each AE hit, which is then presented in percent values.

Figure 4.5a and 4.5b show AE clustered data for CFRP and CFRP/HNT, respectively. The results of K-means clustering shows three distinct clusters associated with three different failure mechanisms, which are classified with respect to their WPF ranges: 45-175 kHz, 175-270 kHz, and 360-570 kHz. In our previous study, these clusters were associated with three main failure mechanisms of: matrix cracking (cr), delamination (d), and fiber fracture (fr), respectively [87].

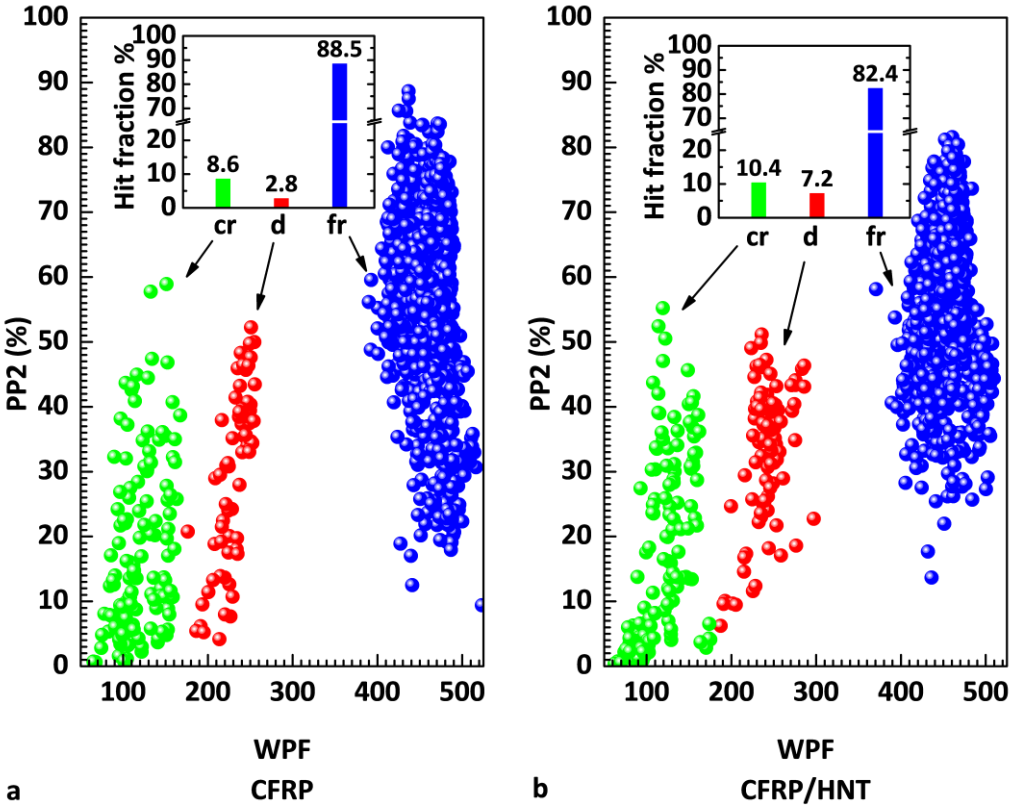

Figure 4.5 AE clusters of CFRP vs. CFRP/HNT specimens under flexural test. The inset figures provide hit fraction of matrix cracks; cluster-cr (green), delamination; cluster-d (red), and fiber fracture; cluster-fr (blue).

Table 4.2; summarizes the averaged AE data of the three neat and HNTs reinforced specimens, which are tested under flexural load. By the incorporation of HNTs into the composite, the average AE hit number dropped from 1459 to 1086. We observed that the standard deviation of the hit number associated with each type of failure is high in all the specimens. Therefore, it is more sensible to compare the average hit fraction. As can be seen from Figure 4.5, the highest average hit fraction is related to fiber breakage. The matrix cracking has increased from 8.6% to 10.4%, thus suggesting that HNTs may act as crack initiation points under higher stress levels and in turn, promote the formation of micro cracks in the material as can be observed from Figure 4.6. The average hit fraction associated with the delamination failure type increases from 2.8% to 7.2% after the addition of HNTs. These two observations imply that the nano integration made the composite material more susceptible to damage initiation. Nonetheless, at low stress levels, the strain field gradient at the interface of HNTs/matrix is not so severe; therefore, the nanomaterials reinforce and consequently increase the stiffness of CFRP as seen in stress-strain curves. However, at high

loading levels, the strain field gradient at the interface of HNT/matrix becomes significant resulting in high stress concentration. High stress regions around the HNTs gradually promote crack initiation in the matrix material, which is also evident from AE activities related to matrix cracking in CFRP/HNT composite system (see Figure 4.5). Nevertheless, as to be discussed in the coming sections, the HNTs will be effective through inhibiting the progress of matrix or interface related damages regardless of its origin, i.e., HNTs induced or inherently formed in the composite. To be able to confirm this conclusion, as shown in Figure 4.6, it is prudent to present the cumulative count versus time and stress-strain behavior on the same graph for representative CFRP and CFRP/HNT specimens since the cumulative graphs of the AE counts allow real-time tracking of both the activation and evolution of various damage mechanisms.

Table 4.2 Comparison of number of hits and hit fraction during flexural test of WPF for cr, d, and fr clusters of each of CFRP vs. CFRP/HNT.

	CFRP		**CFRP/HNT**	
	Avg. No. of hits	**Avg. Hit fraction %**	**Avg. No. of hits**	**Avg. Hit fraction %**
Cluster-cr	126 ± 16	8.6 ± 0.01	114 ± 44	10.4 ± 0.01
Cluster-d	42 ± 21	2.9 ± 0.01	75 ± 18	7.2 ± 0.01
Cluster-fr	1291 ± 153	88.5 ± 0.00	897 ± 348	82.4 ± 0.01
Total	1459 ± 146	100.0 ± 0.00	1086 ± 334	100.0 ± 0.00

Due to the application of concentrated load in the three-point bending test, typically, the initial damage type is fiber buckling on the compression side of the specimen, which is also well correlated with results of previous investigations by the authors [66]. As observed in Figure 4.6, the AE activities corresponding to fiber breakage start prior to other failure types in both composite systems. For the pristine representative specimen presented in Figure 4.6a; the slope of the cumulative counts versus time curve for fiber fracture increases gradually while for other damage types, i.e., matrix cracking and delamination, a sudden jump in AE counts is observed, which is marked by an oval in Figure 4.6a. The abrupt increase in the cumulative counts associated with matrix cracks and delamination bespeaks a failure of the matrix and the interface in a progressive manner. Afterward, the fibers breakage continuously occurs until the final failure, which suggests that the fibers are the only remaining constituent that holds the integrity of the system. CFRP/HNT specimen exhibits different responses to

flexural load. Namely, the matrix crack and delamination failures start at lower strain levels than that of the CFRP specimen. The AE activities related to matrix cracking and delamination reach their maximum values over a larger strain range unlike the case of the pristine specimen. Additionally, the cumulative curve of matrix cracks has a stepped behavior with wider intervals. These experimental observations enable us to back up our previous statement that the incorporation of HNTs into composite materials prevents crack propagation.

In both composite material types, the cumulative AE counts associated with matrix cracking and delamination starts leveling off after the occurrence of major deformation, which corresponds to the onset of the nonlinear response (stiffness degradation) in the stress-strain curve. However, matrix and interface related AE activities in the HNT-integrated composite specimen continue with small increments (seen as small steps in the cumulative count-time graphs) until final breakage point as shown in Figure 4.6b. The gradual matrix cracking and delamination events suggest that there are both ductile and brittle failures taking place in the CFRP/HNT system towards the end of the test, which is indicative of matrix tearing phenomenon [88] as will be shown in the following fractography section.

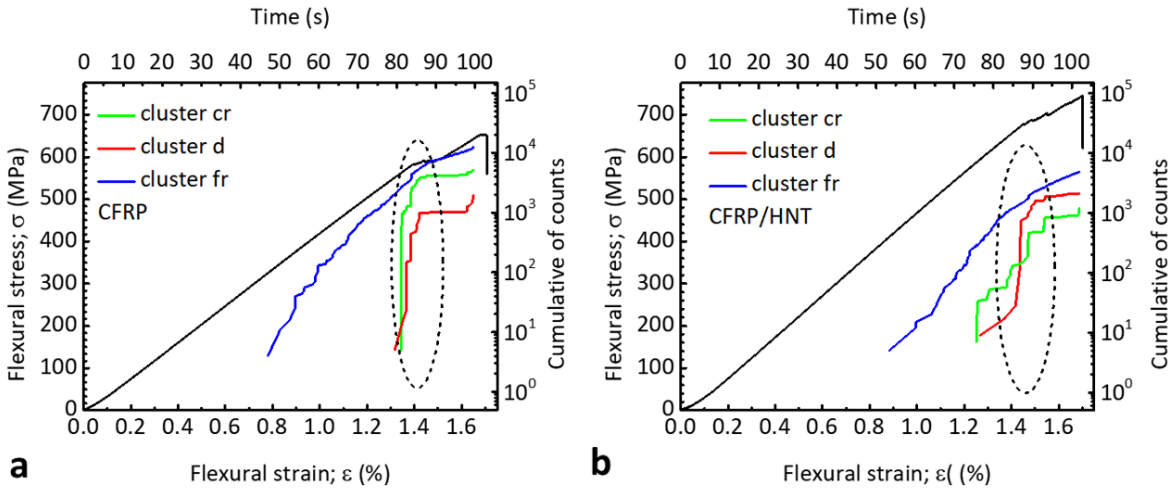

Figure 4.6 Flexural stress-strain curve merged with cumulative counts of AE during the test for (a) CFRP composite and (b) CFRP/HNT.

4.4.3. Fractography

Figure 4.7 and 4.8 compare the fracture surface of CFRP and CFRP/HNT after flexural test, which provides information such as, the interface morphology, defects, and the main

mechanisms of deformation in the composite material. Note that plain-woven CFs have two different directions within the fracture surface (i.e., the examined plane), namely, CFs parallel (0^{o} CFs) and normal (90^{o} CFs) to the examined plane. Under flexural loading conditions, the 0^{o} CFs undergo interface delamination along the fibers' direction while the 90^{o} CFs are more prone to fiber breakage and fiber pull-out. In Figure 4.7a, an interface failure in the pristine composite specimen is clearly noticeable around 90^{o} CFs, where a broken fiber bundle is partially covered by the remnant matrix. On the other hand, the interface of broken fibers in CFRP/HNT composite specimens is continuous and indistinguishable from the surrounding matrix as seen in Figure 4.7b. This is because the addition of HNTs into the CFRP composite enhances the interaction between the CFs and the matrix, i.e., stronger interface.

In Figure 4.7c fracture with a textured surface and multiple river lines extending along the fiber can be observed. These river lines spread from the fiber and converge with each other, i.e., the fracture planes overlap before they coalesce, producing randomly oriented cusps [46, 89-91]. In contrast, Figure 4.7d shows a rough surface without any discernible fracture planes, and there are several propagating microcracks at the interface of 0^{o}- and 90^{o}- CFs as indicated by a dashed line. The difference in the fracture morphology of CFRP and CFRP/HNT can be attributed to the interruption of effective cross-linking of the polymer chains owing to the presence of HNTs.

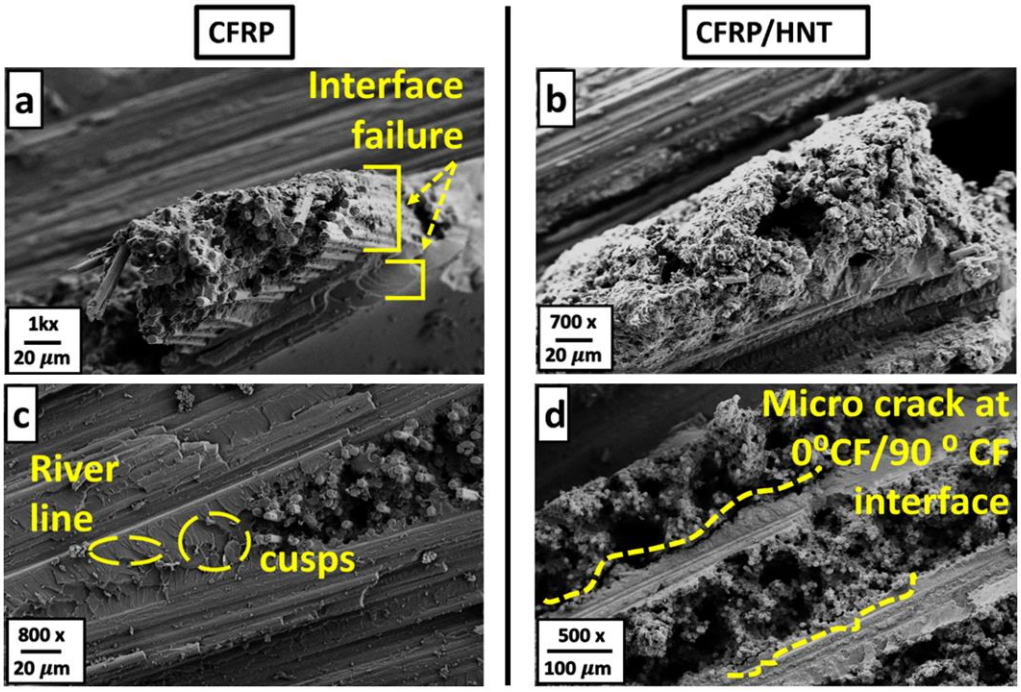

Figure 4.7 SEM micrographs for the cross section of failed (a, and c) CFRP vs. (b, and d) CFRP/HNT composites under flexural loading.

The comparison between Figure 4.8a and 4.8b shows that the matrix in the neat specimen is detached from the fibers through peeling process as indicated by an arrow in Figure 4.8a. Moreover, residues of broken fibrous are seen on the fracture surface, which is probably related to sudden energy release at the final stages of loading as indicated by an abrupt increase in the total AE activity in Figure 4.6. Due to the weaker interface between the fiber and matrix in the pristine specimen, the sudden energy release at the failure stage splits already detached fiber into small pieces. On the contrary, for HNTs integrated laminates, small fiber pieces are not visible since the fibers are still partially surrounded by matrix as seen in Figure 4.8.

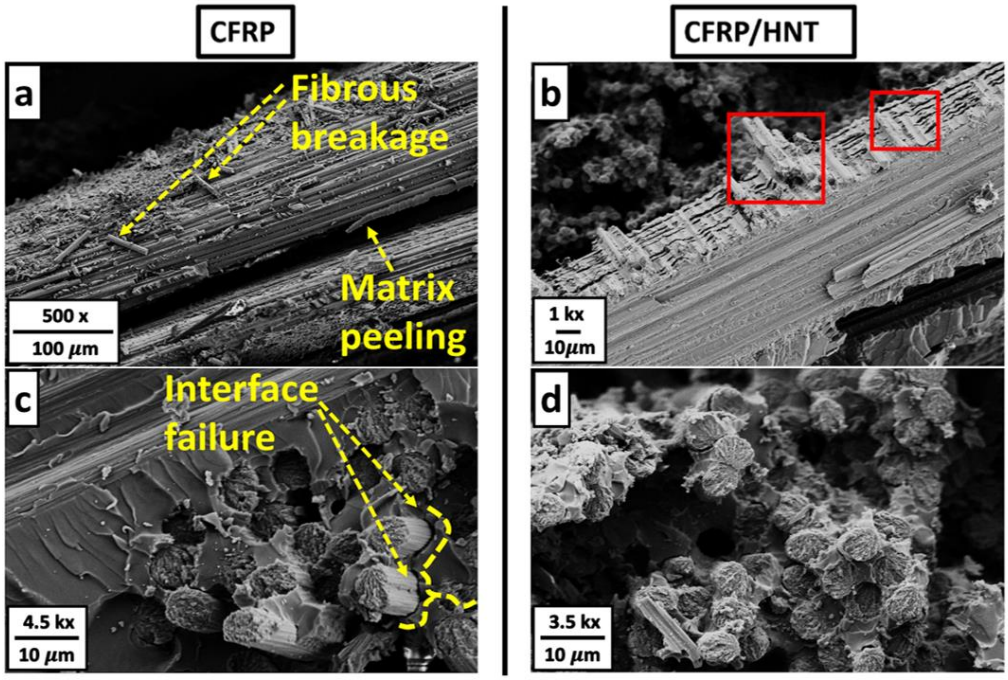

Figure 4.8 SEM micrographs for the cross section of failed (a, and c) CFRP vs. (b, and d) CFRP/HNT composites under flexural loading.

Figure 4.8c shows a broken fiber of the neat specimen, where clear gaps between the fibers and the matrix are recognized due to interface failure. The fiber crenulations are clearly visible indicating that debonding along the fiber/matrix interface is in the form of an adhesive failure [92]. In contrast, in Figure 4.8d, there are partial debonding around the fibers, where debris of the matrix is still attached to the fibers, i.e., no standalone fibers. Such morphology agrees with previous investigations, where HNTs integration into the composite system improved fiber/matrix interface thus leading to a cohesive failure development [93].

For the detailed analysis of fracture surface associated with HNTs integrated composite specimens, two marked regions of Figure 4.8b; are magnified as presented in Figure 4.9. The directions of 90^{o} and 0^{o} CFs are indicated with the dashed line in Figure 4.9. The remnant 90^{o} fibers seen in Figure 4.9a clearly indicate that there is a strong attachment between the matrix and fiber interface even after the failure. The marks for fiber imprints in Figure 4.9a and 4.9b imply the propagation of micro cracks along the 90^{o} fiber in the matrix due to the tensile stresses.

Figure 4.9b shows the coexistence of multiple ductile and brittle failures along and in the vicinity of 90^{o} CFs, which are seen as textured regions and smooth surfaces (shear cusps) [94], respectively. It is noted that the locations of ductile failures are closer to CFs. The

presence of mixed failure types can be related to the fact that HNTs enhance the strength of the fiber/matrix interface more than that of the bulk matrix. Hence, HNTs at the CFs and matrix interface are asserted to hinder crack growth. This conclusion is consistent with the small steps of damage accumulation presented in Figure 4.6b for CFRP/HNT composites. Stated otherwise, the integration of HNTs inside the composite material can prevent the coalescence of microcracks.

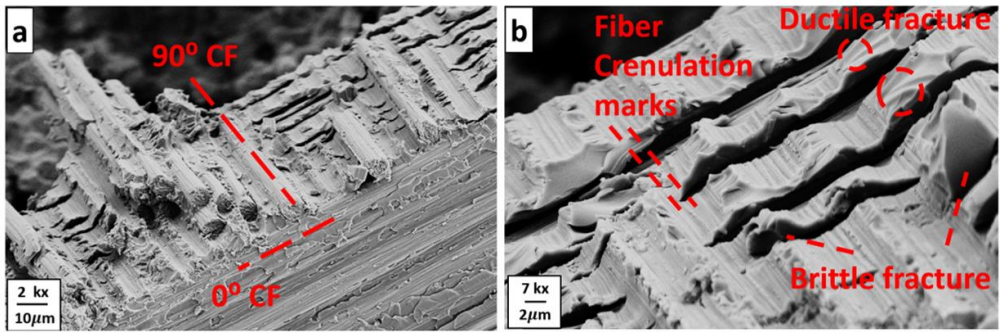

Figure 4.9 SEM micrographs of magnified regions that are marked in red rectangular in Figure 4.8b for a fractured CFRP/HNT specimen under flexural load.

4.4.4. Improvements in the In-plane shear properties

In-plane shear strength, strain, and modulus are calculated according to ASTM D 5379. Figure 4.10 exhibits in-plane shear stress-strain curves of both CFRP and CFRP/HNT specimens. There is an elastic region up to 1% strain, followed by non-linear stress-strain behavior up to 21% strain. The slope of CFRP and CFRP/HNT specimens decreases continuously due to damage accumulation inside the composite and consequent loss of material stiffness. HNTs increase in-plane shear modulus and strength by 27.3 %, and 20.9%, respectively. These findings agree with the results of other researches related to the nanotube reinforcing effect on CFRP [95, 96] as well as the study of Behrooz et al. [97] where they improved shear modulus and strength of carbon nanotube integrated glass fibers reinforced epoxy composite by 10.6 % and 15.8 %, respectively.

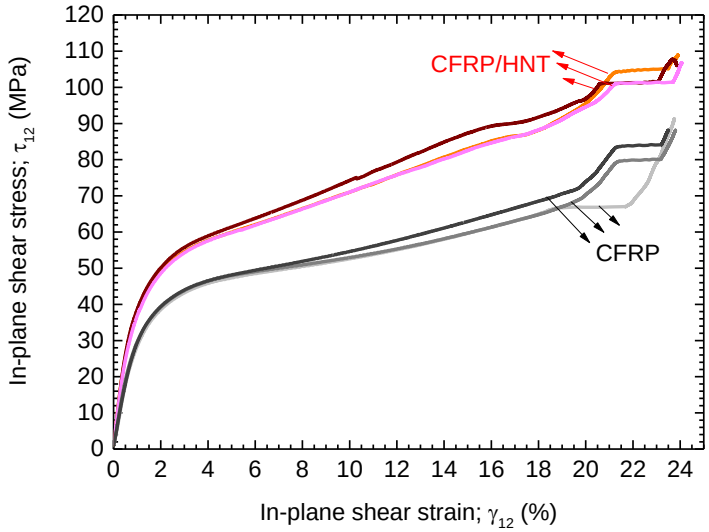

Figure 4.10 Stress-strain curves of CFRP and CFRP/HNT specimens under in-plane shear test where strain is recorded with the strain gages.

By using the previous k-means parameters on AE data during the in-plane shear test, for pristine CFRP, three different clusters are identified as matrix crack (cluster-cr), delamination (cluster-d) and fiber fracture (cluster-fr) which are at WPF ranges of 85-190 kHz, 200-320 kHz and 370-570 kHz, respectively, as shown in Figure 4.11a. It can be observed from Figure 4.11b, that upon the integration of HNTs into the matrix, the WPF range of AE clusters has become wider, which can be related to the presence of HNTs in the matrix and at the interface between fiber and matrix. It may be suggested that HNTs promote micro cracks initiations in the matrix at high stress levels thereby bringing about an increase in WPF range as well as AE count number at lower frequencies. On the other hand, they improve the interface properties thus increasing the frequency range of interface failure. The sum of these two effects results in clusters associated with matrix cracking and interface failure with wider WPF ranges.

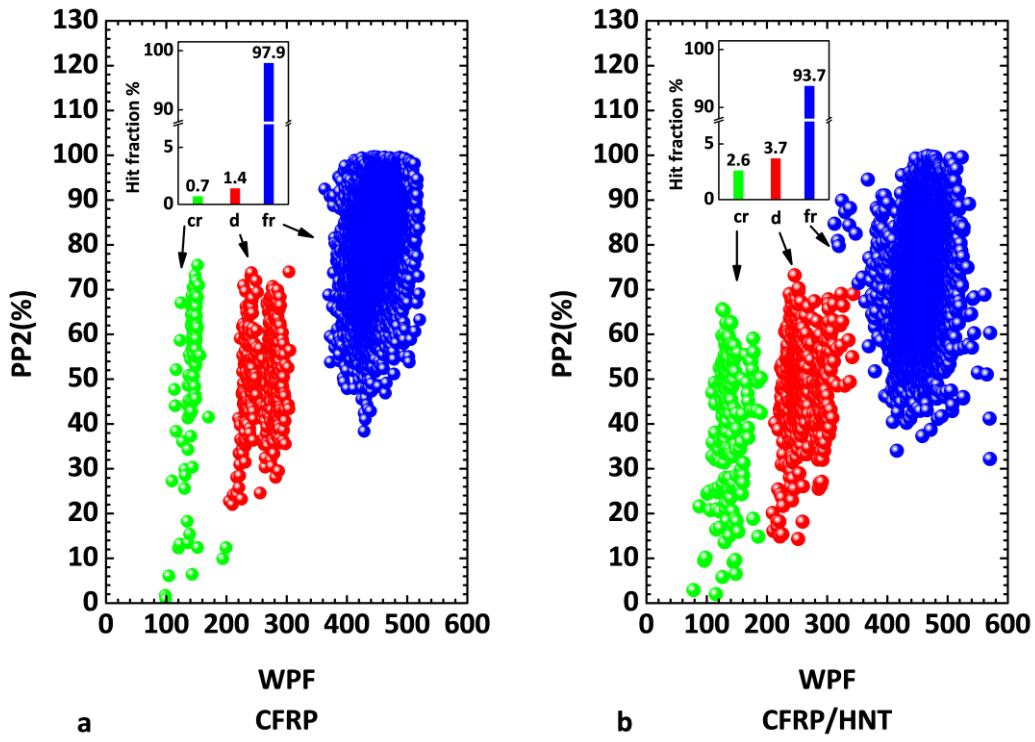

Figure 4.11 AE plots of PP2 vs. WPF for (a) CFRP and (b) CFRP/HNT specimen during in-plane shear test, and (Inset figures) clusters' hit fraction bar plots.

Hit fraction of cluster-cr and cluster-d for pristine sample increase from 0.7% to 2.6% and from 1.4% to 3.7%, respectively, due to the addition of HNTs. The most significant change of failure mechanisms under the flexural loading of CFRP after the addition of HNTs was related to delamination failure as discussed in Figure 4.5b, while for the in-plane shear test, both matrix cracking and delamination mechanisms are increasing significantly. The bonding between epoxy/HNT and the fibers establishes additional interfacial interaction between constituent of the composite material, thus increases AE hits corresponding to interface failure after the addition of HNTs to CFRP.

Furthermore, at relatively higher HNTs concentration, it is inevitable to have local non-uniformities in HNTs distribution in the matrix such that there might be HNTs agglomerations with different sizes as well as isolated ones. As a result, the various failure mechanisms are possible in the matrix. HNTs can act as stress concentration points hence promoting numerous micro cracks initiation [33]. Conversely, HNTs have crack front pinning or bridging effects [47] and can hinder the microcracks coalescence in the direction normal to load as well. According to Deng et al. [93], agglomerated nanotubes cause the

crack to deflect from its original propagation path and result in a favorable new path. Under in-plane shear forces, the composite system shows a non-linear behavior in the stress-strain curve as given in Figure 4.10, since the matrix carries a major fraction of the load. According to the authors previous work [81], such a non-linear behavior is correspondent to micro damage accumulation inside the material. Since the stress values of the non-linear region for HNTs modified CFRP composites are higher than pristine CFRP laminates, it can be suggested that HNTs inhibit matrix deformation more effectively. The highly deformed regions around HNTs clusters act as crack arresters in the composite system. This kind of behavior is similar to the role of the plastic region at the tip of growing cracks. In other words, the presence of HNTs does not preclude the damage occurrence, and instead, delays damage coalescence through altering the crack propagation path. Upon comparing Figure 4.5 and Figure 4.10, it is deduced that the effect of nanomaterials on micro damage accumulation and deformation response of laminates is more profound in in-plane shear as compared to flexural loading.

The change in the behavior of composite due to HNTs integration is associated with the change in the properties of matrix and interface as discussed in the previous sections. For a deeper understanding of HNTs role on damage characteristics, a radar plot of onset ratio (defined as the ratio of the stress level at which the first hit is observed to the one at failure), stress and various AE wave parameters of each of the clusters (average WPF, i.e., an average of WPF value of AE hits for each cluster, duration, i.e., the period of time between first and final threshold crossing, and non-dimensional amplitude, i.e., the ratio of maximum to mean signal amplitude) are presented in Figure 4.12.

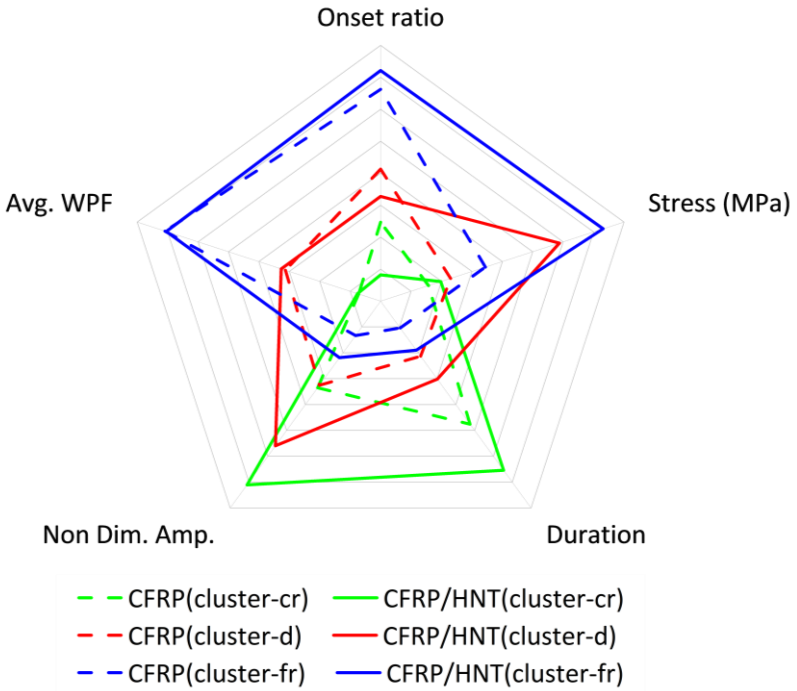

Figure 4.12 Radar plot of onset ratio, stress, and various AE parameters for three clusters (cr, d, and fr) of CFRP vs. CFRP/HNT.

Notably, the average WPF of each cluster does not shift despite the increase in the width of the cluster for HNTs integrated composites as shown in Figure 4.12. This observation indicates that the addition of HNTs does not significantly affect the three different types of failure mechanisms but alters their dominancy. For example, both onset ratios of matrix cracking (cluster-cr) and delamination (cluster-d) decrease after adding HNTs, which can be associated with higher susceptibility of crack initiation at high stress levels due to the presence of HNTs in the matrix. On the other hand, the onset ratio of fiber fracture (cluster-fr) increases, suggesting that HNTs can improve the load transfer between the fibers and the matrix. Furthermore, HNTs integrated laminates show higher amplitude and duration in AE waves as compared to the neat specimens. This observation can be related to the enhancement of the interfacial properties of CFRP/HNT composites, i.e., more energy is required to unlock the matrix/fiber interaction and allow for damage propagation. Figure 4.13 depicts the time-frequency structure i.e., spectrogram plots of AE waves for a randomly chosen data points which have 2048μs length (i.e., 2048 voltage values sampled for each AE hit) from each cluster. In this plot, the normalized frequency, power density, and sample are shown as x-, z-, and y-axes, respectively. Figure 4.13a, 4.13b, and 4.13c present the spectrograms of matrix

cracking (cluster-cr), delamination (cluster-d), and fiber fracture (cluster-fr) for the neat sample, respectively. The main peak of the power for each of these data points occurs at different frequency levels namely $f \leq 200$kHz, $f \leq 370$ kHz, and 370 kHz $\leq f \leq 570$ kHz, respectively. Another observation that reveals a major difference between various failure types is the fluctuation during the attenuation of the waveforms. As seen in Figure 4.13a and 4.13b, the structure of the time-frequency for the AE hit shows a gradual reduction of power density before complete damping in the wave energy. However, for fiber fracture as seen in Figure 4.13c the loss of energy in the material shows a mild decrease followed by a sudden loss of energy in wave over the time-frequency field. On the other hand, Figure 4.13d, 4.13e, and 4.13f show the three failure types associated with matrix cracking, delamination, and fiber fracture for CFRP/HNT sample. It is noticed that the peak values of energy take place at a similar frequency range as pristine laminate, however, the attenuation has reversed. In the case of matrix cracking and delamination, the energy reduction pattern is mild followed by a sudden drop in power density, which is consistent with the improvement in the mechanical properties as seen in the stress-strain curve on bending and in-plane shear (See Figure 4.4 and Figure 4.10). On the other hand, the relative energy reduction for fiber fracture given in Figure 4.13f is gradual as compared to its pristine counterpart in Figure 4.13c. It can be concluded that the addition of HNTs into CFRP laminate changes the evolution of power density for each failure type, which is in direct relation with the mechanical properties of the sample.

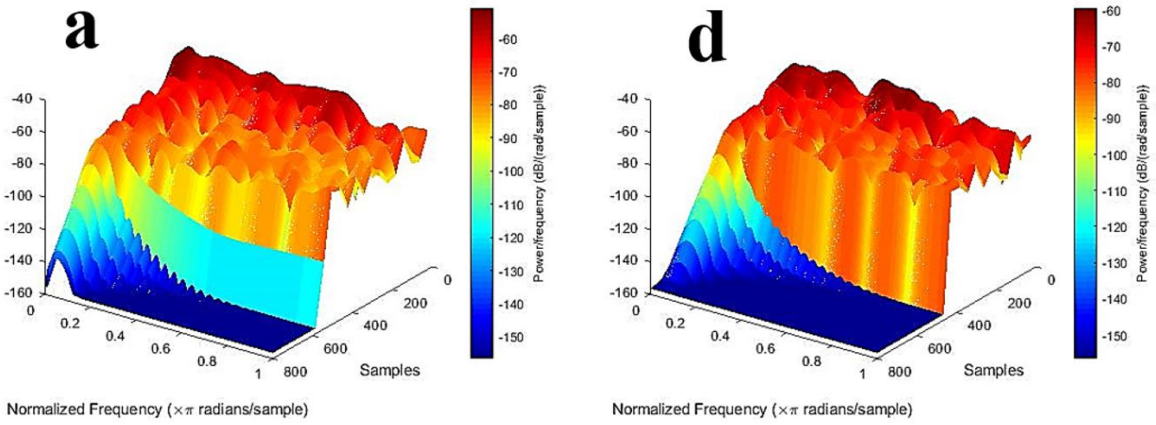

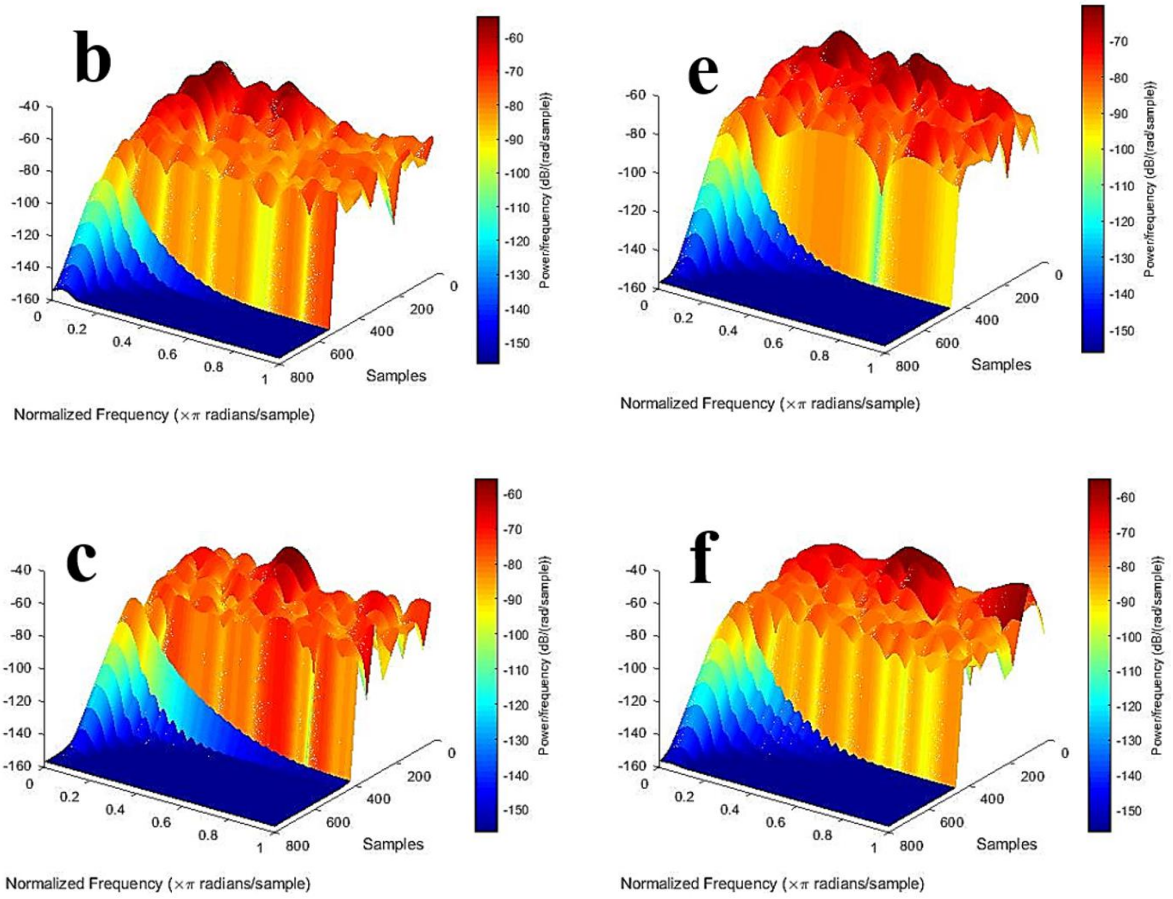

Figure 4.13 Spectrogram of various failure types for CFRP (a) cluster-cr, (b) cluster-d, (c) cluster-fr, and CFRP/HNT (d) cluster-cr, (e) cluster-d, (f) cluster-fr, under in-plane shear stresses.

The correlations between the shear stress-strain graphs and full field shear strain maps obtained from the DIC system are given for CFRP vs. CFRP/HNT laminates in Figure 4.14. Both specimens have nearly the same response to in-plane shear load in the linear region and present a uniform strain distribution in the v-notch region. The non-linear region of CFRP starts at 42 MPa, which is associated with micro damage initiation inside the laminate and creation of a high strain gradient at the v-notch region. After 60 MPa, the contrast on the pristine specimen surface is partially lost in the non-linear region due to the deterioration of the speckle pattern. Therefore, DIC images show gaps in the v-notch region, which can be attributed directly to the coalescence of microcracks into macrocracks.

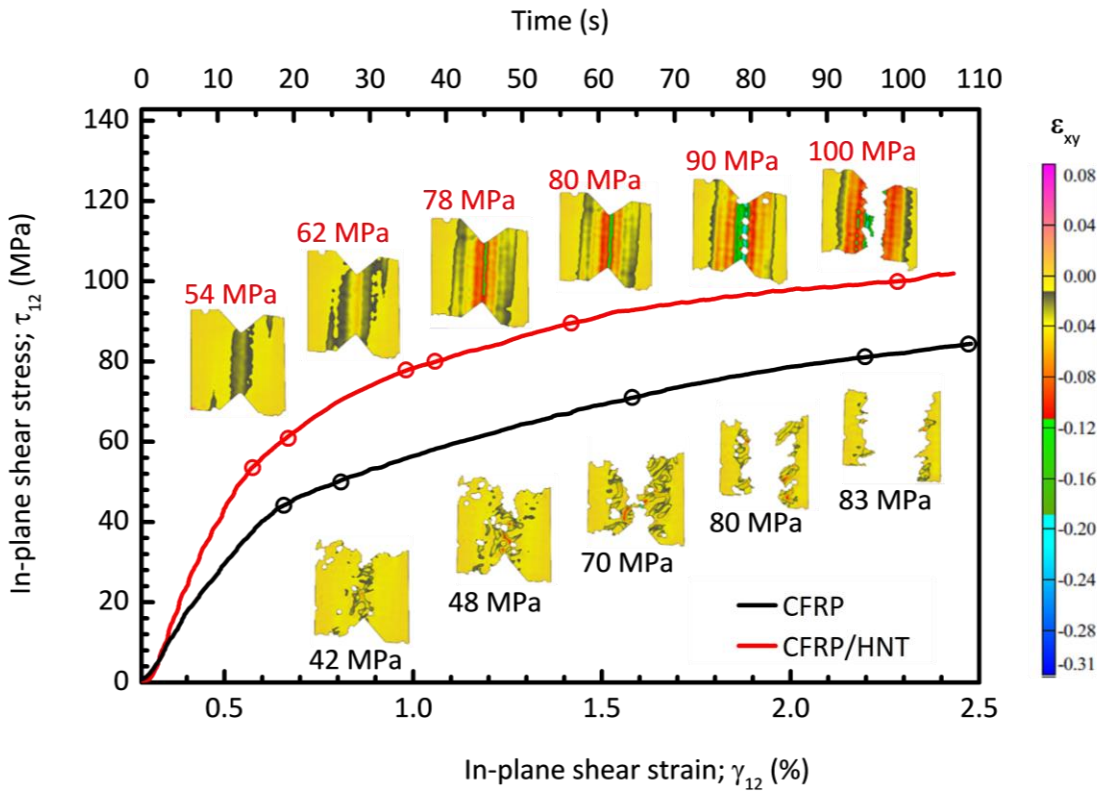

Figure 4.14 Stress-strain plots along with specific DIC images of CFRP, and CFRP/HNT taken at a certain value of stress where the strain data in the plot is recorded with DIC system.

A pure shear strain in the v-notch shear test usually shows a narrow band of a high shear region between the roots of the notches [81]. However, in the case of the current sample for the pristine woven CFRP laminate, such a vertical shear band is not observed. This behavior is related to the early creation of microcracks in resin packet regions and their consequent coalescence which forms a zigzag path for damage between the top and bottom notches. In contrast, the shear strain maps for CFRP/HNT laminates demonstrate the expected vertical shear band, which indicates that HNTs integration might prevent the coalescence of microcrack by a combination of two effects such that; the interface of fiber-matrix becomes resistant to failure development due to HNT addition and HNTs clusters in the matrix act as a barrier and pin the tip of the crack during the in-plane shear test.

The synergic effect of the mentioned mechanisms obviates the progress of the damages in the v-notch region in a stepwise path as shown in Figure 4.15, where the schematic graph shows the examined cross section parallel to one side of the v-notch, and 0°- and 90°-degree fibers are parallel and perpendicular to the examined plane, respectively. SEM images in

Figure 4.15 shows the evident cracks as depicted in the schematics, therefore providing the evidence for the effect of HNTs in hindering the growth path of the cracks.

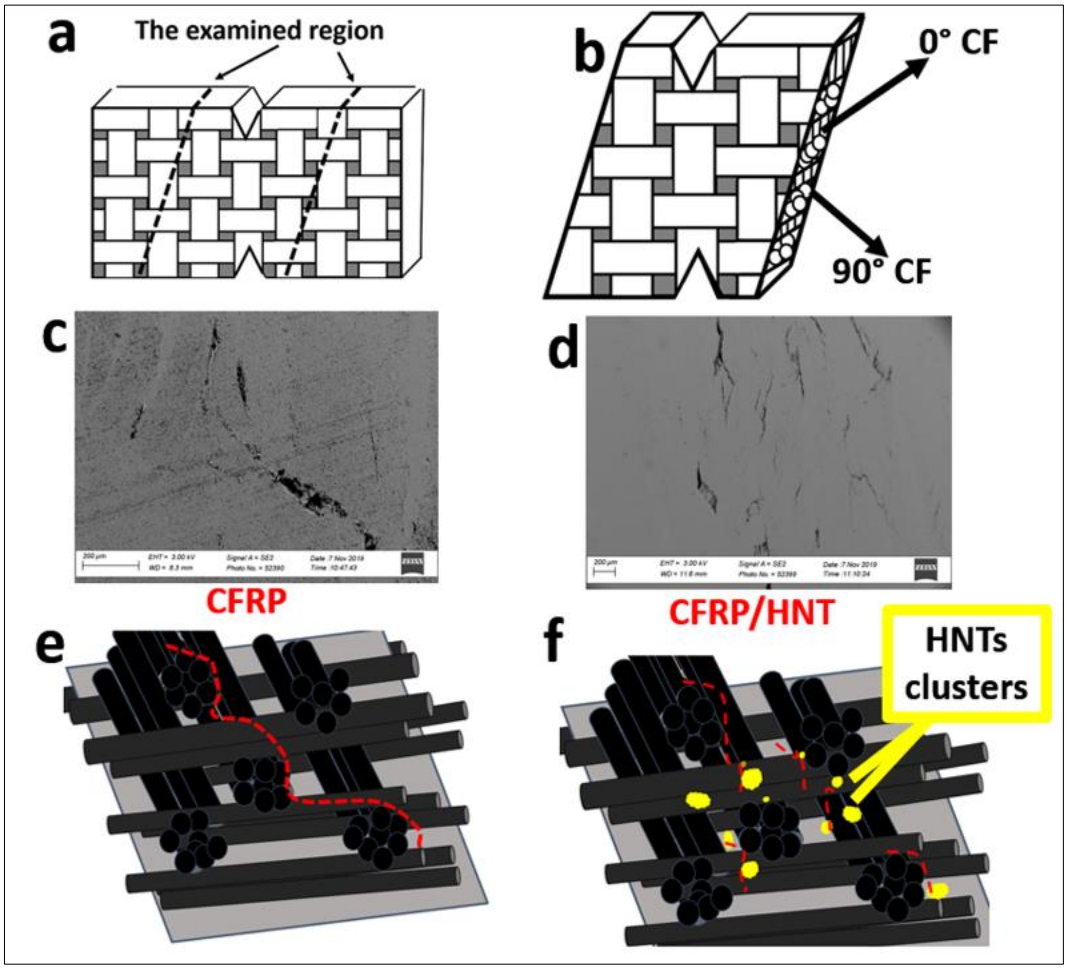

Figure 4.15 (a) Schematic graph of the examined plane from a specimen after global failure under in-plane shear load, (b) direction of plain woven CF at the examined plane, (c) SEM micrograph of CFRP specimen, (d) SEM micrograph of CFRP/HNT, (e) schematic of crack propagation in CFRP specimen, and (f) schematic of crack propagation in CFRP/HNT specimen.

To observe the effect of HNTs on the mechanical performance of the CFRP composite, in Figure 4.14, DIC images for the axial and transverse strains (ε_{xx}, ε_{yy}) are presented with intervals of 10 MPa of in-plane shear stresses up to the breaking point. The comparison of ε_{xx} strain maps in both specimens shows that there are random localized strain points from an early stage of the test until 30 MPa stress level. At 40 MPa, high strain regions appear and spread toward the edges of the specimen until the global failure. On the other hand, the strain distribution in CFRP/HNT is uniform until 50 MPa. At higher stress levels, the concentrated

strain areas appear discretely between the roots of the v-notches and despite the growth of damage, they remain confined in the mentioned region until the global failure.

DIC images in Figure 4.16, in both ε_{xx} and ε_{yy} show similar damage development, however, with the presence of HNTs in the composite system, highly localized strain regions (distinct strain spots) are not observed until 70 MPa stress value. Thus, it can be implied that there is more resistance to crack propagation along the y-axis direction at the fiber/matrix interface and HNT-matrix system.

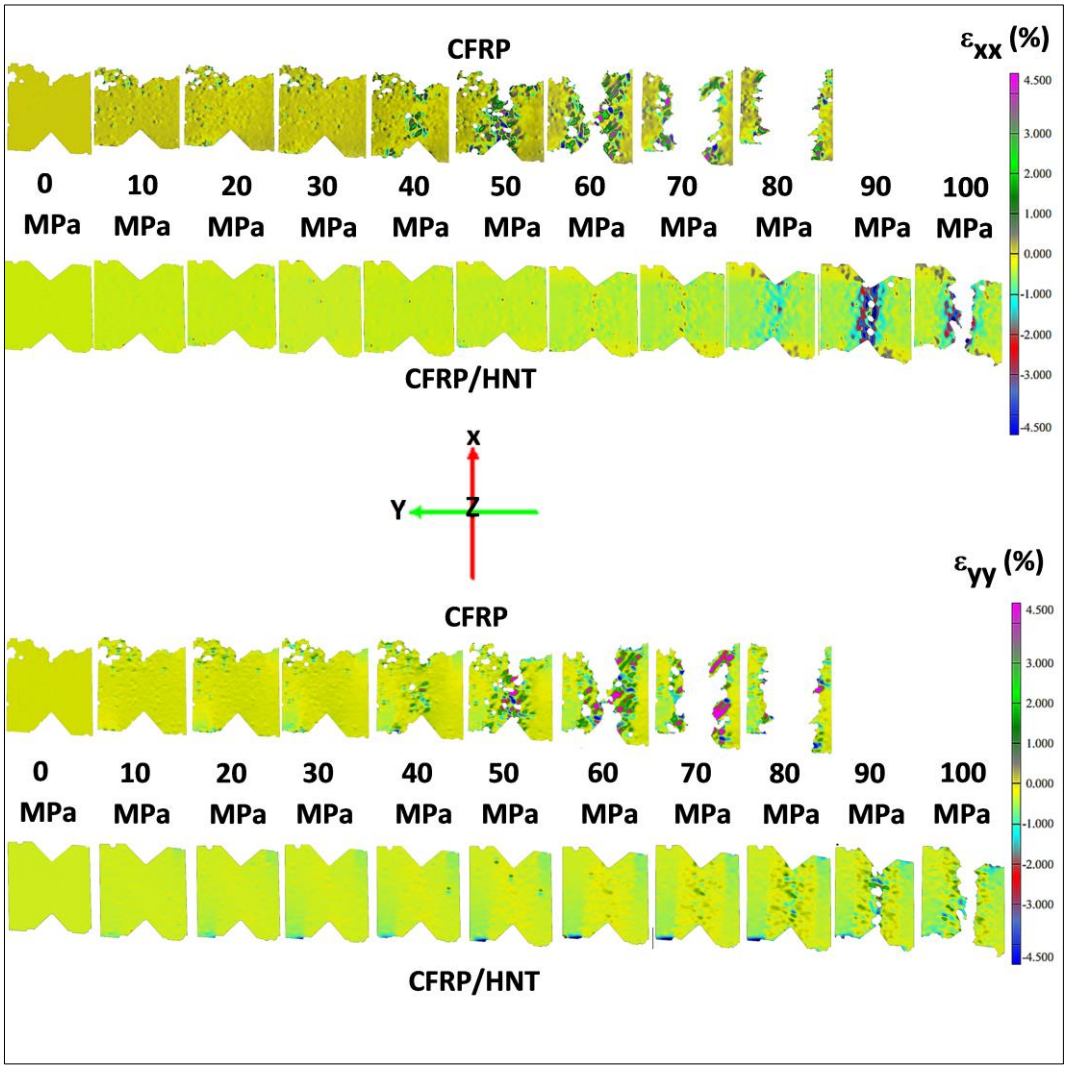

Figure 4.16 DIC frames of calculated average axial (ε_{xx}) and transvers strain (ε_{yy}) during in-plane shear test for CFRP vs. CFRP/HNT laminates. The pristine specimens failed at lower stress values than the HNTs integrated one, therefore, there is no DIC strain map above 90 MPa.

Figure 4.17 presents the in-plane shear stress-strain curve accompanied by IRT images taken for CFRP and CFRP/HNT during the in-plane shear test. Each of these images is chronologically correlated with a bold circle on the stress-strain curve. IRT images related to CFRP laminate are indicated in a black frame while the images taken for CFRP/HNT are given in red frames. Thermal maps are used to calculate the temperature difference (ΔT) between the minimum and the maximum temperature at identical regions of interest (ROI) for both specimens. The ROI is an area defined at the middle of the v-notch shear specimen with dimensions of 30 mm by 20 mm in x-and y-directions.

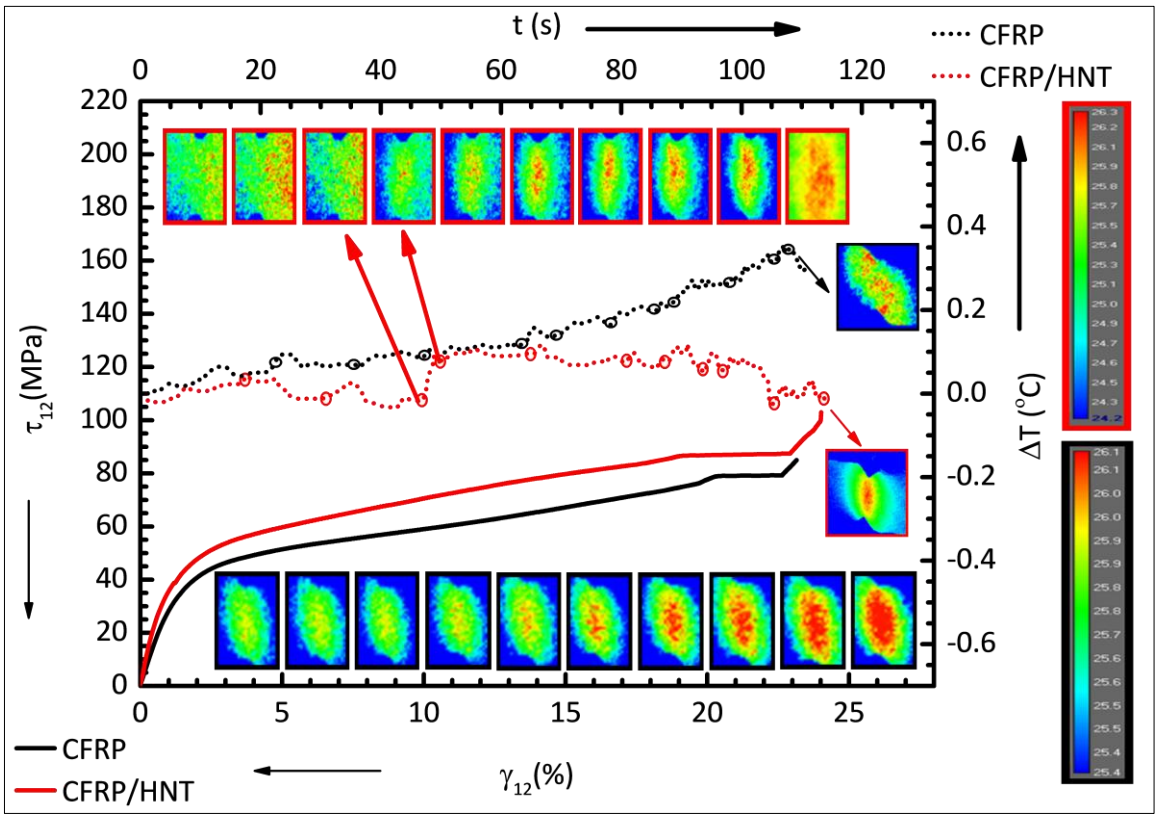

Figure 4.17 Average temperature changes vs. stress (MPa), and IRT images of various points with increased stress from left to right. CFRP images within black frames vs. CFRP/HNT within red frames.

At the beginning of the in-plane shear test, ΔT values for both samples are negligibly small given that no sufficient damage formation has taken place. At about 75 MPa, the variation of temperature in the ROI of CFRP starts to increase gradually until failure. On the contrary, ΔT values of CFRP/HNT specimen show a subtle variation with only a single jump around

75MPa. The range of ΔT for pristine sample varies between 0 ℃ and 0.36 ℃ while for CFRP/HNT remains between 0.0 ℃ and 0.1 ℃ throughout the test.

This observation can be explained as follows. As seen in AE results in Figure 4.11, the presence of HNTs in the composite system causes a reduction in fiber fracture events owing to better interface interaction and matrix stiffening mechanisms, which have higher thermal energy release [98]. On the contrary, the delamination and matrix cracking increase, and these events are characterized by smaller energy release compared to carbon fibers fracture. Moreover, the existence of HNTs in the composite system hinders the coalescence of microcracks thereby circumventing the formation of macrocracks. To this end, heat generation due to the friction between the surfaces of macrocracks under the applied load is eliminated to a certain extent. In our parallel study, we have observed that HNTs improve the thermal conductivity of the CFRP/HNTs composite. As a result, HNTs in the composite system causes more homogenous thermal distribution in the v-notched region.

One can notice a rise in ΔT of CFRP/HNT plot between 55 MPa and 65 MPa. According to two IRT images taken at these points (indicated by red arrows on the figure), this jump in ΔT is related to the formation of thermal emission points at the center of the v-notch region where the shear stress is maximum. The last two IRT images with larger ROI as compared to the rest of IRT images are taken at the instant of global failure for both specimens. There is an obvious difference between IRT images of the two composites at the final failure point where thermal emission region in CFRP shows heterogeneous thermal map extended toward the edges of the sample while the counterpart region in CFRP/HNT appears to be more localized with a distinctive gradient from the v-notch center toward the outer edges. This is consistent with DIC results as seen in Figure 4.14, where the higher strain values of CFRP/HNT are localized within the v-notch region until the end of the test.

4.4.5. PD analysis results

To implement the numerical approach for the current study, the resulted morphology of nano materials in the matrix can be assumed as analogous to holes inside the material. As observed in micrographs of Figure 4.15 and explained for AE analysis results, nano materials promote crack initiation and deflect the progressing cracks inside the hybrid material.

In addition, the material stiffness coefficients (i.e., constitutive elastic constants) of the plain-woven laminate when stacked as cross-ply layup become analogous to constitutive relations of transversely isotropic material. Besides, the applied loading conditions specified herein is a pure in-plane shear load, thus enabling the utilization of plane stress condition to disregard the effect of transverse stiffness of the laminate. Consequently, when subjected to in-plane loads, the present material properties of the plain-woven laminate can be suitably represented as an isotropic material.

Therefore, the relative physics behind the effect of HNTs on damage progress of plain-woven composites is presumably like the effects of the holes inside a 2D continuum of an isotropic material. Since the HNTs are distributed in the matrix material and the shear response of the composite is a matrix dominant property [99], we have chosen to simulate the v-notched shear tests to support the experimental observations. In this regard, using the OSB formulations given in Section 4.3, various v-notched plates having different densities of randomly generated holes are numerically investigated under the shear loading condition for an isotropic sample. The material used herein possesses a Young modulus of E = 2.94 GPa, a Poisson Ratio of $\nu = 0.38$, a density of ρ = 1200 Kg/m^3, and a critical energy release rate of Gc = 602 J/m^2.

In order to obtain computational results in a feasible time, the loading is applied with the velocity boundary condition of 20 (m.s^{-1}) in the y-direction to a 23 (mm) portion of the right end of the plate while the 23 (mm) portion of the left end is fixed in x- and y- directions as depicted in Figure 4.18. For all the analyses in this section, the distance between material points is taken as dx = 0.1 mm, thus, leading to a point discretization of 760 × 190 in x- and y-directions, respectively. The incremental time-step size is taken as $dt = 4.25 \times 10^{-8}$ minute, and the failure of the bonds is allowed only in tension.

To analyze the effect of holes, i.e. nanotube clusters, on growth of cracks and their coalescence, two cases are investigated. The case without initial cracks (Figure 4.18a) is used to explore the dynamics of initiation and crack growth at different densities of holes, namely, without holes, low density and high density of holes. The case with initial cracks (Figure 4.18b) is analyzed with and without the holes to certify the assumption of hindrance in crack coalescence with the presence of holes, i.e. delay in merging of microcracks.

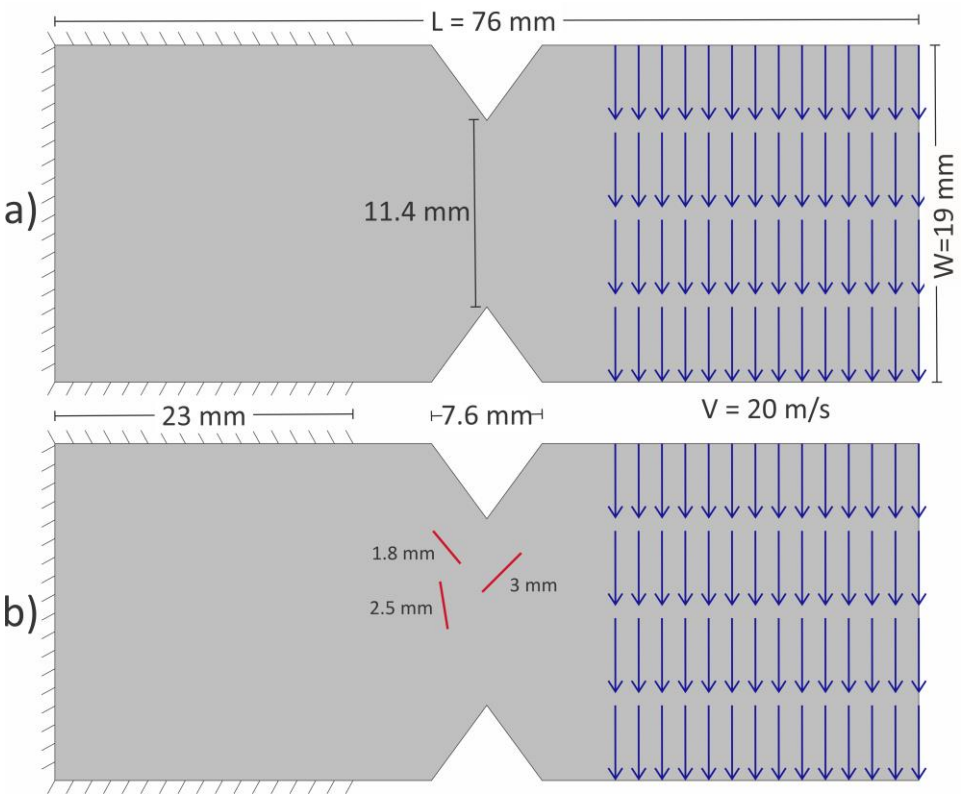

Figure 4.18 Geometric properties of the v-notched plate and its loading condition, (a) without cracks, (b) with three randomly generated microcracks.

As the first step, the plate is solved with no holes to have a reference on crack dynamics where the propagation of the crack is determined to start from the upper notch of the plate at 370^{th} time-step and reach the fixed boundary approximately after 850 time-steps. Accordingly, the crack propagations between 400^{th} and 800^{th} time-steps are taken as the basis of comparison. Figure 4.19 shows the propagation of the crack after 600^{th}, 700^{th}, and 800^{th} time-steps at the central portion of plates having zero, low and high density of randomly generated holes, given that no failure has occurred in other regions.

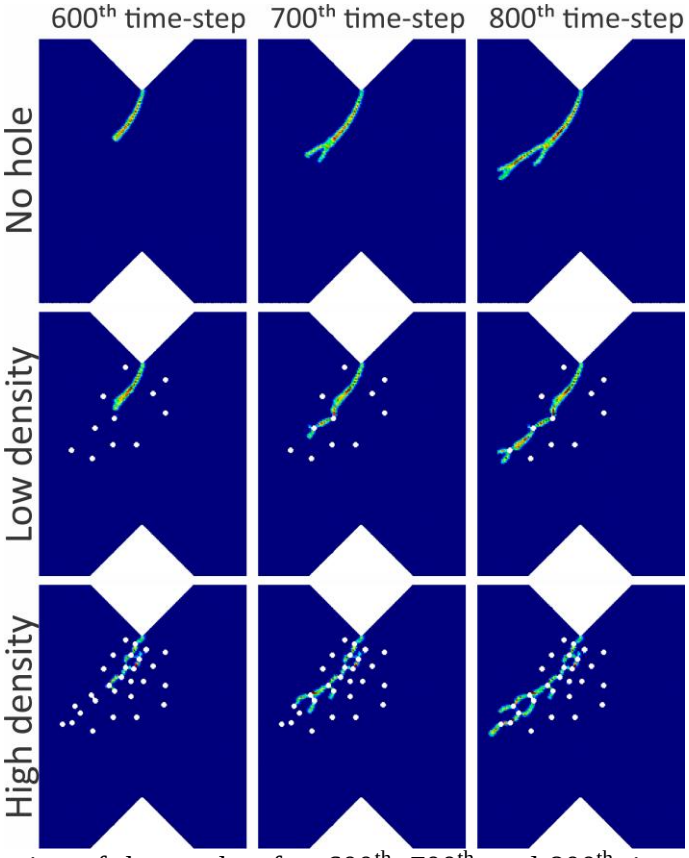

Figure 4.19 Propagation of the cracks after 600th, 700th, and 800th time-steps at the central portion of plates with zero, low and high density of randomly generated holes.

As seen in Figure 4.19, the presence of holes, i.e., clusters of nano materials in experiments, deflects the path of crack propagation and promotes branching of the growing crack. The higher density of holes inside the material causes a higher crack branching, such a bifurcation in crack path results in crack branches having a lower potential at the tip. The energy reduction at crack tip eventually leads to a decrease in propagation velocity of the crack as seen in Figure 4.20, which shows the change in length of the cracks with respect to time. The slope of the lines in Figure 4.20 at any instant of time indicates the average velocity of the crack propagation between the neighboring time steps. These numerical results support previous findings in AE analysis, DIC and IRT images as discussed in the previous sections, wherein for neat samples the release of failure energy is more abrupt as compared to HNTs integrated laminates. The faster AE energy release in pristine laminate observed as big leaps in acoustic emission counts is directly related to the fast growth of cracks inside the material that is consistent with rapid damage progress of the sample without holes in Figure 4.20. On the contrary, as seen in Figure 4.6b, the gradual increase of AE counts for HNTs integrated

specimen is related to the lower speed of crack development inside this composite material, i.e., the crack growth in HNTs laminate is similar to the high-density specimen in Figure 4.20. Moreover, the experimental results, presented in Figure 4.17, show that the thermal energy release associated with failure events in the pristine specimens have higher magnitude indicating the higher potential of the failure, which is consistent with numerical observation depicted in Figure 4.20, for the sample without holes. On the other hand, the addition of HNTs to the system resulted in lower magnitude failure events that are analogues to the numerical observations for samples with holes.

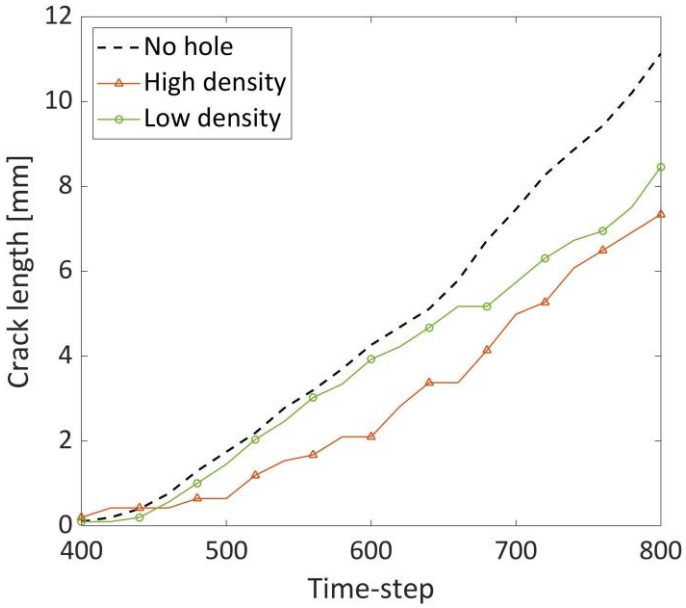

Figure 4.20 Total crack length in plates with zero, low and high density of randomly generated holes.

Overall, the presence of nanomaterials inside the laminates causes a similar effect as the presence of the holes in the specimen under in-plane shear loading, as seen from the crack dynamics in Table 4.3. The length of propagated crack for the sample without the holes is the highest as compared to the specimens with holes. Moreover, the highest effect of holes on crack propagation velocity and length is seen in the geometry with a high density of holes where the velocity and the length of the crack propagation have decreased approximately by 35% and 34%, respectively.

Table 4.3 A comparison of plates with zero, low and high hole densities by means of crack dynamics.

	No hole	**High density**	**Low density**
Crack propagation initiation time-step	370	355	360
Total length of the crack after 400 time-steps [mm]	0.10	0.20	0.10
Total length of the crack after 800 time-steps [mm]	11.13	7.34	8.46
Average velocity between 400th and 800th time-steps [mm/time-step]	0.027	0.0179	0.0209
Difference in average velocity with respect to no hole geometry	-	-35.27 %	-24.21 %
Difference in crack propagation length with respect to no hole geometry after 800 time-steps	-	-34.05	-23.99

Figure 4.21 shows the failure results of initially cracked samples with and without holes. It is clear from the results that after approximately 600^{th} time steps, the microcracks in the plate without holes start to merge, thus resulting in the growth of crack coalescence. However, in the sample with holes, the coalescence of cracks is prevented at the identical time steps as compared to the case without holes. These results are consistent with the experimental observations obtained through DIC and IRT analysis, where the existence of HNTs in the composite specimens causes the shear band to remain confined within the v-notch region (in Figure 4.14) and the dissipation of thermal energy becomes more homogenous due to prevention of crack coalescence.

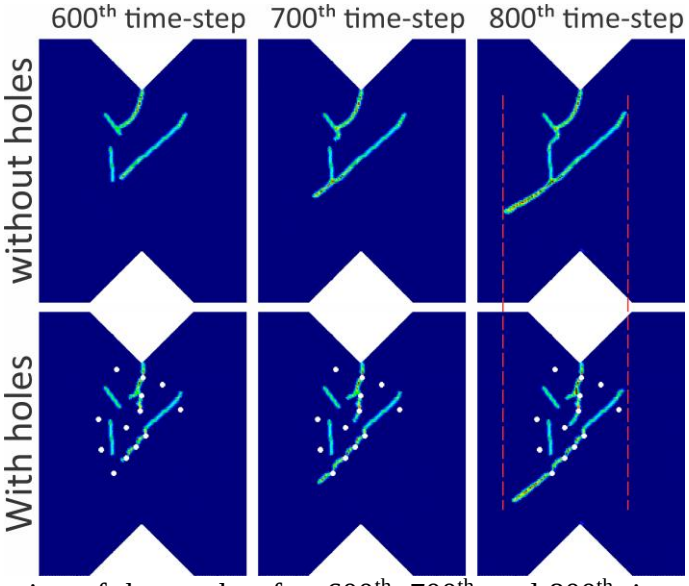

Figure 4.21 Propagation of the cracks after 600th, 700th, and 800th time-steps at the central portion of plates with and without holes having randomly generated microcracks.

4.5. Conclusions

CFRP and CFRP/HNT laminates are successfully manufactured and their mechanical responses are monitored under flexural and in-plane shear loading conditions. The flexural- and in-plane shear moduli are improved by 18.1% and 27.3%, respectively. Based on AE results and SEM fractography analysis, it is found that HNTs primarily affect matrix cracking and delamination mechanisms. The damage accumulation becomes less severe and more gradual with smaller steps as can be concluded from AE cumulative counts.

The strain fields and thermal maps for the in-plane shear tests show consistent results in terms of damage progress. The role of HNTs in hindering crack growth, crack tip splitting and in turn crack coalescence in CFRP/HNT specimens is evident by the formation of a pure shear region in DIC strain maps and a homogenous thermal energy release in the IRT images. The experimental findings as to the effects of HNTs on the damage mechanisms in the composite system are confirmed with peridynamic analysis where nanotubes clusters in the matrix of composite laminates are represented by arbitrarily positioned holes. The numerical results demonstrate that HNTs clusters obstruct crack growth, encourage crack tip splitting, and consequently, circumvents the crack coalescence.

CHAPTER 5. EFFECT OF INFUSION PATH IN RESIN TRANSFER MOLDING ON THE INTERFACIAL INTERACTION IN CFRP/HNTS COMPOSITES

5.1. Introduction

The performance of CFRP is highly affected by the interfacial properties between the matrix and the fibers. One approach to improve these properties is to integrate nanomaterials into the composite system [52, 53, 66, 100]. Interfacial properties depend on both, the physical and the chemical interaction between the nanomaterial, the matrix, and the carbon fibers. HNTs contribute/facilitate the curing process of epoxy polymer [48]. Besides, when used in CFRP polymeric composites, HNTs have more affinity toward the carbon fibers than the epoxy, and can form bonds with the fibers surface which improve the interface ability to transfer the load from the matrix to the fiber, and consequently increase the composite toughness [25].

RTM is widely used for rapid manufacturing of small parts with high fiber volume fraction, high quality on both sides of the composite plate, and a at high production rate [101-103]. Resin properties (e.g., viscosity, and gel time), fiber volume fraction, and injection flow rate are some of the factors that highly affects the end product [104]. Various types of ordered arrangements of fiber tows such as woven, stitched, or braided fabrics can be used [105]. RTM involves long-range flow of resin through the pore space between the reinforcement fibers. Concerning the fibers effect on RTM process, various studies focus on either the fiber type and fiber modification technique on the impregnation process [106] or the aligning of the fiber in accordance to the flow path (i.e., parallel, perpendicular). While other studies investigated the effect of the port locations on the quality of the preform filling. For example, fingering process can occur due to difference between the fiber tows and the tow gap permeability which *trap* air (i.e., voids) in the laminate [107]. Void formation increases when nanoparticles are used because they affect how the resin-front flows and increase the infiltration phenomena [102]. By employing Darcy's law, it is possible to observe a decrease in the front flow speed due to the pressure gradient. Controlling the pressure gradient within the mold adds to the importance of correctly allocating the injection ports to maximize the efficiency of the wetting process [101]. Finding the right design of RTM mold through trial-

and-error is an expensive and time-consuming process. Simulation modulus to optimize the design of RTM mold are highly important tool to shorten the design process and lower its cost. Those simulations require experimental results obtained from processes that are designed with simple parameters, as input for simulation by impregnation models [108-110]. Another critical issue during the manufacturing, is acquiring data about particle deposition when nanomaterials are used. Deposition of particles occurs during injections of particle-filled resins into porous reinforcements, resulting in clogging of the pores [108]. The clogging leads to a decrease of the permeability [107], which is highly undesirable for processing, since it leads to an increase in the filling times, a risk of incomplete mold filling, and the production of inhomogeneous particle distribution within the composite plates [109].

In literature and up to this date, no comparison is made between two RTM mold that are different in the infusion bath, and how this affects the properties of CFRP composites. Additionally, knowing that the presence of nanomaterials in the injected resin will add to the complexities of the manufacturing process and alters the properties of produced composites, it is necessary to investigate how the application of different infusion path reflects in the final properties of the cured composites, such as the average void content and the mechanical properties of CFRP composites.

In this research, HNTs are added to the resin prior to the injection into the mold, and it is expected that HNTs will cause a local deviation in the permeability. This stems from the tendency of HNTs to form clusters with various diameters once the resin mixture has settled in the injection pot before the injection process, where some of the clusters can exist in the micro scale. These micro clusters surge the filtration of the nanotubes throughout the weave tows [102]. In order to mainly compare the effect of the resin infusion path on the loading of HNTs within CFRP composites, simple geometry molds were designed, and 2D plain woven carbon fibers were used. The two RTM molds have similar shape (i.e., rectangular plane) but differ in the positioning of the inlet/outlet ports, and this results different injection path. The first RTM (RTM(I)) has a linear resin flow, where in the second RTM (RTM(II)), the resin flow path is curved. CFRP composites with and without HNTs were manufactured in both RTM molds. Specimens from the resulted plates were tested under three-point bending and in-plane shear loads. The relationship between void content and mechanical properties are discussed in detail.

5.2. Experimental

5.2.1. Materials

HNTs with the size of d_{98} = 9.95 µm, d_{90} = 5.01 µm, and d_{50} = 0.53 µm and the specific surface of 128 m^2/g are supplied by ESAN, Turkey. Two components DGEBA epoxy (ARALDITE® LY 1564 SP resin and XB 3403 hardener) are purchased from HUNTSMAN.

5.2.2. Manufacturing of CFRP and CFRP/HNT composites by RTM

CFRP (i.e., N) and CFRP/HNT(10 wt.%) (i.e., NT) composites were manufactured in both RTM molds as explained with details in previous work [25] and Chapter 4. CFRP and CFRP/HNT plates that are produced via RTM(I) are labeled as N(I), NT(I), respectively. Similarly, CFRP and CFRP/HNT plates which are manufactured by RTM(II) are labeled as N(II), and NT(II). Figure 5.1a, and Figure 5.2a show RTM(I) and RTM(II) molds with the inlet and outlet ports numbered in the mold image. Additionally, the schemes in Figure 5.1b and Figure 5.2b clarify the main flow path in each mold with blue arrows. In RTM(I) the mixture is injected at Port.1, flows in the designed channels along the edges of the mold cavity, and gradually wet the fibers. The excess resin is discharged through the outlet Port.2 and Port.3.

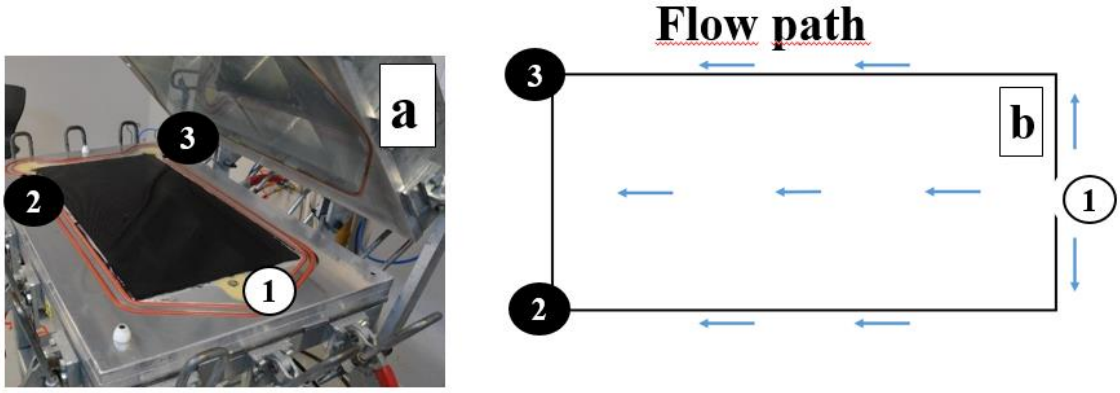

Figure 5.1 (a) RTM(I) mold contains a cured NT(I) composite plate, (b) Schematic representation of the mold cavity in RTM(I) mold with blue arrows that represent the flow direction of the resin.

While in RTM(II), the inlet Port.4 is located in the middle of one side of the mold cavity, flows along the edge around the mold cavity, pass through fibers, and then get sucked out through the outlet Port.5 which is located at the center of the plate.

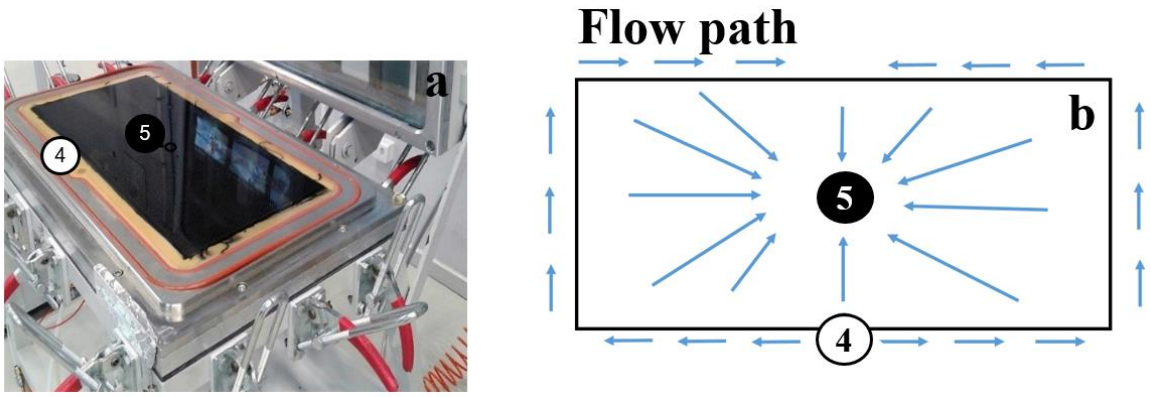

Figure 5.2 (a) RTM(II) mold contains a cured NT(II) composite plate, (b) Schematic representation of the mold cavity in RTM(II) mold, with blue arrows that represent the flow direction of the resin.

12 layers of CFs are used in RTM(I) vs. 14 CF layers are used with RTM(II). The weight fraction (wt. %) for the composite components are calculated using TGA measurements and listed in Table 5.1. Figure 5.3 shows the detailed steps that are followed to prepare the specimens needed for experimental tests.

Table 5.1 Weight fraction (wt. %) of N(I), NT(I), N(II), and NT(II) composite plates.

Composite plate	**CFs (wt. %)**	**Epoxy (wt. %)**	**HNTs (wt. %)**
N(I)	50.4	49.6	-
NT(I)	51.6	43.8	4.6
N(II)	51.7	48.3	-
NT(II)	49.2	46.8	4

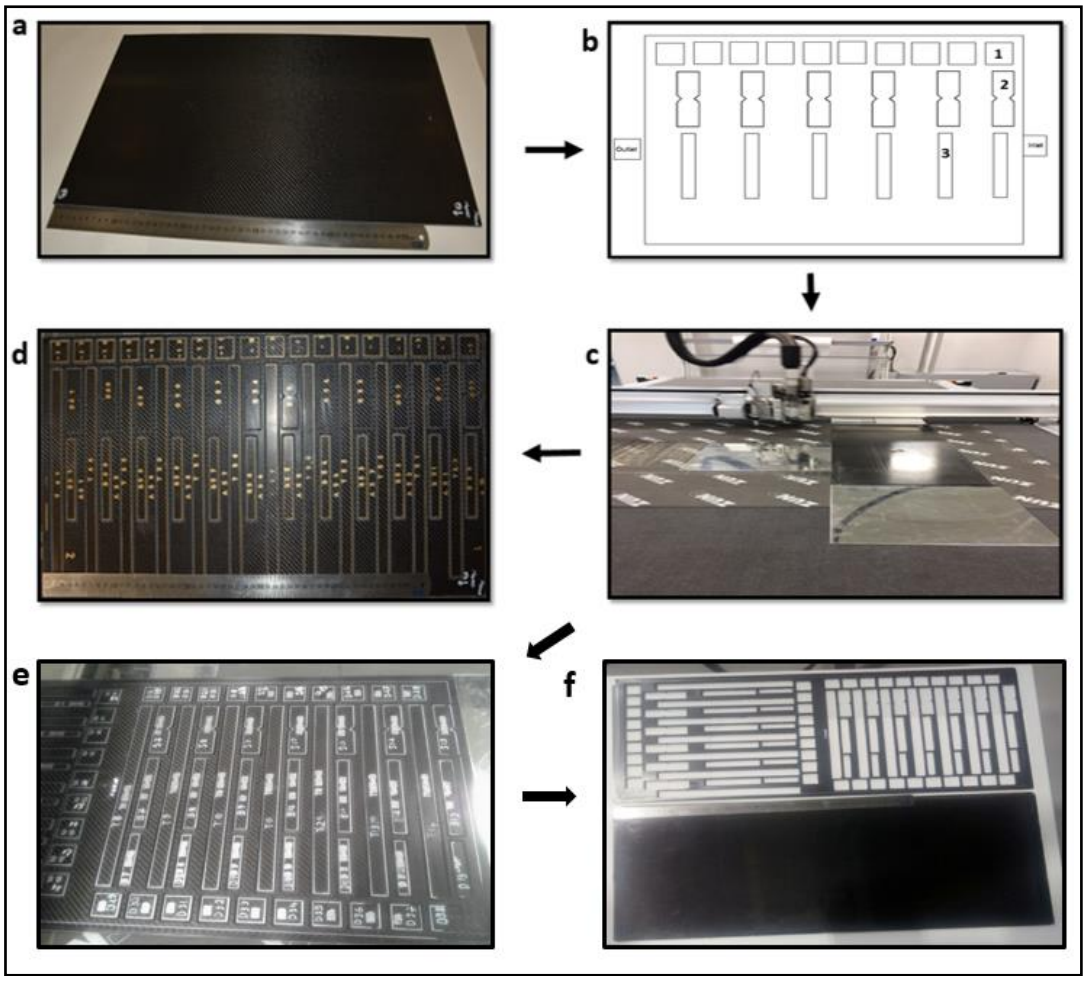

Figure 5.3 (a) trimmed NT(I) composite plate, (b) scheme of the specimens nesting layout for RTM(I) plates, (c) NT(I) composite plate during specimens cutting in a robotic cutting machine, (d) NT(I) specimens for various experimental tests, cut and ready to be collected from a plate, (e) NT(II) specimens for various experimental test, cut and ready to be collected from the plate, (f) NT(II) plate after collecting the specimens shows two directions of specimens nesting with relative to the injection Port.4.

5.2.3. Characterization

The density of CFRP and CFRP/HNT composites are measured according to ASTM D792, through specific gravity analyzer (AUW balance + SMK-401 kit for measuring specific gravity analysis by immersing method, using a weighing pan for standard samples) from Shimadzu. The specimens are cut as 25 mm x 25 mm squares, and measurements are performed three times for each specimen. Void volume fraction (V_v) is calculated for each composite plate according to the D3171-B, where after finding the specimen density, the polymeric matrix is then dissolved and the weight of the undissolved fibers will be determined. From the specimen density, constituent densities, and the fiber content, the

reinforcement content, matrix content, and void content can then be determined. Mechanical tests were conducted using Instron 5982 equipped with a static load cell of ±100 kN. To find the flexural modulus of composite material, flexural tests were performed in accordance with ASTM D790-03, with a constant speed of 2 mm/min., and a span-to-depth ratio of 16:1. The dimensions for flexural test samples of the CFRP laminate are 76 mm × 12.7 mm × 4 mm, while the dimensions of NT(I) specimens are 76 mm × 12.7 mm × 3.5 mm. In order to find the shear modulus, in-plane shear test was performed according to ASTM D5379 using Iosipescu shear test fixture, with a constant load speed of 2 mm/min.. Biaxial rosette strain gauges from Micro-Measurements were used with an exposed solder tap area of 1.0 mm x 1.8 mm, a grid resistance of 350 ± 0.6% ohms, and a gauge factor of 4.728.

5.3. Results and Discussion

5.3.1 Density and void content

Table 5.2 contains the average void volume fraction ($\overline{V_v}$ (%)) for 6 specimens, at two different locations for N(I) and NT(I) plates, and for 12 specimens at four various locations for N(II), and NT(II). Overall, when comparing RTM(I) and RTM(II) plates, RTM(II) produced plates that contain higher void content compared to RTM(I) and this will affect the properties of the composites under stress. But, when comparing CFRP and CFRP/HNT that were manufactured with the same RTM mold it is found that for RTM(I), $\overline{V_v}$ in NT(I) increased by 6% compared to N(I), however, for RTM(II), $\overline{V_v}$ for NT(II) decreased by 17% compared to N(II).

Table 5.2 Average void volume fraction ($\overline{V_v}$ (%)), and average density ($\bar{\rho}$) for N(I), NT(I), N(II), and NT(II) specimens.

	N(I)	**NT(I)**	**N(II)**	**NT(II)**
$\overline{V_v}$ **(%)**	0.46 ∓ 0.11	0.48 ∓ 0.04	0.56 ∓ 0.04	0.46 ∓ 0.05
$\bar{\rho}$ **(g/cm^3)**	1.42 ∓0.01	1.47 ∓0.00	1.42 ∓0.02	1.45 ∓0.01

SEM images of HNTs powder [25] shows that there is large particles (in the 100–200 nm range), and this may favor filtration since the space between the fiber tows is of the order of 100 nm. Figure 5.4a presents densities of N(I) and NT(I) specimens as a function of their location, which is calculated as the distance (r) between the center of the inlet.Port.1 and the center of each specimen). Knowing that the density (ρ) is the ratio of the specimen mass to

its volume, and that all specimens from the same composite plate have the same volume (∓ 0.01% mm^3), any difference in densities for specimens from the same plate is correlated to differences in mass. A specimen with higher density is a specimen with higher mass (less porosity) compared to the other specimens from the same plate. Table S5.2 contain the average density ($\bar{\rho}$) of 18 specimens from N(I) and NT(I) and 38 specimens from N(II) and NT(II) plates.

The density values for N(I), NT(I), N(II) and NT(II) composites' plates are plot as a function to their distance from the inlet port (Figure 5.4). In N(I) specimens, ρ for all specimens with r < 50 cm are below $\bar{\rho}$ value. ρ decreases slowly from the inlet till the middle of the plate and then it starts to increase gradually. In other words, the void content increase in N(I) plate from the inlet to r = 37 cm, then it starts to decrease toward the outlet ports, in the second half of the plate, away from the inlet. However, it is the opposite case for NT(II) specimens where, the majority of the densities value are above $\bar{\rho}$ of NT(II) density until r = 50 cm. This means that void content decreases from the inlet (r = 0 cm) to the middle of the plate, then it starts to increase gradually. The presence of approximately of HNTs in the plate decreases the porosity slightly in the middle region of the plate.

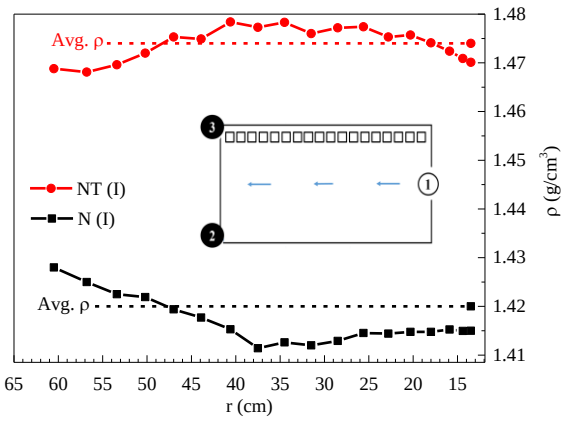

Figure 5.4 Density (ρ) of N(I) vs. NT(I) specimens as a function of the distance (r) from the injection port, with the average density ($\bar{\rho}$) for N(I) specimens is indicated by black dashed line, and for NT(I) specimens by a red dashed line. Inset: scheme of RTM(I) composite plate with squares that represents the location of the tested specimen.

In N(I) where the system is prone to trap air and form voids (i.e., 20 cm < r < 48 cm), and with the presence of HNTs in NT(I) plate, HNTs cluster and fill those volumes, which results in less void compared to N(I). The higher the flowing rate (i.e., near the outlet) the

less pores are generated in N(I) and the load of the resin in N(I) laminates increase. On the other hand, the presence of HNTs precipitated within the fibers obstruct the flow and results in raise in void content closer to the inlet.

2D density graphs for N(II) and NT(II) specimens are not feasible (Figure S5.2, Appendix III). To make the density distribution more visually appealing: 2D color maps of densities and void content are presented for 38 specimens for N(II) and NT(II) (Figure 5.5).

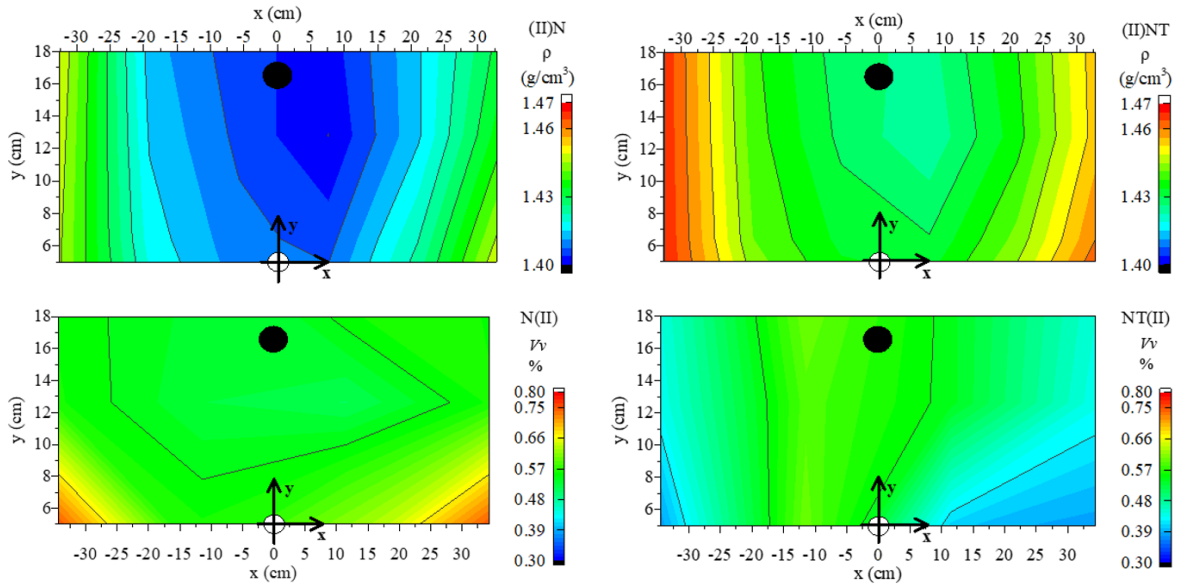

Figure 5.5 Color maps for density (ρ) and void volume fraction ($\overline{V_v}$ (%)) for N(II), and NT(II) plates.

For both N(II), and NT(II), ρ is the lowest between the inlet port and the outlet, within the red dashed circle, and increase gradually in circular steps toward the corners. However, for V_v in N(II) are almost homogenously distributed through the plate, but for NT(II) plate V_v are not homogenous and are higher within the dashed red circle. In the corners of N(II) plate, the resin flow trapes higher amount of air, therefore increase V_v compared to the region within the red dashed circle, while in NT(II) plate, HNTs seems to have percipitated in these voids (closer to the corners) which explain the decrease in V_v of the plate.

5.3.2 Effect of RTM method on mechanical properties

The preform has to be sufficiently wetted by the resin (i.e., the resin sufficiently fills the volume between the fiber and inside them), in order for the cured plate to have high mechanical performance. To determine which RTM mold produce better composites, plates

with the same composition from both RTMs are compared together. N(II) is compared to N(I), and NT(II) is compared to NT(I) (Table 5.3). RTM(II) increases $\overline{V_v}$ in neat CFRP composite by 22%, and when comparing $\bar{E}_{\text{flex.}}$, and $\bar{E}_{\text{shr.}}$, it is noticed that this increase in $\overline{V_v}$ barely changes $\bar{E}_{\text{flex.}}$ but improves $\bar{E}_{\text{shr.}}$ for N(II) compared to N(I) by 12.3%. On the other hand, $\overline{V_v}$ for NT(II) decreased by 4% compared to NT(I), and both moduli ($\bar{E}_{\text{flex.}}$ and $\bar{E}_{\text{shr.}}$) decrease by ~ 12% compared to NT(I). RTM(II) gives better composites only for neat CFRP systems.

Table 5.3 average values of void volume fraction ($\overline{V_v}$), average flexural modulus ($\bar{E}_{\text{flex.}}$) and average in-plane shear modulus ($\bar{E}_{\text{shr.}}$) for N(I) compared to N(II) and for NT(I) compared to NT(II).

	N(I)	**N(II)**	**NT(I)**	**NT(II)**
$\overline{V_v}$ **(%)**	0.46 ∓ 0.11	0.56 ∓ 0.04	0.48 ∓ 0.04	0.46 ∓ 0.05
% change of (II) vs. (I)	+22 %		-4 %	
$\bar{E}$ **flex. (GPa)**	42.6 ∓ 1.8	42.9 ∓ 2.7	48.3 ∓ 0.8	42.2 ∓ 2.2
% change of (II) vs. (I)	+0.7 %		-12.6 %	
$\bar{E}$ **shr. (MPa)**	3178 ∓ 106	3568 ∓ 367	4067 ∓ 351	3587 ∓ 192
% change of (II) vs. (I)	+12.3 %		-11.8%	

To find out which RTM mold is more suitable when HNTs are added to the resin, flexural and in-plane shear properties for N(I) vs. NT(I), and for N(II) vs. NT(II), are compared in Table 5.4. NT(I) composite have better flexural and in-plane shear properties compared to N(I), while NT(I) composite properties has degraded compared to N(I). This shows that RTM(I) has a better design for producing CFRP/HNT composites.

Table 5.4 Average of flexural strength ($\bar{\sigma}_{Felx.}$), strain at maximum load ($\bar{\varepsilon}_{Flex.}$), and flexural modulus ($\bar{E}_{Flex.}$), and average of in-plane shear strength ($\bar{\sigma}_{Shr.}$), strain at maximum load ($\bar{\varepsilon}_{Shr.}$), and in-plane shear modulus ($\bar{E}_{Shr.}$) for N(I) vs. NT(I) and N(II) vs. NT(II)

	Flexural properties			**In-plan shear properties**		
% change of	$\bar{\sigma}$ **flex.** **(MPa)**	$\bar{\varepsilon}$ **flex.** **(%)**	$\bar{E}$ **flex.** **(MPa)**	$\bar{\sigma}$ **shr.** **(MPa)**	$\bar{\varepsilon}$ **shr.** **(%)**	$\bar{E}$ **shr.** **(MPa)**
NT(I) vs. N(I)*	+11.8%	+1.3%	+12.3%	+5.7%	+37.9%	+27.8%
NT(II) vs. N(II)	-1.83%	-4.30%	-0.07%	+6.77%	+0.56%	-7.76%

*****Experimental data are presented in detail in Chapter 4.

5.3.3 Flexural load resistance

The flexural stress-strain curves obtained from flexural tests for N(I), NT(I), N(II), and NT(II) composites are shown Figure 5.6. All the tested specimens gave similar responses and at the end of the test, all composites present stress drops before the final fracture. N(I) and NT(I) response to three-point bending loads are examined in detailed previously in Chapter 4 [25]. Mainly, The flexural modulus improves by 18.1% for NT(I) compared to N(I) and the stress drops, at higher load during the test, are attained over a broader strain interval for N(I) compared to NT(I) (Figure 5.6a). However, stress-strain curves for N(II), and NT(II) specimens overlap and there is no clear difference in the overall response to flexural stress in three-point bending after the addition of HNTs (Figure 5.6b).

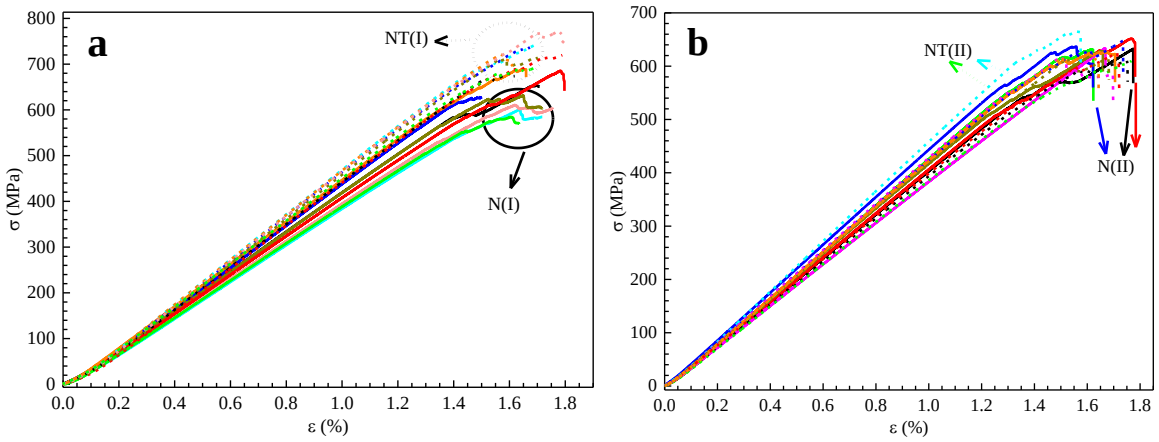

Figure 5.6 Three-point bending stress-strain curves for (a) N(I) and NT(I), and (b) N(II), NT(II) composites.

Knowing that the void content varies across the plates that are produced by RTM(II), it becomes needed to inspect smaller region within the plate plane. Some of the stress-strain curves that belongs to N(II), and NT(II) composite specimens, which have the same (x.y) coordinate on the composite plate, are overlaid in Figure 5.7 with s scheme of the composite plate showing the location of the tested specimens.

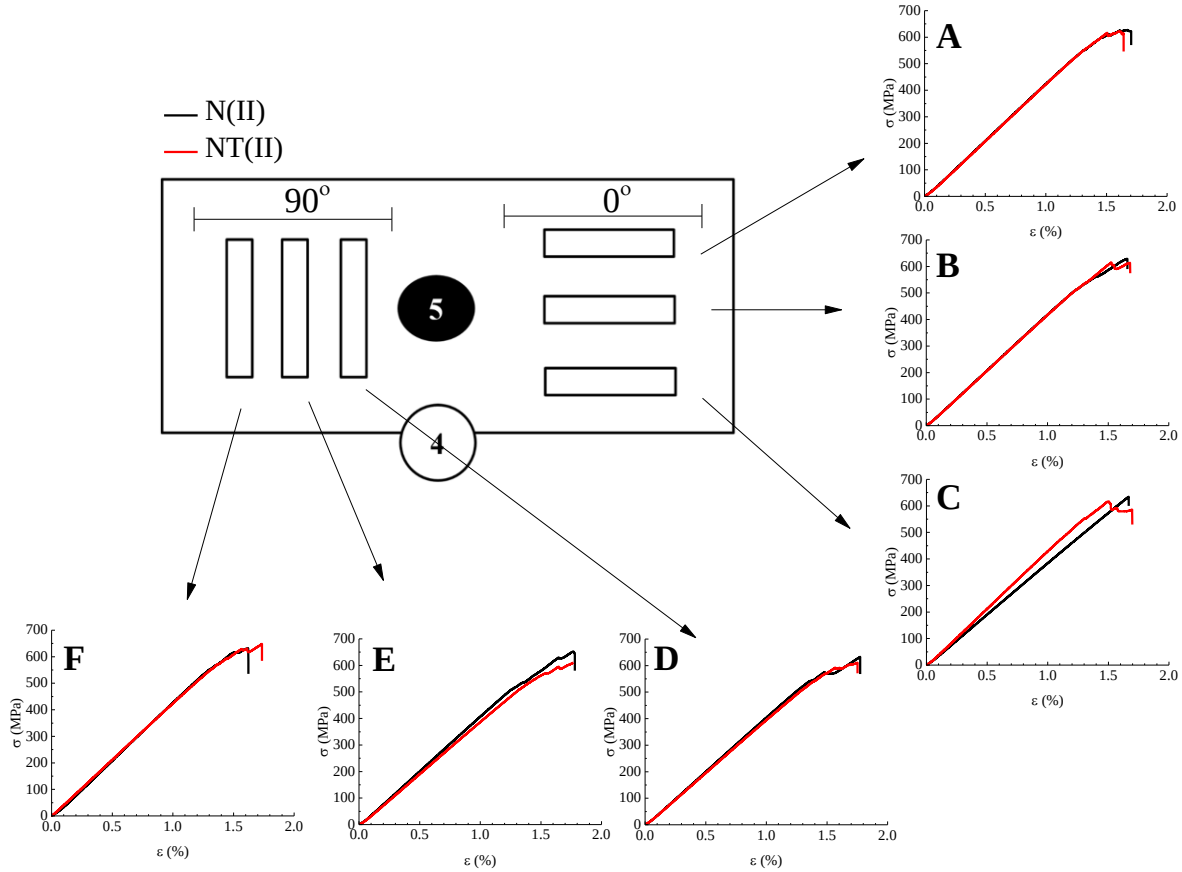

Figure 5.7 Scheme of plate made by RTM(II) with locations of specimens that are used for three-point bending tests with arrows showing stress-strain curves for N(II), NT(II) composites taken from the same exact location in the composite plate.

As it is seen in Figure 5.7, N(II) and NT(II) specimens that are closer to ports 4 and 5 have similar stress-strain curves, while specimens that are further away from the inlet and outlet ports, and closer to the corners of the plate (Figure 5.7C and F), shows that HNTs addition to the composite system results in some improvements in the specimens resistance to flexural stress. Figure S5.8 in appendix III shows a comparison between color maps for flexural modulus and V_v for both N(II), and NT(II) composite plates.

5.3.4 In-plane shear resistance

Figure 5.8 exhibits in-plane shear stress-strain curves of for N(I), NT(I), N(II), and NT(II) composite specimens. In all the groups tested the linear in-plane shear response ends at 1% strain, afterward the non-linear stress-strain behavior continues up to 21% strain. The damage accumulation and deformation mechanisms for N(I), NT(I) specimens are discussed in details in our previous work [25] and in Chapter 4. To recap, NT(I) specimens' in-plane

shear modulus and strength increased by 27.3 %, and 20.9% respectively, compared to N(I) (Figure 5.8a). On the other hand, stress-strain curves for N(II), and NT(II) specimens overlap and there is no clear difference in the composite response to in-plane shear after the addition of HNTs (Figure 5.8b). An inspection of smaller regions within the plate plane is presented in Figure 5.9.

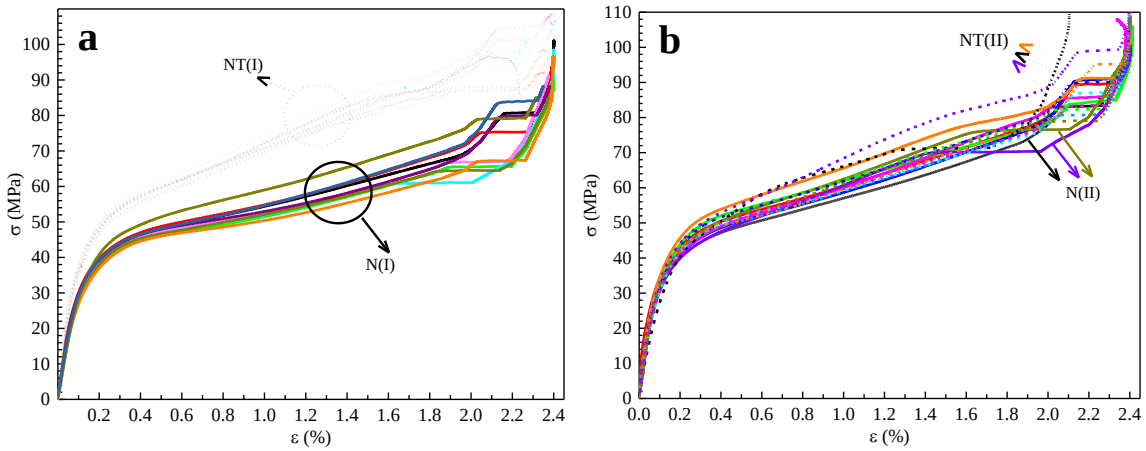

Figure 5.8 In plane shear stress-strain curves for (a) N(I) and NT(I), and (b) N(II), NT(II) composites.

The distribution of V_v in RTM(II) plates and the precipitation of HNTs in the corners, affects the specimen behavior under in-plane shear in a opposite way compared to three-point bending test. Figure 5.9 show N(II) and NT(II) specimens that are closer to corners of the plate (Figure 5.9C and G) has less resistance to in-plane shear stress.

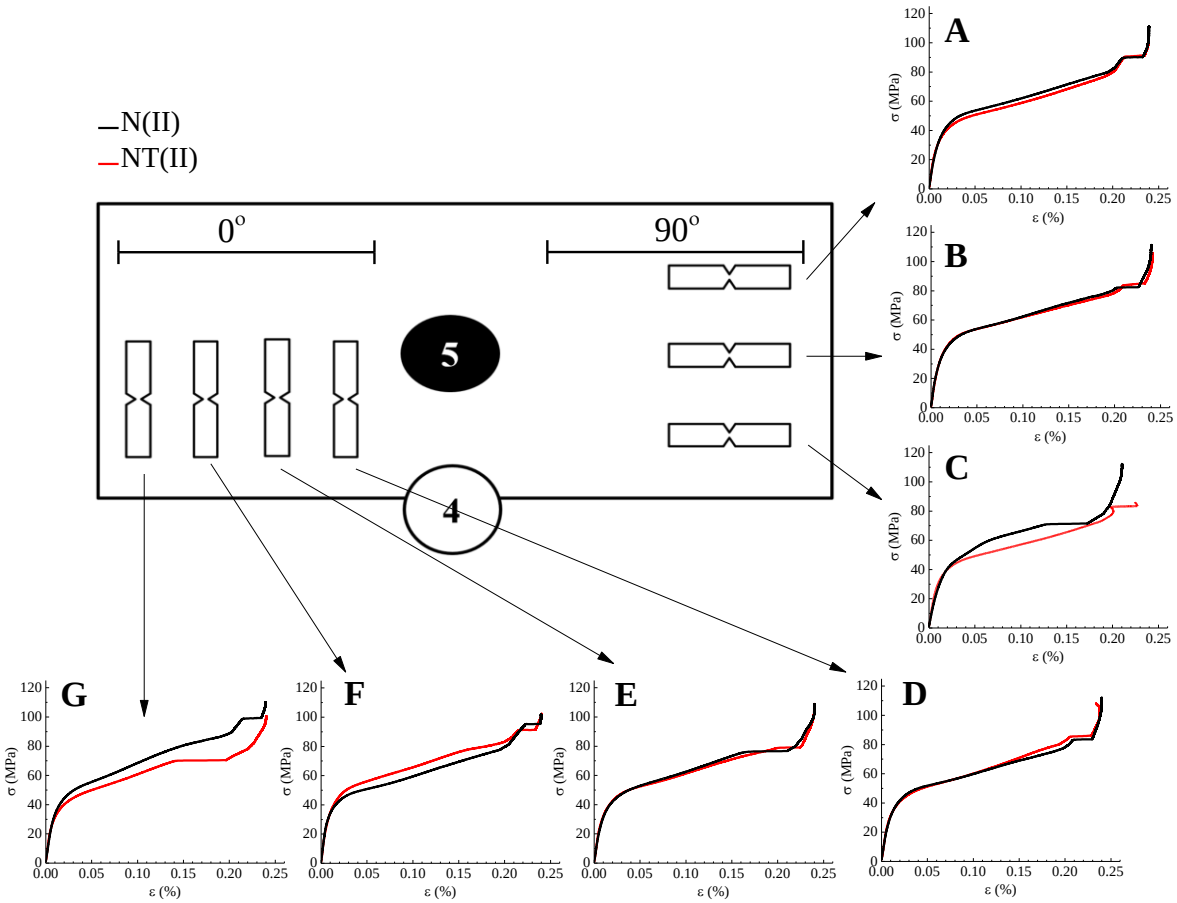

Figure 5.9 Scheme of plate made by RTM(II) with locations of specimens that are used for In-plane shear tests with arrows showing stress-strain curves for N(II), NT(II) composites taken from the same exact location in the composite plate.

5.4. Conclusions

Two RTM molds are used to manufacture CFRP and CFRP/HNT composite plates. RTM(I) have a linear resin flow front while RTM(II) have a curved one. Composite plates manufactured by both RTMs (with and without HNTs) where compared with regards to void content, flexural (i.e., obtained by three-point bending test) and in-plane shear properties. Overall, composite plate that are produces by RTM(II) have a higher $\overline{V_v}$ relative to RTM(I) plates. The mechanical properties of the composites, improves by adding HNT only by using RTM(I). Even though the linear flow path in RTM(I) leads to gradual increase in particle participation alongside the mold, modulus of flexural and in-plane shear properties increased with the addition of HNTs by 12.3%, and +27.8%, respectively. The rectangular RTM(II) mold with centered outlet port creates more void in the CFRP composite plate around the corners of the plate, and HNTs filtrate through the CFs perform largely in those area away

from the inlet and outlet ports. RTM(II) produces un-homogenous distribution of CFFR/HNT plates, where the performance of composites shows no general improvement if not degrading in the flexural and in-plane shear properties after the incorporation of HNTs.

CHAPTER 6. CONCLUSIONS

In this thesis, a comprehensive study was conducted to understand the effect of HNTs on the curing kinetics of epoxy polymer when it is cured by amine-based hardener. Based on extensive DSC and rheological experiments, KS model-based analysis was applied and the constants affecting the curing kinetics were calculated. The formation of bonds during the polymerization process was accelerated and decelerated with combination of factors and as a function of HNTs weight fraction in the system. At 2 wt.% longer chains formed prior to the gelation point, whereas at 5 wt.% more cross linking took place. Moreover, the deformation mechanism of epoxy nanocomposites under static and dynamic flexural loads were investigated and 10 wt.% of HNTs improved flexural modulus by 35.5%. The integration of HNTs improved the mechanical performance of the nanocomposites with no effect on the T_g of the resin. Afterward, the manufacturing process of a wide range of concentration of epoxy/HNT nanocomposites was explored. Alkaline modification of HNT surface showed no noticeable improvement in the mechanical properties compared to the improvement that were already achieved by using pristine HNTs. Conductivity spectra of epoxy/HNT showed that 10 wt.% of HNTs gives epoxy an ionic conductivity that is comparable to the ionic conductivity of epoxy with 1 wt.% of IL/$LiClO_4$. This means that epoxy/HNT nanocomposites are feasible system to be developed further for structural capacitor applications.

Aiming at investigating the epoxy/HNT as a matrix in CFRP composites, CFRP and CFRP/HNT laminates were successfully manufactured by RTM method. Upon adding 10 wt.% of HNT to the epoxy resin, the flexural- and in-plane shear moduli have improved by 18.1% and 27.3%, respectively. HNTs primarily affected matrix cracking and delamination mechanisms and altered the damage accumulation mechanism to become less severe and more gradual with smaller steps. Non-destructive health monitoring techniques and numerical analysis using Peridynamic supported the experimental data that we found. HNTs hindered crack growth, crack tip splitting and in turn crack coalescence in CFRP/HNT specimens.

In last part of the thesis we studied the effect of the infusion path on the void content and HNTs infiltration through the fibers. Two RTM molds were used to manufacture CFRP

and CFRP/HNT composite plates. Both molds were plain and rectangular shapes, but they differ in the placement of inlet and outlet ports, thus the front flow path of the resin through the preform will be different between the two RTMs. RTM(I) had a linear front flow, while RTM(II) had a curved flow. Linear flow path led to gradual increase in particle participation alongside the mold, where the curved front flow caused HNTs participations to be higher in the corners of the mold more than closer to the center of the plate. *Vv* and HNTs content in CFRP/HNT plates made by RTM(I) improved flexural and in-plane shear properties significantly compared to CFRP plates. Contrary to RTM(I), adding HNTs to the resin produced plates with inhomogeneous distribution of *Vv* and HNT participation, and the mechanical properties of CFRP/HNT degraded in comparison of CFRP plate by RTM(II). Overall, for manufacturing neat CFRP composites, RTM(II) plates contained 22% extra *Vv* compared to RTM(I) plates, and in-plane shear modules of RTM(II) plates were higher by 12% compared to RTM(I) composites. However, when adding HNTs to the composite, RTM(II) have 6% less *Vv* and lower moduli compared to CFRP/HNT plates from RTM(I). Linear front flow path in RTM(I) was more advantageous in terms of yielding smaller particle distribution non-homogeneity in the composite. In RTM(II), the center gate design has increases the non-homogeneity in the composite compared to RTM(I). Filtration of the nanotubes throughout the plate was inhomogeneous and affected the flexural and in-plane shear moduli negatively. To understand the mechanism of how HNTs improved in-plane shear properties in CFRP/HNT from RTM(I), health monitoring techniques showed HNTs facilitates the formation of a pure shear region in the area between the notches. For CFRP/HNT made by RTM(II), the decrease in *Vv* and the variation in HNTs deposition throughout the plate, obstructed this deformation mechanism and the average value of in-plane shear modulus were smaller compared to CFRP/HNT made by RTM(I).

REFERENCES

1. Voronin, D.V., et al., *Clay Composites for Thermal Energy Storage: A Review.* Molecules, 2020. **25**(7).
2. Downey, M.A. and L.T. Drzal, *Toughening of aromatic epoxy via aliphatic epoxy copolymers.* Polymer, 2014. **55**(26): p. 6658-6663.
3. Frankowiak, J.C., R.H. Bello, and L.A.F. Coelho, *Oxidation time effects of multiwalled carbon nanotubes on thermal, mechanical, and cure kinetics of epoxy-based nanocomposites.* Polym. Compos., 2020. **41**(10): p. 3966-3984.
4. Xu, Y., et al., *Thermal behavior and kinetics study of carbon/epoxy resin composites.* Polym. Compos., 2019. **40**(12): p. 4530-4546.
5. Zhang, J., et al., *Role of rigid nanoparticles and CTBN rubber in the toughening of epoxies with different cross-linking densities.* Compo. Part A Appl. Sci. Manuf., 2016. **80**: p. 82-94.
6. Bakar, M., et al., *Synergistic effects of thermoplastic and nanoclay on the performance properties and morphology of epoxy resin.* Polym. Compos., 2018. **39**(S4): p. E2540-E2551.
7. Gholinezhad, F., R. Golhosseini, and O. Moini Jazani, *Non-isothermal DSC curing kinetics study of silicone-modified epoxy/ABS/GO nanocomposite.* Polym. Compos., 2022. **43**(6): p. 3794-3808.
8. Liu, Y., et al., *Selective dispersion of silver nanowires in epoxy/polyetherimide binary composites with enhanced electrical conductivity: a study of curing kinetics and morphology.* Polym. Compos., 2019. **40**(11): p. 4390-4401.
9. Mphahlele, K., S. Ray, and A. Kolesnikov, *Cure Kinetics, Morphology Development, and Rheology of a High-Performance Carbon-Fiber-Reinforced Epoxy Composite.* Compos. B: Eng., 2019. **176**.
10. Cizmecioglu, M., A. Gupta, and R. Fedors, *Influence of cure conditions on glass transition temperature and density of an epoxy resin.* J. Appl. Polym. Sci., 1986. **32**(8): p. 6177-6190.
11. Barghamadi, M. and H. Behmadi, *Influence of the epoxy functionalization of multiwall carbon nanotubes on the nonisothermal cure kinetics and thermal properties of epoxy/multiwall carbon nanotube nanocomposites.* Polym. Compos., 2012. **33**(7): p. 1085-1093.
12. Rahaman, A. and A. Mohanty, *Effect of carbon nanotubes on the curing and thermomechanical behavior of epoxy/carbon nanotubes composites.* Polym. Compos., 2014. **35**(3): p. 441-449.
13. Zhao, L. and X. Hu, *Autocatalytic Curing Kinetics of Thermosetting Polymers: A New Model Based on Temperature Dependent Reaction Orders.* Polymer, 2010. **51**(16): p. 3814-3820.

14. Sourour, S. and M.R. Kamal, *Differential Scanning Calorimetry of Epoxy Cure: Isothermal Cure Kinetics.* Thermochim. Acta, 1976. **14**: p. 41-59.

15. Kamal, M.R. and S. Sourour, *Kinetics and thermal characterization of thermoset cure*. **Polym. Eng. Sci.**, 1973. **13**(1): p. 59-64.

16. Rabearison, N., C. Jochum, and J.C. Grandidier, *A Cure Kinetics, Diffusion Controlled and Temperature Dependent, Identification of the Araldite LY556 Epoxy.* J. Mater. Sci., 2010. **46**(3): p. 787-796.

17. Kamran-Pirzaman, A., Y. Rostamian, and S. Babatabar, *Surface improvement effect of silica nanoparticles on epoxy nanocomposites mechanical and physical properties, and curing kinetic.* J. Polym. Res., 2020. **27**.

18. Tcherbi-Narteh, A., M. Hosur, and S. Jeelani, *Effects of Different Montmorillonite Nanoclay Loading on Cure Behavior and Properties of Diglycidyl Ether of Bisphenol A Epoxy.* J. Nanomater., 2016. **2016**: p. 3840348.

19. Ma, X.Q., et al., *Interlaminar properties of carbon fiber composite laminates with resin transfer molding/prepreg co-curing process.* J. Reinf. Plast. Compos., 2014. **33**(24): p. 2228-2241.

20. Han, S. and D.D.L. Chung, *Strengthening and stiffening carbon fiber epoxy composites by halloysite nanotubes, carbon nanotubes and silicon carbide whiskers.* Appl. Clay Sci., 2013. **83-84**: p. 375-382.

21. Ulus, H., et al., *Halloysite nanotube reinforcement endows ameliorated fracture resistance of seawater aged basalt/epoxy composites.* J. Compos. Mater., 2020. **54**(20): p. 2761-2779.

22. Jelic, A., et al., *Design of halloysite modification for improvement of mechanical properties of the epoxy based nanocomposites.* Polym. Compos., 2021. **42**(5): p. 2180-2192.

23. Zhao, X.L., et al., *Preparation of HNTs-d-GO hybrid nanoparticles for gallic acid epoxy composites with improved thermal and mechanical properties.* Polym. Compos., 2022. **43**(8): p. 5133-5144.

24. Ye, Y.C., H.; Wu, J.; Ye, L., *High impact strength epoxy nanocomposites with natural nanotubes.* Polymer, 2007. **48**(21): p. 6426-6433.

25. AlKhateab, B., et al., *Damage mechanisms in CFRP/HNT laminates under flexural and in-plane shear loadings using experimental and numerical methods.* Compo. Part A Appl. Sci. Manuf., 2020. **136**.

26. Akbari, V., et al., *Effect of Surface Treatment of Halloysite Nanotubes (HNTs) on the Kinetics of Epoxy Resin Cure with Amines.* Polymers (Basel), 2020. **12**(4).

27. Jouyandeh, M., et al., *Curing epoxy resin with anhydride in the presence of halloysite nanotubes: the contradictory effects of filler concentration.* Prog. Org. Coat., 2019. **126**: p. 129-135.

28. Cheng, C., et al., *Halloysite nanotubes in polymer science: purification, characterization, modification and applications.* Nanotechnol. Rev., 2020. **9**(1): p. 323-344.

29. Ravichandran, G., et al., *Enhancement of mechanical properties of epoxy/halloysite nanotube (HNT) nanocomposites.* SN Appl. Sci., 2019. **1**(4).

30. Liu, M., et al., *Natural inorganic nanotubes reinforced epoxy resin nanocomposites.* J. Polym. Res., 2007. **15**(3): p. 205-212.

31. Nakamura, R., A.N. Netravali, and M.V. Hosur, *Effect of Halloysite Nanotube Incorporation in Epoxy Resin and Carbon Fiber Ethylene Ammonia Plasma Treatment on Their Interfacial Property.* J. Adhes. Sci Technol., 2012. **26**: p. 1295–1312.

32. Ramamoorthi, P. and P.S. Sampath, *Experimental Investigations of Influence of Halloysite Nanotube on Mechanical and Chemical Resistance Properties of Glass Fiber Reinforced Epoxy Nano Composites.* J. Sci. Ind. Res., 2015. **74**: p. 685-689.

33. Ye, Y.P., et al., *Interlaminar properties of carbon fiber composites with halloysite nanotube-toughened epoxy matrix.* Compos. Sci. Technol., 2011. **71**(5): p. 717-723.

34. Yuan, P., D. Tan, and F. Annabi-Bergaya, *Properties and applications of halloysite nanotubes: recent research advances and future prospects.* Appl. Clay Sci., 2015. **112-113**: p. 75-93.

35. Sprenger, S., *Nanosilica-Toughened Epoxy Resins.* Polymers (Basel), 2020. **12**(8).

36. Yuan, P., et al., *Functionalization of Halloysite Clay Nanotubes by Grafting with γ-Aminopropyltriethoxysilane.* J. Phys. Chem. C, 2008. **112**(40): p. 15742–15751.

37. Dittanet, P. and R.A. Pearson, *Effect of silica nanoparticle size on toughening mechanisms of filled epoxy.* Polymer, 2012. **53**(9): p. 1890-1905.

38. Sun, P., et al., *Simultaneous improvement in strength, toughness, and thermal stability of epoxy/halloysite nanotubes composites by interfacial modification.* J. Appl. Polym. Sci., 2016. **133**(13).

39. Abbasi, S., *Purification, size separation and ionic fnctionalization of halloysite nanotubes*, in *Graduate School of Engineering and Natural Sciences*. 2018, Sabanci University.

40. Sun, Y., et al., *Glass transition and relaxation behavior of epoxy nanocomposites.* J. Polym. Sci. B Polym. Phys., 2004. **42**(21): p. 3849-3858.

41. Chatterjee, K.K., *Uses of Industrial Minerals, Rocks and Freshwater*. 2009, New York: Nova Science Publishers, Inc.

42. Bilyeu, B., W. Brostow, and K.P. Menard, *Epoxy Thermosets and Their Applications III . Kinetic Equations and Models.* J. Mater. Educ., 2001. **23**: p. 189-204.

43. Rozenberg, B.A., *Kinetics Thermodynamics and Mechanism of Reactions of Epoxy Oligomers with Amines*, in *Epoxy Resins and Composites II, Advances in Polymer Science*. 1986, Springer: Berlin, Heidelberg. p. 113-165.

44. Karayannidou, E.G., D.S. Achilias, and I.D. Sideridou, *Cure Kinetics of Epoxy–Amine Resins Used in the Restoration of Works of Art From Glass or Ceramic.* Eur. Polym. J., 2006. **42**(12): p. 3311-3323.

45. Dai, J.Y., et al., *Synthesis of Biobased Benzoxazines Suitable for Vacuum-Assisted Resin Transfer Molding Process via Introduction of Soft Silicon Segment.* Ind. Eng. Chem. Res., 2018. **57**(8): p. 3091-3102.

46. Greenhalgh, E.S., *Delamination-dominated failures in polymer composites*, in *Failure Analysis and Fractography of Polymer Composites*. 2009, CRC Press LLC. p. 164-237.

47. Zeng, S., et al., *Facile hydroxylation of halloysite nanotubes for epoxy nanocomposite applications.* Polymer, 2014. **55**(25): p. 6519-6528.

48. AlKhateab, B., et al., *Aspects of Halloysite Nanotubes Integration in Epoxy Nanocomposites; Curing kinetics and Deformation Mechanism.* Polym. Compos., 2022.

49. González, C., et al., *Structural composites for multifunctional applications: Current challenges and future trends.* Prog. Mater. Sci., 2017. **89**: p. 194-251.

50. Zhou, W., et al., *Failure behavior and damage visualization of thick carbon/aramid hybrid woven composites under flexural loading conditions.* Nondestruct. Test. Eval., 2019. **35**(2): p. 139-157.

51. Zanjani, J., et al., *Design and fabrication of multi-walled hollow nanofibers by triaxial electrospinning as reinforcing agents in nanocomposites.* J. Reinf. Plast. Compos., 2015. **34**: p. 1273-1286.

52. Zanjani, J., et al., *Nano-engineered design and manufacturing of high-performance epoxy matrix composites with carbon fiber/selectively integrated graphene as multi-scale reinforcements.* RSC Advances, 2016. **6**(12): p. 9495-9506.

53. Zanjani, J.S.M., et al., *Tailoring viscoelastic response, self-heating and deicing properties of carbon-fiber reinforced epoxy composites by graphene modification.* Compo. Part A Appl. Sci. Manuf., 2018. **106**: p. 1-10.

54. Tiwari, S. and J. Bijwe, *Surface Treatment of Carbon Fibers - A Review.* Procedia Technology, 2014. **14**: p. 505-512.

55. Sánchez, M., et al., *Effect of the carbon nanotube functionalization on flexural properties of multiscale carbon fiber/epoxy composites manufactured by VARIM.* Compos. B: Eng., 2013. **45**(1): p. 1613-1619.

56. Gonzalez-Montiel, A.M.-B., S.; Barrientos-Ramirez, S.; Flores-Santos, L.; Montes de Oca-Ramirez, G., *Mechanical Reinforcement of Epoxy Resins using Magnetic Aligned Halloysite*, in *NSTI-Nanotech 2011*. 2011: United States.

57. Bozkurt, E., E. Kaya, and M. Tanoğlu, *Mechanical and thermal behavior of non-crimp glass fiber reinforced layered clay/epoxy nanocomposites.* Compos. Sci. Technol., 2007. **67**(15-16): p. 3394-3403.

58. Tessema, A., et al., *Effects of Nanoparticles on the Shear Properties of Polymer Composites*. 2015, Mechanical Engineering Department, University of South Carolina: South Carolina, USA.

59. Du, M., B. Guo, and D. Jia, *Thermal stability and flame retardant effects of halloysite nanotubes on poly(propylene).* Eur. Polym. J., 2006. **42**(6): p. 1362-1369.

60. Vijayan, P.P., Y.M.H. El-Gawady, and M.A.S.A. Al-Maadeed, *Halloysite Nanotube as Multifunctional Component in Epoxy Protective Coating.* Ind. Eng. Chem. Res., 2016. **55**(42): p. 11186-11192.

61. Dikshit, V., S. Bhudolia, and S. Joshi, *Multiscale Polymer Composites: A Review of the Interlaminar Fracture Toughness Improvement.* Fibers, 2017. **5**(4).

62. Xu, Y. and S.V. Hoa, *Mechanical properties of carbon fiber reinforced epoxy/clay nanocomposites.* Compos. Sci. Technol., 2008. **68**(3-4): p. 854-861.

63. Kornmann, X., et al., *Epoxy-layered silicate nanocomposites as matrix in glass fibre-reinforced composites.* Compos. Sci. Technol., 2005. **65**(14): p. 2259-2268.

64. Krushnamurty, K., et al., *Effect Of Nanoclay On The Toughness Of Epoxy And Mechanical, Impact Properties Of E-glass-epoxy Composites.* Advanced Materials Letters, 2015. **6**(8): p. 684-689.

65. Yang Y., C.Y., Leng F., Huang L., Wang Z., Tian W., *Recent Advances on Surface Modification of Halloysite Nanotubes for Multifunctional Applications.* Appl. Sci., 2017. **7**(12): p. 1215.

66. Tabrizi, I.E., et al., *Experimental and numerical investigation on fracture behavior of glass/carbon fiber hybrid composites using acoustic emission method and refined zigzag theory.* Compos. Struct., 2019. **223**.

67. Cho, J., et al., *Incorporation of Hydroxyethylcellulose-Functionalized Halloysite as a Means of Decreasing the Thermal Conductivity of Oilwell Cement.* Sci Rep, 2018. **8**(1): p. 16149.

68. Yilmaz, C., et al., *A hybrid damage assessment for E-and S-glass reinforced laminated composite structures under in-plane shear loading.* Compos. Struct., 2018. **186**: p. 347-354.

69. Akinyede, O., et al., *Investigation of particulate filtration of alumina nano-particles in VARTM processing of hybrid composites.* Proceedings of the Asme International Mechanical Engineering Congress and Exposition 2007, Vol 13, 2008: p. 157-162.

70. Yu, G., X. Gao, and Y. Song, *Experimental Investigation of the In-Plane Shear Behavior on Needled C/SiC Composites using Digital Image Correlation.* J. Ceram. Sci. Tech, 2016. **7**(4): p. 387-396.

71. Kalariya, Y. and S. Khedkar, *Applications of Digital Image Correlation Technique in Composite Research*, in *9th International Symposium on Advanced Science and Technology in Experimental Mechanics*. 2014: New Delhi, India.

72. Canal, L.P., et al., *Application of Digital Image Correlation at the Microscale in Fiber-Reinforced Composites.* Compo. Part A Appl. Sci. Manuf., 2012. **43**(10): p. 1630-1638.

73. Ali, H.Q., et al., *Microscopic analysis of failure in woven carbon fabric laminates coupled with digital image correlation and acoustic emission.* Compos. Struct., 2019. **230**.

74. Kefal, A., K.A. Hasim, and M. Yildiz, *A novel isogeometric beam element based on mixed form of refined zigzag theory for thick sandwich and multilayered composite beams.* Compos. Part B-Eng., 2019. **167**: p. 100-121.

75. Silling, S.A., *Reformulation of elasticity theory for discontinuities and long-range forces.* J. Mech. Phy. Solids, 2000. **48**(1): p. 175-209.

76. Madenci, E. and E. Oterkus, *Peridynamics for Isotropic Materials*. 2014. p. 53-74.

77. Hu, Y.L. and E. Madenci, *Bond-based peridynamic modeling of composite laminates with arbitrary fiber orientation and stacking sequence.* Compos. Struct., 2016. **153**: p. 139-175.

78. Kefal, A., et al., *Topology optimization of cracked structures using peridynamics.* Continuum Mech. Therm., 2019. **31**(6): p. 1645-1672.

79. Sohouli, A., et al., *Continuous density-based topology optimization of cracked structures using peridynamics.* Structural and Multidisciplinary Optimization, 2020.

80. Rahimi, M.N., et al., *An Ordinary State-Based Peridynamic Model for Toughness Enhancement of Brittle Materials through Drilling Stop-Holes (under review).* Int. J. Mech. Sci., 2020.

81. Yilmaz, C., et al., *A hybrid damage assessment for E-and S-glass reinforced laminated composite structures under in-plane shear loading.* Compos. Struct., 2018. **186**: p. 347–354.

82. Kovvali, N., *Theory and Applications of Gaussian Quadrature Methods*. Synthesis Lectures on Algorithms and Software in Engineering, ed. A. Spanias. Vol. 3. 2011: Morgan & Claypool Publishers. 1-65.

83. Madenci, E. and E. Oterkus, *Peridynamic Theory and Its Applications*. 2014: Springer, New York, NY.

84. Oterkus, E., et al., *Combined finite element and peridynamic analyses for predicting failure in a stiffened composite curved panel with a central slot.* Compos. Struct., 2012. **94**(3): p. 839-850.

85. Silling, S.A. and E. Askari, *A meshfree method based on the peridynamic model of solid mechanics.* Comput. Struct., 2005. **83**(17-18): p. 1526-1535.

86. Sánchez, M., et al., *Effect of the carbon nanotube functionalization on flexural properties of multiscale carbon fiber/epoxy composites manufactured by VARIM.* Compos. Part B-Eng., 2013. **45**(1): p. 1613-1619.

87. Gutkin, R., et al., *On acoustic emission for failure investigation in CFRP: Pattern recognition and peak frequency analyses.* Mech. Sys. Signal Pr., 2011. **25**(4): p. 1393-1407.

88. Gill, A.F., P. Robinson, and S. Pinho, *Effect of variation in fibre volume fraction on modes I and II delamination behaviour of 5HS woven composites manufactured by RTM.* Compos. Sci. Technol., 2009. **69**(14): p. 2368-2375.

89. Pan, L., et al., *Enhanced mechanical and thermal properties of epoxy with hyperbranched polyester grafted perylene diimide.* RSC Adv., 2015. **5**(5): p. 3177-3186.

90. Srivastava, S. and A. Pandey, *Mechanical behavior and thermal stability of ultrasonically synthesized halloysite-epoxy composite.* Compos. Commun., 2019. **11**: p. 39-44.

91. Purslow, D., *Matrix fractography of fiber reinforced epoxy composites.* Composites 1986. **17**(4).

92. Ali, H.Q., et al., *Microscopic analysis of failure in woven carbon fabric laminates coupled with digital image correlation and acoustic emission.* Compos. Struct., 2019. **230**: p. 111515.

93. Deng, S., et al., *Toughening epoxies with halloysite nanotubes.* Polymer, 2008. **49**(23): p. 5119-5127.

94. Dalai, R. and B.C. Ray, *Failure and Fractography Studies of FRP Composites: Effects of Loading Speed and Environments*, in *Processing and Fabrication of Advanced Materials XIX*. 2011: New Zealand.

95. Fernández, C., et al., *The effect of multiwall carbon nanotubes on the in-plane shear behavior of epoxy glass fiber reinforced composites.* Compos. Part B-Eng., 2013. **55**: p. 421-425.

96. Chandrasekaran, V.C.S., S.G. Advani, and M.H. Santare, *Influence of resin properties on interlaminar shear strength of glass/epoxy/MWNT hybrid composites.* Compos. Part A-Appl. Sci. Manuf., 2011. **42**(8): p. 1007-1016.

97. Taheri-Behrooz, F., M. Esmkhani, and A. Yaghoobi-Chatroodi, *Effect of testing procedure on the in-plane shear properties of CNF/glass/epoxy composites.* Polym. Polym. Compos., 2019: p. 0967391119867200.

98. Hansen, U., *Damage development in woven fabric composites during tension-tension fatigue.* J. Compos. Mater., 1999. **33**(7): p. 614-639.

99. Massarwa, E., I.E. Tabrizi, and M. Yildiz, *Numerical Prediction and Experimental Validation of the Mechanical Response and Failure Behavior of Glass/Carbon Fiber Hybrid Composites under Various Loading Conditions.* Mech. Mater., 2020.

100. Okan, B., et al., *Morphology-controllable synthesis and characterization of carbon nanotube/polypyrrole composites and their hydrogen storage capacities*. Vol. 167. 2015. 171–180.

101. Brocks, T., et al., *Experimental RTM Manufacturing Analysis of Carbon/Epoxy Composites for Aerospace Application: Non-crimp and Woven Fabric Differences.* Materials Research-Ibero-American Journal of Materials, 2013. **16**(5): p. 1175-1182.

102. Sas, H.S. and M. Erdal, *Modeling of particle–resin suspension impregnation in compression resin transfer molding of particle-filled, continuous fiber reinforced composites.* Heat Mass Transf., 2014. **50**(3): p. 397-414.

103. Kocaman, E.S., et al., *Monitoring the Damage State of Fiber Reinforced Composites Using an FBG Network for Failure Prediction.* Materials (Basel), 2017. **10**(1).

104. Babu, B.J.C., R.T.D. Prabhakaran, and V.P. Agrawal, *Quality Evaluation of Resin Transfer Molded Products.* J. Reinf. Plast. Compos., 2008. **27**(6): p. 559-581.

105. Fracassi, F.T. and M.V. Donadon, *Simulation of vacuum assisted resin transfer molding process through dynamic system analysis.* J. Compos. Mater., 2018. **52**(27): p. 3759-3771.

106. Ma, K.M., et al., *Plasma treatment of carbon fibers: Non-equilibrium dynamic adsorption and its effect on the mechanical properties of RTM fabricated composites.* Appl. Surf. Sci., 2011. **257**(9): p. 3824-3830.

107. Zarandi, M.A.F., S. Arroyo, and K.M. Pillai, *Longitudinal and transverse flows in fiber tows: Evaluation of theoretical permeability models through numerical predictions and experimental measurements.* Compo. Part A Appl. Sci. Manuf., 2019. **119**: p. 73-87.

108. Nordlund, M., S.P. Fernberg, and T.S. Lundström, *Particle deposition mechanisms during processing of advanced composite materials.* Compo. Part A Appl. Sci. Manuf., 2007. **38**(10): p. 2182-2193.

109. Lefevre, D., et al., *Modelling the flow of particle-filled resin through a fibrous preform in liquid composite molding technologies.* Compo. Part A Appl. Sci. Manuf., 2007. **38**(10): p. 2154-2163.

110. Erdal, M., S.I. Güçeri, and S.C. Danforth, *Impregnation Molding of Particle-Filled Preceramic Polymers: process modeling.* J. Am. Ceram. Soc., 1999. **82**(8).

APPENDIX I

I.1. Structural characterization of HNTs

Table S2.1 Theoretical and experimental physical properties of HNTs.

	Surface area (BET) m^2/g	Density (Pycnometer) g/cm^3	Moisture	Particle size, d_{90} (μm)
Theo.	128.38	1.8-2.6	5.43%	5.01
Exp.	66.17	2.3	5.30 %	2

I.2. Mechanical Properties of epoxy/HNT nanocomposites

Table S2.2 Average flexural yielding strength (0.2%) of three specimens for epoxy and epoxy/HNT nanocomposites.

Neat	**0.5 wt.%**	**1 wt.%**	**2 wt.%**	**5 wt.%**	**10 wt.%**
85.1 ± 8.29	95.5 ± 1.64	97.8 ± 0.89	80.4 ± 2.89	94.6 ± 0.58	96.5 ± 0.91

I.3. Curing Kinetics of epoxy/HNT nanocomposites

Table S2.3 model summary of the coefficient of determination (R^2), sum of deviation squares, and mean residual.

Method/Model	R^2	Sum of dev. squares	Mean Res.
Friedman	0.999	0.059	0.004
OFW	0.912	4.736	0.037
KAS	0.977	1.294	0.020

KFM; Friedman method

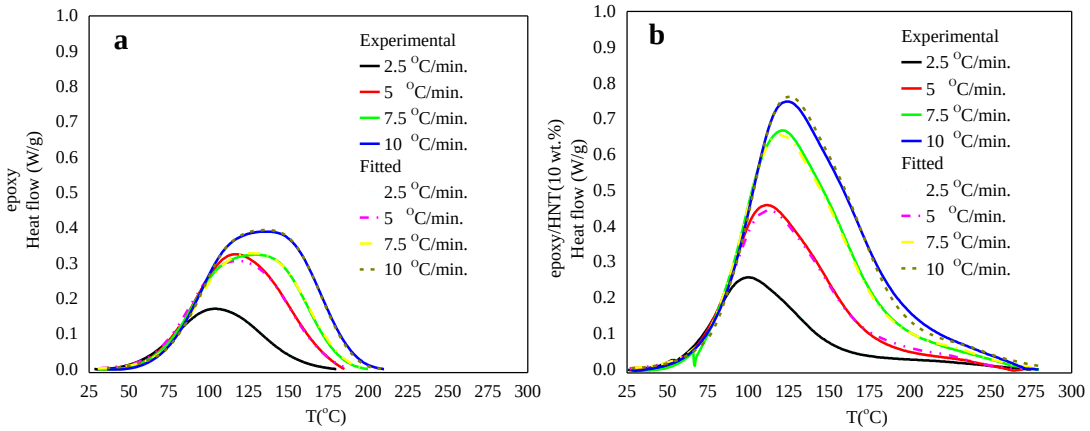

Figure S2.1 Experimental data obtained from DSC measurements and the fitted data using Friedman method supplied by Netzsch Neo software for (a) epoxy, and (b) epoxy/HNT(10 wt.%).

Epoxy and epoxy/HNT (10 wt.%) conversion curves

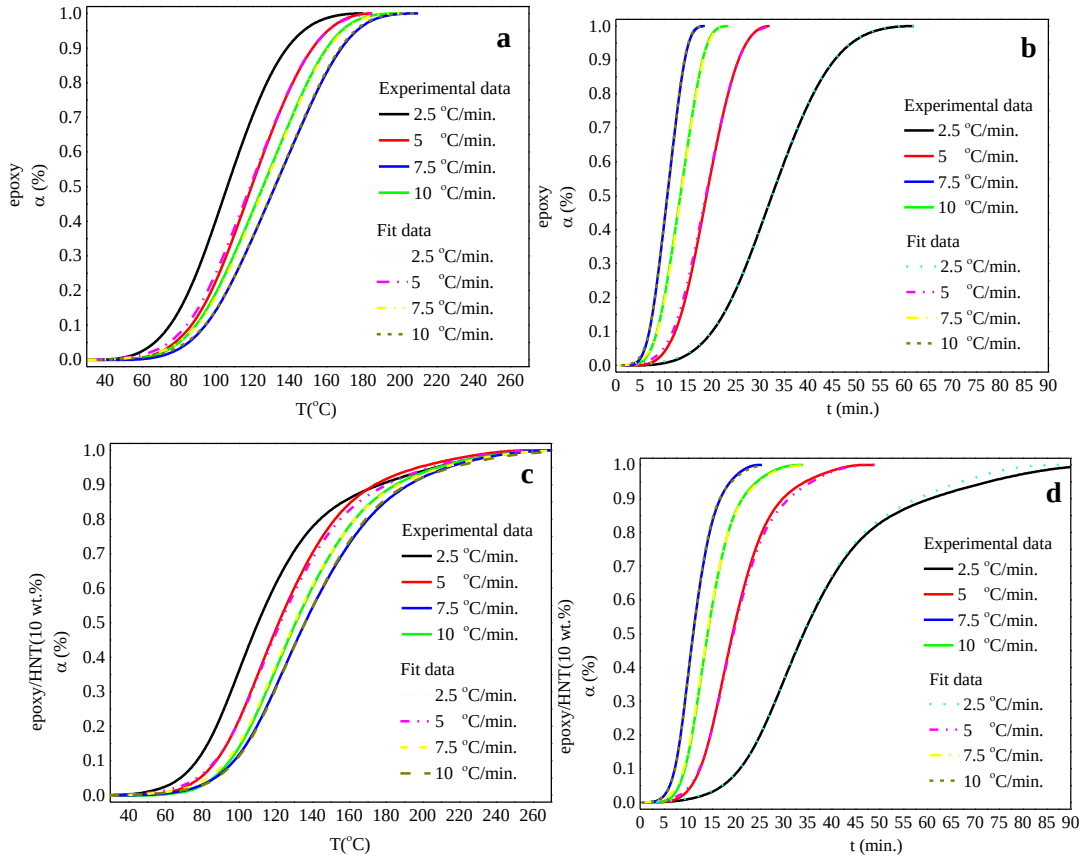

Figure S2.2 Experimental and fitted data of (a) conversion vs. temperature for epoxy, (b) conversion vs. time for epoxy, (c) conversion vs. temperature for epoxy/HNT(10 wt.%), (d) conversion vs. time for epoxy/HNT(10 wt.%).

Epoxy and epoxy/HNT (10 wt.%) conversion rate

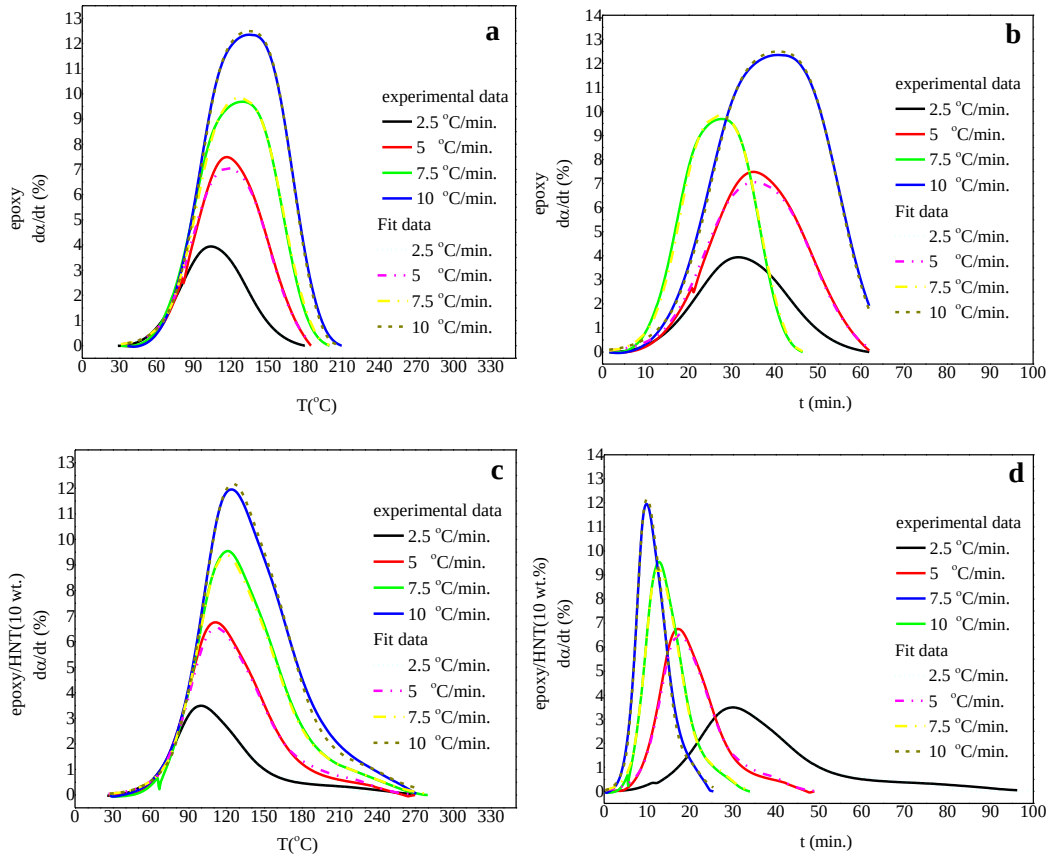

Figure S2.3 Experimental and fitted data of (a) rate of conversion vs. temperature for epoxy, (b) rate of conversion vs. time for epoxy, (c) rate of conversion vs. temperature for epoxy/HNT(10 wt.%), (d) rate of conversion vs. time for epoxy/HNT(10 wt.%).

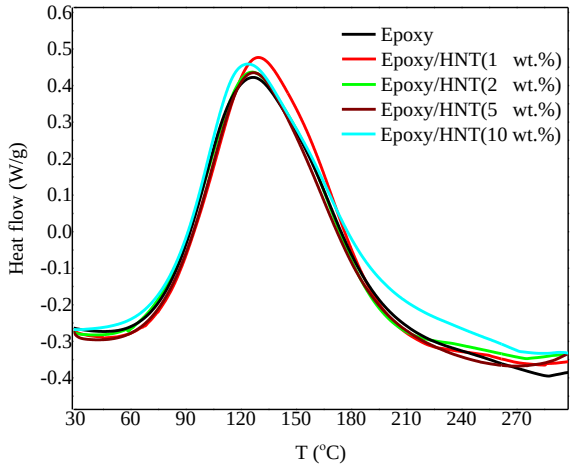

Figure S2.4 DSC graphs of epoxy/HNT nanocomposites with different weight ratios at a heating rate of 10 °C/min.

Table S2.4 Activation energy (Ea_1), Log of the pre-exponential factor ($Log(A_1)$), reaction order (n), Log of the autocatalytic pre-exponential factor ($Log(A_2)$), autocatalytic power (m), activation energy 2 (Ea_2), area under curve, $Log(K_{diff})$, C_1, and C_2 for epoxy/HNT(0, 1, 2, 5, and 10 wt.%).

Without diffusion control											
wt.%	***Ea₁***	***Log (A₁)***	***n***	***Log (A₂)***	***m***	***Ea₂***				**Area**	***R²***
0	1889.02	-0.67	1.38	1.73	0.514	24.5				325.94	0.996
1	1901.24	-0.75	1.3	1.7	0.513	23.91				356.86	0.998
2	292.09	-0.42	1.29	1.35	0.507	23.63				334.72	0.997
5	1790.98	-0.66	1.51	1.71	0.537	24.28				358.22	0.999
10	1790.01	-0.54	1.87	1.65	0.559	24.54				390.5	0.998
With diffusion control											
wt.%	***Ea₁***	***Log (A₁)***	***n***	***Log (A₂)***	***m***	***Ea₂***	***Log (K_diff)***	***C₁***	***C₂***	**Area**	***R²***
0	1886.3	-0.67	1.38	1.73	0.514	24.51	-2.75	0.13	56.87	325.94	0.996
1	1893.7	-0.75	1.3	1.7	0.512	23.93	-4.05	0.13	56.53	356.87	0.998
2	196.6	-0.41	1.62	1.35	0.543	23.45	-7	3.58	75.3	360.96	0.998
5	1786.9	-0.66	1.51	1.71	0.537	24.28	2.66	14.87	93.78	358.22	0.999
10	1787.6	-0.54	1.87	1.65	0.56	24.54	-6.24	22.79	61.71	390.5	0.998

Rheological measurements

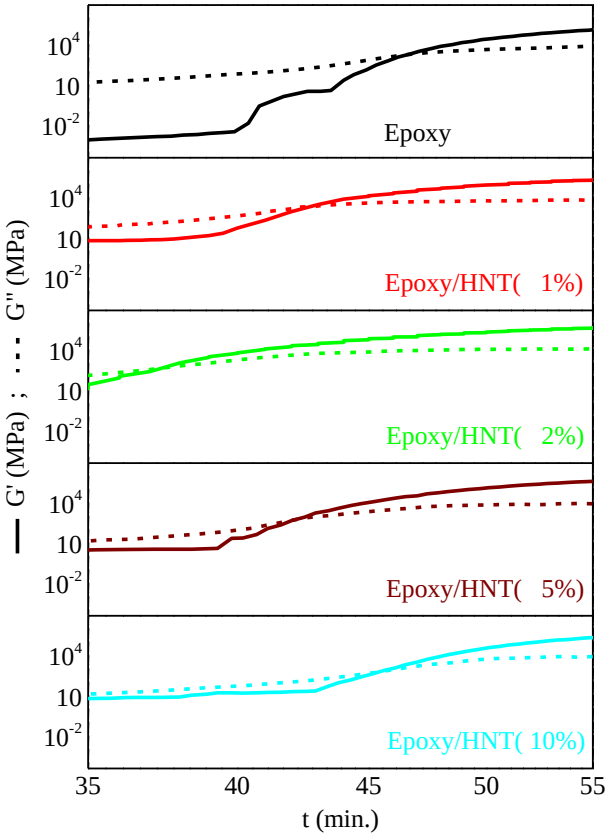

Figure S2.5 Superimposed graphs for storage shear modulus (G′), (b) loss shear modulus (G′′) for epoxy/HNT(0, 1, 2, 5, and 10 wt.%).

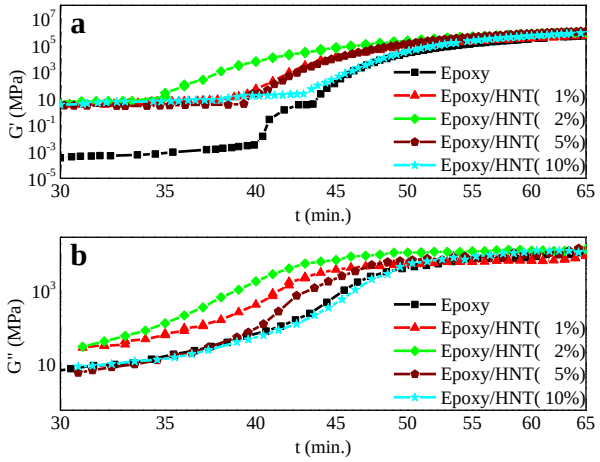

Figure S2.6 (a) storage shear modulus (G′), (b) loss shear modulus (G′′) for epoxy/HNT(0, 1, 2, 5, and 10 wt.%).

I.4. FTIR measurements of epoxy/HNT nanocomposites

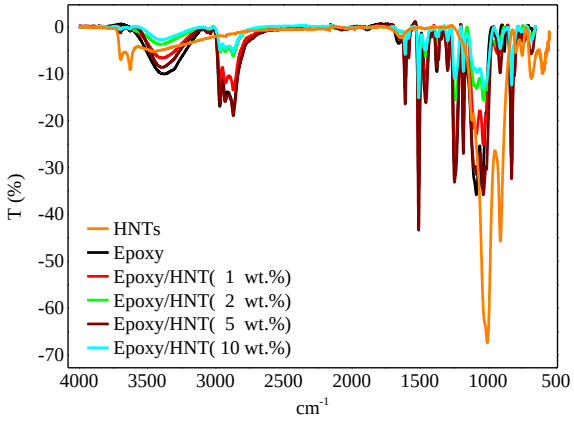

Figure S2.7 FTIR spectrums of HNTs and epoxy/HNT(0, 1, 2, 5, and 10 wt.%).

APPENDIX II

II.1. XRD

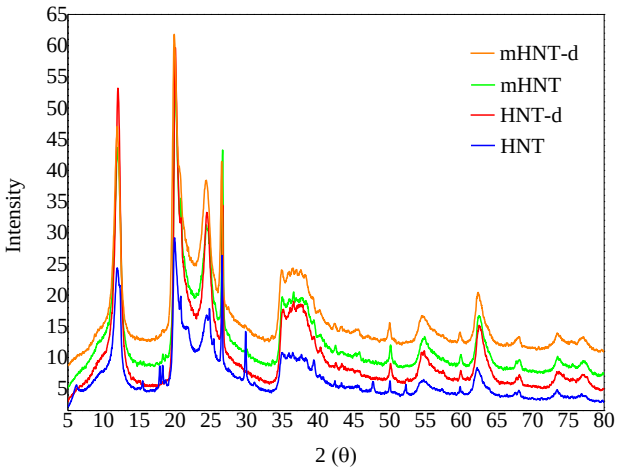

Figure S3.1 XRD of dried and hydrated HNTs (HNT and h-HNT), and dried and hydrated mHNTs (h-mHNT and mHNT).

II.2. FTIR

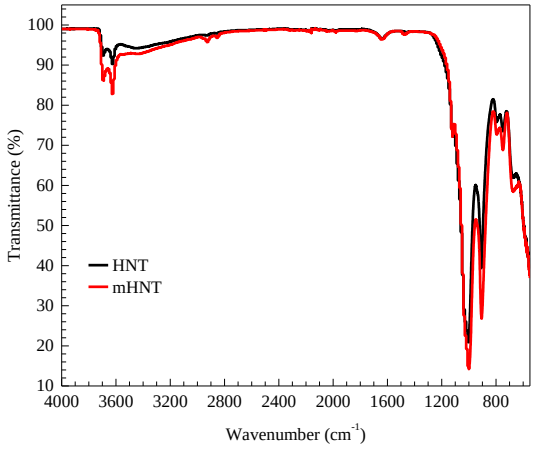

Figure S3.2 FTIR graphs for HNT vs. mHNT.

Table S3.1 FTIR characteristic peaks of HNTs and their assignments.

Peak (cm^{-1})	**Assignment**	**Peak (cm^{-1})**	**Assignment**
369	O-H stretching of inner-surface hydroxyl groups	1004	in-plane Si-O stretching
3625	O-H stretching of inner hydroxyl groups	909	O-H deformation of inner hydroxyl groups
3448	O-H stretching of water	795	symmetric stretching of Si-O
1640	O-H deformation of water	749, 672	perpendicular Si-O stretching
1117	perpendicular Si-O stretching	553	deformation of Al-O-Si

II.3. TGA

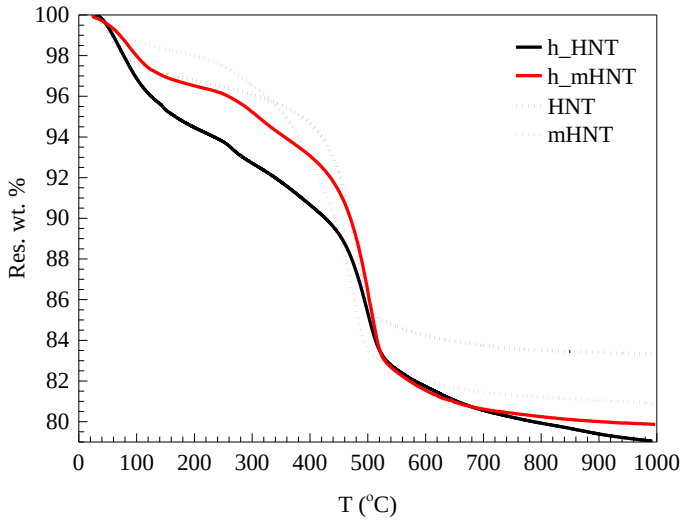

Figure S3.3 TGA curves of h_HNT, h_mHNT, HNT, and m_HNT tested under N_2. Inset: deferential thermal analysis graphs of h_HNT, h_mHNT, HNT, and m_HNT.

II.4. Morphological properties of HNTs

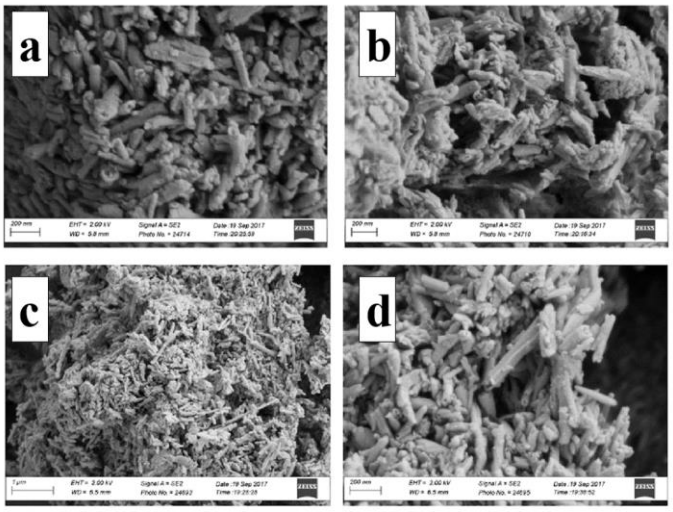

Figure S3.4 SEM micrographs of a)HNTs and b) mHNTs.

II.5. Flexural properties for epoxy/HNT and epoxy/mHNT

Table S3.2 Improvement (%) in average of flexural modulus ($\bar{E}$), average strain at maximum load ($\bar{\varepsilon}$), and average flexural strength ($\bar{\sigma}$) for H0, H1, H2, H5, and H10 vs. mH0, mH1, mH2, mH5, and mH10 specimens.

	HNT			**mHNT**		
wt.%	$\bar{\sigma}$ **(%)**	$\bar{\varepsilon}$ **(%)**	$\bar{E}$ **(%)**	$\bar{\sigma}$ **(%)**	$\bar{\varepsilon}$ **(%)**	$\bar{E}$ **(%)**
0	0.00	0.00	0.00	0.00	0.00	0.00
0.5%	-6.21	-8.96	19.32	-5.57	14.96	30.00
1%	1.12	0.72	17.20	-7.76	11.84	21.54
2%	-0.44	6.81	14.65	1.97	-6.18	19.23
5%	-32.20	6.81	25.69	1.31	11.43	16.15
10%	17.07	6.45	35.46	2.19	16.55	10.00

II.6. Sensitivity of epoxy/HNT nanocomposites to water

To find the amount of absorbed water by epoxy/HNT nanocomposites, three samples from each type of specimen are cut into the dimension of 20 mm x 10 mm x 3 mm, and then are immersed in distilled water at room temperature. Having been taken out of the water, specimens are dried properly, weighted, and then immersed back into water. The absorbed

amount of water is calculated using Equation S3.1 and results are reported as weight gain (wt.% gain) after 1 hour, 1 day, 1 week, and 3 weeks.

$$\text{wt. \% gain} = ((\text{wt.2} - \text{wt.1})/\text{wt.1})*100 \qquad \text{(S3.1)}$$

wt.1 and wt.2 is the weight of the dried sample before and after a specific time interval, respectively.

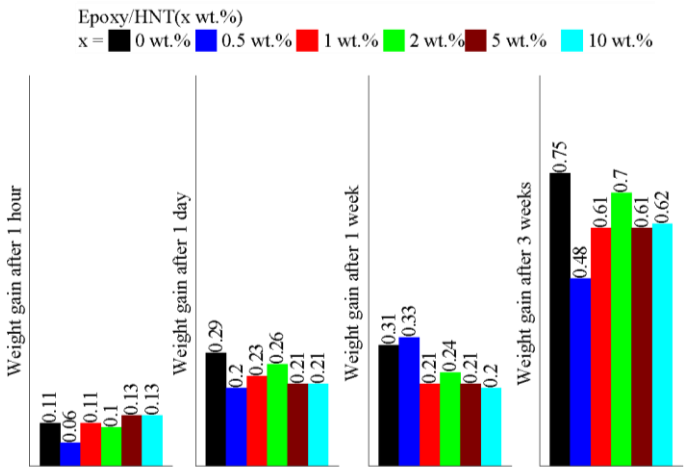

Figure S3.5 Bar graphs for the amount of water absorbed by H0, H1, H2, H3, H5, and H10 after 1 hour, 1 day, 1 week and 3 weeks.

Table S3.3 Weight gain (wt.%) by absorbing water after 1 week vs. after 3 weeks, and the decrease in the water uptake for epoxy/HNT nanocomposites.

HNT wt. %	0	0.5	1	2	5	10
wt. % after 7 days	0.31	0.33	0.21	0.24	0.21	0.2
Improv. % after 7 days	-	-7.65	33.31	23.7	33.24	36.28
wt. % after 21 days	0.75	0.48	0.61	0.7	0.61	0.62
Improv. %after 21 days	-	36.55	19.16	07.44	18.93	18.22

II.7. FTIR

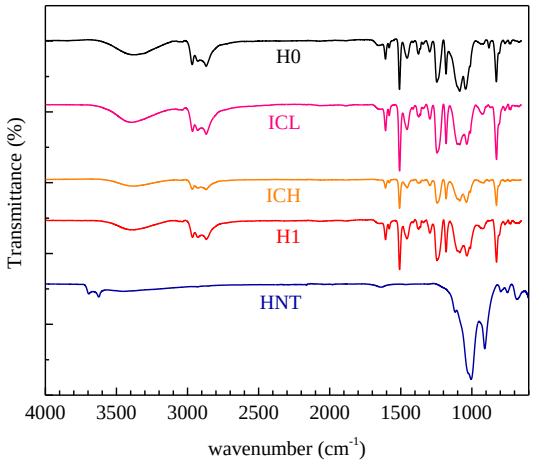

Figure S3.6 FTIR graphs for H0, H1, ICL, and ICH nanocomposites.

II.8. Rheological measurements

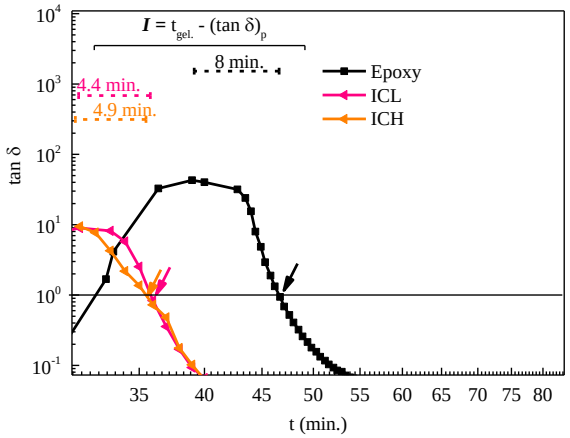

Figure S3.7 tan δ vs. t during complex viscosity measurements for H0, ICL, and ICH.

APPENDIX III

III.1. Schemes for both RTM molds

Each of RTM(II) plates are split in half through y-axis passing from the inlet Port.4 and outlet Port.5. The specimens in one half are aligned parallel to y-axis (90^{o}), and the second half of the specimens are aligned parallel to x-axis along the edge passing through the inlet Port.4 (Figure S5.1).

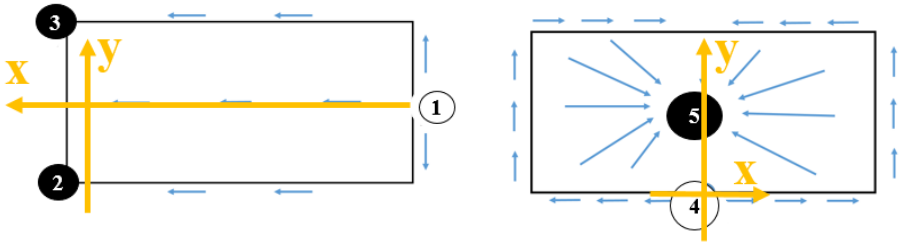

Figure S5.1 Scheme of RTM(I) and RTM(II) composite plates showing the assigned x, y axes.

III.2. Density and void content

Table S5.1 Density (ρ) value and population for N(I), NT(I), N(II) and NT(II) specimens.

	N(I)		**NT(I)**		**N(II)**		**NT(II)**	
	ρ	Population	ρ	Population	ρ	Population	ρ	Population
	1.41	7	1.47	9	1.40	5	1.43	14
	1.42	9	1.48	9	1.41	13	1.44	6
	1.43	2			1.42	5	1.45	6
					1.43	3	1.46	7
					1.44	8	1.47	5
					1.45	2		
					1.46	2		
Avg.	1.42		1.474		1.422		1.446	
STD	0.01		0.003		0.017		0.015	

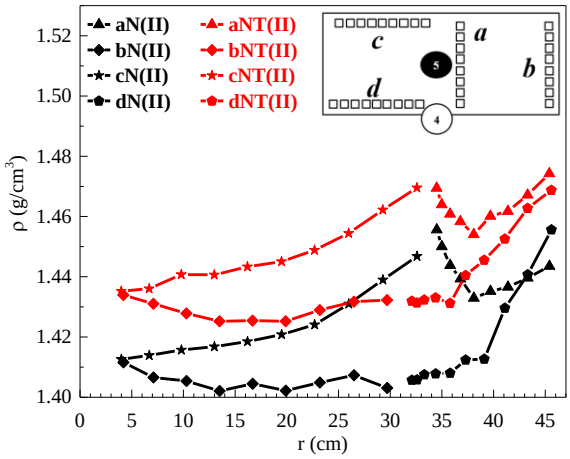

Figure S5.2 Density (ρ) of N(II) and NT(II) specimens as a function to thier specific locations on the composite plates.

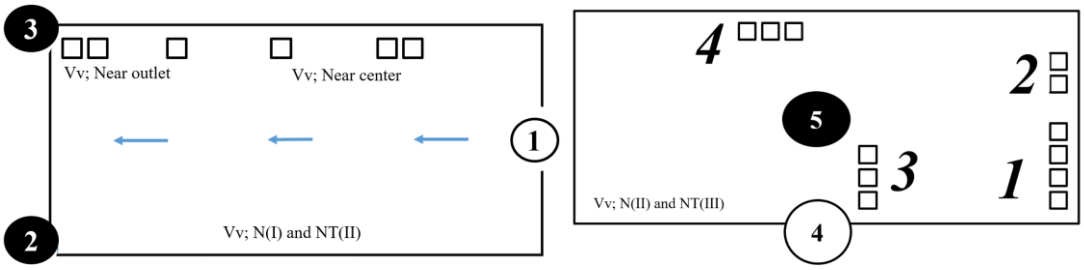

Figure S5.3 Schematic graphs shows locations of sample used to determine V_v for (a) N(I) and NT(I), and (b) N(II), NT(II) composites.

III.3. Flexural properties

In RTM(II) plates, NT(II) have 17% less V_v with lower homogeneity in the distribution of these voids across the plates compared to N(II). Figure S5.4 presents color maps for the flexural modulus and V_v for N(II), and NT(II) composite plates. As explained previously, NT(II) have less V_v across the whole composite plate compared to N(I) (i.e, V_v is higher by 1% in the region within the dashed red circle compared to the rest of the plate. Less V_v across the plate improves flexural strength and modulus of NT(II) compared to N(II) composites.

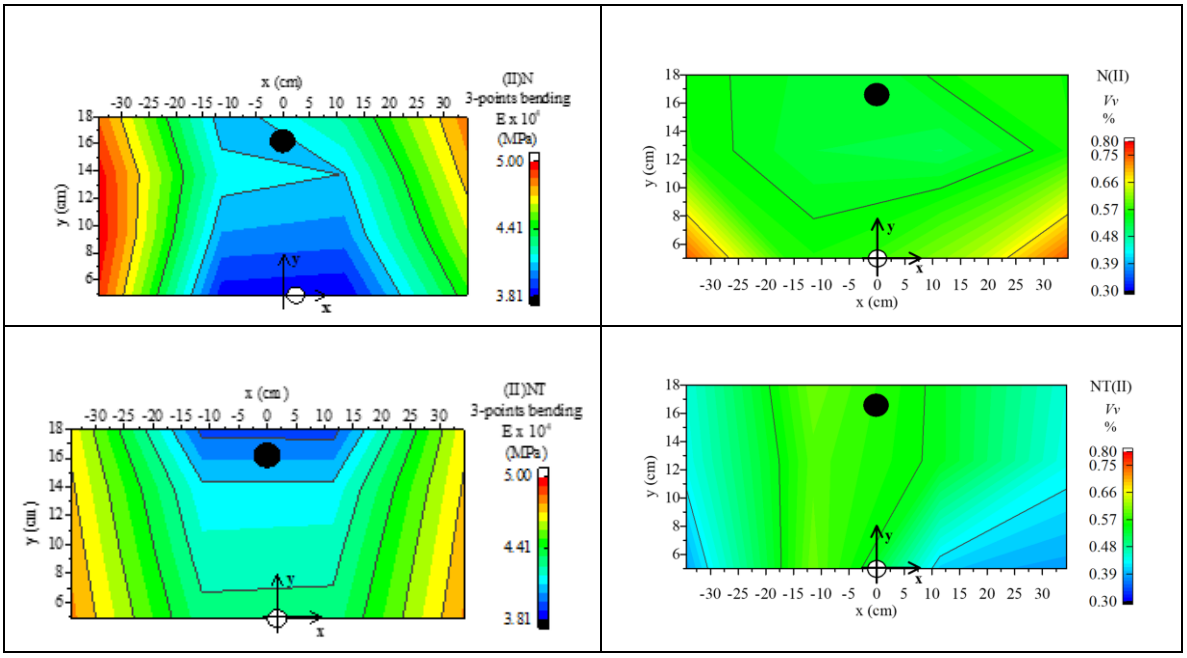

Figure S5.4 Color maps for flexural modulus and V_v for both N(II), and NT(II) composite plates.